

Optical collisions in crossed beams and Bose-Einstein condensation in a microtrap

Cristina Figl

▶ **To cite this version:**

Cristina Figl. Optical collisions in crossed beams and Bose-Einstein condensation in a microtrap. Atomic Physics [physics.atom-ph]. Université Paris Sud - Paris XI, 2004. English. NNT : . tel-00007125

HAL Id: tel-00007125
https://pastel.hal.science/tel-00007125

Submitted on 14 Oct 2004

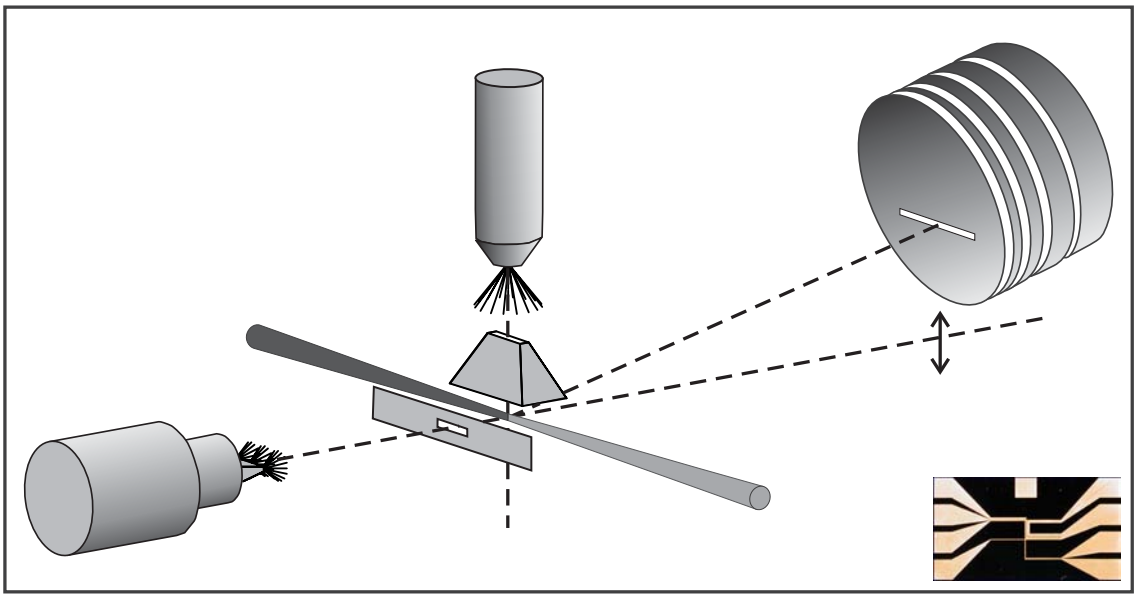
HAL is a multi-disciplinary open access archive for the deposit and dissemination of scientific research documents, whether they are published or not. The documents may come from teaching and research institutions in France or abroad, or from public or private research centers.

L'archive ouverte pluridisciplinaire **HAL**, est destinée au dépôt et à la diffusion de documents scientifiques de niveau recherche, publiés ou non, émanant des établissements d'enseignement et de recherche français ou étrangers, des laboratoires publics ou privés.

Optical collisions in crossed beams

and

Bose-Einstein condensation in a microtrap



Vom Fachbereich Physik der Universität Hannover
zur Erlangung des Grades

Doktorin der Naturwissenschaften
– Dr. rer. nat. –

genehmigte Dissertation von

Dipl. Phys. Cristina Figl

geboren am 02. Dezember 1974 in Hannover

2004

Referent: Prof. Dr. Joachim Großer
Korreferent: Prof. Dr. Christoph Westbrook
Tag der Promotion: 19. Mai 2004

This Ph.D work was done in the framework of the European Graduate College "Interference and Quantum Application" which is a collaboration of the University of Hannover in Germany, the University of Glasgow and the Strathclyde University in Scotland, and the Université Paris Sud IX in France. Within the college, a cotutelle agreement between the University of Hannover and the Université Paris Sud IX was established. While my work was focused on the study of differential optical collisions in the group of J. Grosser in Hannover, the College gave me the opportunity to join the group of A. Aspect for half a year and gain an insight into the fascinating world of Bose-Einstein condensation. Although the two subjects might seem to have not much in common, many experimental and theoretical techniques are similar which was both very interesting and instructive to explore.

Abstract

Optical collisions are studied in a crossed beams experiment. Differential cross sections of K-Ar collisions are measured and are used to derive the repulsive parts of the $X\Sigma$ and $B\Sigma$ potential curves. The achieved accuracy has not been realized with scattering experiments before. A collision energy resolved analysis of the final state probes the relative population of the fine-structure states $K(4p_{1/2})$ and $K(4p_{1/2})$ which depends on details of the outer part of the potentials. Calculations from the determined potentials are in concordance with the experimental results. The relative population of the Na fine-structure states after Na-N_2 and Na-O_2 collisions is determined similarly. The results for N_2 are in very good agreement with the theory. Differential cross sections of Ca-Ar optical collisions are measured for an asymptotically forbidden transition. The spectral dependence of the signal intensity shows a characteristic maximum. The experimental data are in good agreement with *ab initio* calculations.

Wires on a microchip create a magnetic trap that is used to obtain a ^{87}Rb Bose-Einstein condensate. The roughness of the magnetic potential is characterized by the measured density of a cold atom cloud. The measured roughness is compared to the roughness that is calculated from the geometry of the microwire.

Key words: optical collisions, molecular potentials, Bose-Einstein condensate

In einem Aufbau mit gekreuzten Teilchenstrahlen werden optische Stöße untersucht. Differentielle Wirkungsquerschnitte von K-Ar Stößen werden gemessen und benutzt, um die repulsiven Teile der $X\Sigma$ und $B\Sigma$ Potentiale mit einer Genauigkeit zu bestimmen wie sie in Streuexperimenten bislang nicht realisiert wurde. Die relative Besetzung der Feinstrukturniveaus $K(4p_{1/2})$ und $K(4p_{3/2})$ nach dem Stoß werden energieaufgeloest bestimmt. Sie hängt von den äußeren Teilen der Potentiale ab und stimmt sehr gut mit Berechnungen auf der Basis der bestimmten Potentiale überein. Ebenso wird die relative Besetzung der Na Feinstrukturniveaus nach Na-N_2 und Na-O_2 Stößen gemessen und für N_2 von den theoretische Ergebnisse sehr gut reproduziert. Differentielle Wirkungsquerschnitte des Stoßpaares Ca-Ar werden für einen asymptotisch verbotenen Übergang gemessen. Die spektrale Abhängigkeit der Signalintensität zeigt ein charakteristisches Maximum. Die experimentellen Ergebnisse stimmen gut mit *ab initio* Berechnungen überein.

Mit Strömen durch Drähte auf einem Mikrochip wird eine Magnetfalle realisiert, die benutzt wird, um ein ^{87}Rb Bose-Einstein Kondensat zu erzeugen. Die Rauigkeit des Magnetpotentials wird durch die Dichtemessung einer Atomwolke in der Falle charakterisiert. Die Größe der gemessenen Rauigkeit wird verglichen mit der Rauigkeit, die sich aus der Geometrie des Drahtes berechnet.

Schlagworte: optische Stöße, Molekülpotentiale, Bose-Einstein Kondensation

Nous avons étudié les collisions assistées par la lumière entre deux jets atomiques croisés. Les sections efficaces différentielles de collisions K-Ar sont mesurées et utilisées pour calculer les parties répulsives des potentiels $X\Sigma$ et $B\Sigma$. La précision sur les potentiels ainsi obtenus n'avait jamais été atteinte auparavant dans des expériences de diffusion. Une analyse de l'état final en fonction de l'énergie de collision nous permet de sonder la population relative entre les niveaux fins $K(4p_{1/2})$ et $K(4p_{1/2})$. Cette différence relative de population dépend en détail de la structure externe des potentiels. Les calculs à partir des potentiels déterminés sont en accord avec nos résultats expérimentaux. Nous avons également étudié la population relative entre les états fins d'atomes de sodium après des collisions Na-N_2 et Na-O_2. Les résultats pour N_2 sont en très bon accord avec la théorie. Nous avons mesuré les sections efficaces différentielles de collision pour des collisions Ca-Ar assistées par la lumière pour une transition asymptotiquement interdite. La dépendance spectrale de l'intensité du signal présente un maximum caractéristique. Les données expérimentales sont en bon accord avec des calculs *ab initio.*

Nous avons utilisé des fils microfabriqués pour créer un potentiel magnétique dans lequel nous avons obtenu un condensat de Bose-Einstein de ^{87}Rb. Nous avons caractérisé la rugosité du potentiel magnétique en mesurant le profil de densité d'un nuage d'atomes froids. Nous comparons la rugosité mesurée avec la rugosité calculée par la géométrie du fil.

Contents

List of Figures ix

List of Tables xiii

Introduction 1

Optical collisions in a crossed beams experiment 7

1 Theoretical description 7
- 1.1 Light absorption by a collision complex . . . 7
- 1.2 Semiclassical description . . . 10
- 1.3 Quantum mechanical treatment and nonadiabatic couplings . . . 15

2 Experimental method 19
- 2.1 Overview . . . 19
- 2.2 Laser system and optical components . . . 21
- 2.3 Detection scheme . . . 25
- 2.4 Projectile beam . . . 28
- 2.5 Target beam . . . 33
- 2.6 Vacuum system . . . 38
- 2.7 Background signals and corrections . . . 38
- 2.8 Data acquisition, automatization and electronics . . . 45
- 2.9 Convolution of theoretical data . . . 46

3 Results and discussion 51
- 3.1 KAr . . . 51
  - 3.1.1 Differential cross sections . . . 51
  - 3.1.2 Determination of $X\Sigma$ and $B\Sigma$ potentials . . . 55
  - 3.1.3 Nonadiabatic transitions . . . 61
- 3.2 NaN_2, NaO_2: Nonadiabatic transitions . . . 63
- 3.3 CaAr: Optical collisions near a forbidden atomic transition . . . 64

Bose-Einstein condensation in a microtrap 73

4 Theoretical description **73**
4.1 BEC phase-transition . . . 73
4.2 Collisions at low energies . . . 74
4.3 Wavefunction and density distribution . . . 74
4.4 Magnetic trapping . . . 75
4.5 Laser cooling . . . 76
4.6 Magneto-optical trap . . . 77
4.7 Evaporative cooling . . . 78

5 Experimental realization **81**
5.1 Overview of the set-up . . . 81
5.2 Production of the microchip . . . 82
5.3 Magnetic fields of the microwires . . . 84
5.4 Laser system . . . 88
5.5 Imaging system . . . 88

6 Results and discussion **91**
6.1 The way to a ^{87}Rb BEC on a microchip . . . 91
6.2 Roughness of the magnetic potential . . . 96
6.3 Prospects . . . 104

Summary **107**

Appendix **111**

A Derivation of the phase difference of two trajectories **111**

B Conversion from optical collision laboratory to center of mass coordinates **115**

C Reference atomic transitions and conversion to SI units **119**

D KAr differential cross sections and determined potentials **121**

E Physical properties of ^{87}Rb **127**

Bibliography **129**

List of Figures

1.1 Potential curves of two atoms . . . 7
1.2 Potential curves including energy of photon . . . 8
1.3 Modification of potentials by light . . . 9
1.4 Potential curves for an optical collision . . . 11
1.5 Coordinates for description of collision . . . 11
1.6 Classical trajectory . . . 12
1.7 Deflection function . . . 13
1.8 Phase and phase difference. . . . 14
1.9 Crossing deflection functions . . . 14
1.10 Region of nonadiabtic transitions . . . 16

2.1 Experimental Set-up . . . 19
2.2 Optical components . . . 21
2.3 Set-up for filtering of excitation laser . . . 23
2.4 Spectrum of $A^* \rightarrow A(nl)$ transitions . . . 24
2.5 Spectrum of $A \rightarrow A(nl)$ transitions . . . 24
2.6 Rydberg detector . . . 26
2.7 Time of flight determination . . . 27
2.8 Projectile beam sources . . . 29
2.9 Profile of projectile beam . . . 30
2.10 Angular distribution of projectile beam . . . 31
2.11 Velocity distribution of projectile atoms . . . 32
2.12 Argon beam source . . . 34
2.13 Angular distribution and density distribution over scattering volume of argon beam. . . . 34
2.14 Measurement of argon velocity . . . 35
2.15 Angular distribution and density distribution over scattering volume of molecular target beam. . . . 37
2.16 Molecular target beam source . . . 37
2.17 Measurement of molecular target velocity . . . 38
2.18 Ca: Signal dependency on intensity of excitation laser. . . . 41
2.19 Projectile beam profile with and without target gas . . . 42
2.20 K: Signal dependency on intensity of excitation laser. . . . 43
2.21 K: Signal dependency on intensity of detection laser: Low intensities . . . 44
2.22 K: Signal dependency on intensity of detection laser: High intensities . . . 44

2.23 Communication of computer with experimental hardware 46
2.24 Differential scattering rate 47
2.25 KAr: Resolution of scattering angle and collision energy 49

3.1 KAr: Differential cross sections and deflection functions for different detunings 52
3.2 KAr: Differential cross sections and deflection function for different collision energies 53
3.3 KAr: Potentials 54
3.4 KAr: Detuning as a function of the Condon radius 54
3.5 KAr: potentials 56
3.6 KAr: Initial potential system 57
3.7 KAr: Calculation with initial potential 58
3.8 KAr: best potentials 59
3.9 KAr: Calculation with new potential 60
3.10 KAr: Detuning as a function of the Condon radius 60
3.11 Principle of the measurement of nonadiabatic transitions. 61
3.12 KAr: Nonadiabatic transitions 62
3.13 KAr: Resolution of relative kinetic energy 62
3.14 NaN_2, NaO_2: Nonadiabatic transitions 64
3.15 CaAr: Potentials 65
3.16 CaAr: Transition dipole moments and Condon radius 66
3.17 CaAr: Differential cross sections. 66
3.18 CaAr: Detuning dependence 67

4.1 Principle of MOT 78
4.2 Principle of forced evaporative cooling 79

5.1 Design of the experiment 81
5.2 Layout of wires on microchip 83
5.3 Production of wires 83
5.4 Height profile of chip surface. 84
5.5 Magnetic field of wire with bias field 85
5.6 Magnetic field of u-wire 86
5.7 Magnetic field of z-wire 86
5.8 Optical transitions of ^{87}Rb 87
5.9 Imaging system I 89
5.10 Imaging system II 90

6.1 Image of cloud in u-MOT 92
6.2 Image of cloud in magnetic trap. 93
6.3 Realization of evaporative cooling 94
6.4 Image of BEC: density distribution 95
6.5 Image of BEC: time evolution 95
6.6 Images of fragmented cloud 96
6.7 Shifting of cloud along central wire 97

6.8 Fit of harmonic potential 98
6.9 Fragmentation potential 99
6.10 Power spectral density of fragmentation potential 100
6.11 Pictures of central z-wire 101
6.12 Roughness of wire edge 101
6.13 Power spectral density of magnetic potential calculated from border of wire 103
6.14 Comparison of power spectral densities 103

A.1 Phase of a trajectory 112

B.1 Newtondiagram 115
B.2 Calculation of Jakobi determinante. 117

D.1 KAr-Differential cross sections: 220 cm^{-1} 122
D.2 KAr-Differential cross sections: 480 cm^{-1} 123
D.3 KAr-Differential cross sections: 640 cm^{-1} 124
D.4 KAr-Differential cross sections: 720 cm^{-1} 125

List of Tables

2.1 General quantities of experimental set-up 20
2.2 Laser dyes 22
2.3 Uncertainty in frequency of lasers 25
2.4 Ion time-of-flights in detector 27
2.5 Relevant quantities of projectile beam sources 29
2.6 Vapor pressure and fraction of dimers 30
2.7 Automized parameters 45

5.1 Parameters of z-trap 87

C.1 Reference atomic transitions 119
C.2 Conversion into SI units 119

D.1 KAr potentials 126

Introduction

Since the first experimental evidence of atoms in the beginning of the 19th century, the study of their nature and interaction is one of the major goals in physical and chemical research. The characterization of the interactions of these microscopic particles demands elaborate experimental and theoretical techniques. A widespread method for the experimental study of atomic and molecular interactions is the analysis of collision experiments. Collisions between atoms or molecules determine the characteristics of various systems such as combustions, laser media, the outer atmosphere of stars, and the atmosphere of the earth. Collision processes also constitute an essential mechanism involved in chemical reactions in the gaseous phase and in the process of forming of a Bose Einstein condensate. Studies of collisions reveal the underlying physical mechanisms by characterizing the most basic system of two (or just a few) particles.

The theoretical description of atom-atom and atom-molecule collisions (as opposed to for example electron-atom collisions) can in very good approximation be broken down into two steps. The first step is the determination of interatomic potentials describing the energy of the system in a certain eigenstate as a function of the static interatomic distance (Born-Oppenheimer approximation). On the basis of the potentials, the collision dynamics are described in a second step in which also couplings between different states can be taken into account. The treatment of cold, thermal or hot collisions with collision energies from less than a meV to MeV is hereby different only in details, not in the overall principle. The quality of *ab initio* calculations of collision processes, especially for alkali+rare-gas systems, has improved considerably with increasing computing power. However, experimental data are still more accurate than calculations, so the possibility of comparing calculated to experimental results is essential for testing the various theoretical approaches. In cases for which a calculation exceeds the computation power, an experiment is left as the only alternative.

A widespread experimental approach to a study of collisions is a complete characterization of the quantum states of the particles before and after the collision. This is possible in a standard crossed beams experiment in which, however, the collision itself is not observed. A direct access is possible with an optical excitation of the collision pair, a process known as an optical collision [Bur85]. The photon serves as a tool to gain a direct insight into the collision and can be used to coherently control the outcome of the collision.

An optical collision

$$A + B + h\nu \rightarrow (AB)^* \rightarrow A^* + B \tag{0.1}$$

is a collision between a projectile A and a target B. The collisional complex (AB) is excited during the collision by a photon with the energy $h\nu$ which is detuned by $\Delta h\nu$ from the atomic transition A→A*. The optical transition occurs in good approximation at a fixed distance r_c of the atoms where the resonance condition

$$V_e(r_c) - V_g(r_c) = h\nu. \tag{0.2}$$

is fulfilled [All82]. r_c is called Condon radius. $V_g(r)$ is the potential corresponding to the initial state of the collision system as a function of the interatomic distance r and V_e is the potential that is coupled to V_g by the light field.

Optical collisions are usually studied in gas cells [Hav86, Gon94, Beh96, Lin01]. In this type of experiment, the signal is averaged over the scattering angle and over a thermal distribution of collision energies. The observation of optical collisions in a crossed beams experiment has considerably expanded the experimental possibilities, as presented first in [Gro94]. In the so-called differential optical collisions, a scattering angle of the excited particles A* is selected and their velocities are determined. The technique allows a very detailed characterization of the collision event. Differential optical collisions have been used successfully to study Na–rare gas and Na–molecule systems [Gro96, Gro97b, Gro99a] leading to new insights into the collision processes. In the present work, the following differential optical collisions are studied:

$$\begin{aligned}
K(4s)^2S + Ar + h\nu &\rightarrow (KAr)^2\Sigma &&\rightarrow K(4p)^2P_{1/2,3/2} + Ar \\
Ca(4s^2)^1S + Ar + h\nu &\rightarrow (CaAr)^1\Sigma &&\rightarrow Ca(4s3d)^1D + Ar \\
Na(3s)^2S + M + h\nu &\rightarrow (NaM)^2A' &&\rightarrow Na(3p)^2P_{1/2,3/2} + M, \quad M=N_2,O_2
\end{aligned} \tag{0.3}$$

The range of systems is thus expanded to K–Ar, another alkali+rare-gas system, and Ca–Ar, an alkaline-earth+rare-gas collision pair.

The differential cross sections of optical collisions show pronounced Stueckelberg oscillations resulting from a coherent superposition of pathways that lead to the same scattering angle. The interference pattern can be used to test and determine interatomic potentials [Gro97a, Gro00]. Potentials can be determined with customary spectroscopic techniques with an accuracy of less than cm^{-1}. However, the measurements are restricted to regions where bound states exist [Lee91, Bru91, Bok96, Kau97b, Zim99]. Repulsive parts of potentials can be studied with optical collisions in gas cell experiments reaching accuracies around 50 cm^{-1} [Hed72, Beh96]. The accuracy of potentials derived from differential cross sections of optical collisions, however, is more precise. A combination of results from *ab initio* calculations, spectroscopic measurements and differential cross

sections of optical collisions is a novel approach to determine a set of potentials that is reliable over a greater range of interatomic distances for which the potentials are repulsive as well as attractive. In this work, the technique is applied to the K-Ar system.

Coupling between different states can lead to nonadiabatic transitions during a collision resulting in a variety of final states. Transitions in the ingoing part of a collision may even decide over the outcome of a chemical reaction cite68. With the method of differential optical collisions, transition probabilities in the outgoing cannel of a collision can be probed as a function of the collision energy which is more detailed than measurements in gas cells [Gro99b]. Measured relative population ratios of the fine-structure levels of K and Na after an optical collision will be presented.

The atomic transition that is used for the Ca–Ar system is forbidden in the free calcium atom. It becomes an allowed molecular transition in the presence of an argon atom as a perturber. Thus, the strength of the transition varies considerably with the Ca-Ar distance. It is given by the absolute value of the transition dipole moment. Referring to Equation 0.2, the energy $h\nu$ of the excitation photon determines the distance of the collision partners at the moment of excitation. The energy is hereby usually given by its detuning from a reference atomic transition (given in Table C). A variation of the detuning thus probes the absolute value of the transition dipole moment as a function of the interatomic distance. Comparable transitions were studied as well in alkali+rare-gas systems [Kle88, Ued89].

The optical transition probability depends not only on the absolute value of the transition dipole moment but also on its orientation with respect to the light polarization. The transition dipole moment reflects the geometric properties of the ground and excited state wavefunction at the moment of excitation and is oriented with respect to the axis of the collision partners. Notably, in a differential optical collision experiment the direction of the axis at the moment of excitations is fixed in space. In the case of atom – atom collisions, the transition dipole moment is orientated either parallel or perpendicular to the atom – atom axis and a polarization experiment allows the determination of the relative position vectors of the collision partners during the collision and is comparable to a photography of the collsion. For atom – molecule collisions, the orientation of the transition dipole moments is more complicated, and polarization experiments probe the distribution of orientations of the dipole transition moments with respect to the atom-molecule axis [Gol01, Fig02]. The polarization of the photon can not only be used to study the collision event, it is also a tool to coherently control the collision. Using different elliptical polarizations, the interference pattern of the differential cross sections can be arbitrarily tuned by imprinting the phase of the light onto the collision complex [Sch04]. This way, basically a tunable interferometer is established.

A Bose-Einstein condensate (BEC) is a different domain of atomic interaction. It is the massive population of the ground state in an external trapping potential that occurs when the phase-space density exceeds a critical value. The crucial decrease to temperatures of nK to μK is realized by evaporative cooling which relies on the rethermalization of the atoms by elastic collisions. Elastic collisions at low temperatures are governed only by

one parameter, the s-wave scattering length, and the differential cross sections do not depend on the scattering angle, as opposed to the thermal collisions that are studied in the first part of this work. In a BEC, the atoms can be collectively described by a macroscopic wavefunction resulting in interference phenomena that are commonly known in lasers or superconductors. BEC, although predicted already in 1925, has become experimentally accessible only some years ago in 1995 [And95, Dav95, Brad95]. For the achievement and study of a BEC, the atoms are often held in a magnetic trap which is usually created by macroscopic coils outside the vacuum chamber. An alternative is the use of wires on a microchip that is mounted close to the atoms [For98, Rei99, Den99, Key00, Fol00, Rei01]. The shape of the trapping potential can be changed conveniently and accurately by the current in the wires and atom-optical devices like wave guides and beam splitters can be realized [Cass00, Den99, Rei01]. BEC on a microchip was achieved by several groups in the last years [Hän01, Ott01, Sch03]. The most important technical advantage of a set-up with a microchip is that more confining traps can be realized. Thus, a higher density of the trapped cloud is achieved resulting in a larger elastic collision rate which sets the timescale for the evaporative cooling process and a BEC is achieved about 10 times faster than in an experiment with macroscopic coils. Hence, the lifetime of the atoms in the magnetic trap can be accordingly shorter which results in weaker demands on the background pressure and thus in a significant technical simplification of the experiment. A further advantage is the low inductivity of the micro wires allowing to turn off the magnetic trap very quickly. The experimental realization with a microchip is hence smaller and more convenient.

One of the main expamples of macroscopic quantum effects is Josephson tunneling which occurs in two superconductors separated by a finite barrier [Jos62, Mei02]. It was pointed out even before BEC was accomplished experimentally that Josephson tunneling could be observed in a BEC [Jav86]. For such an experiment, two traps are required that are separated on a scale of μm by a tunable tunneling barrier. It seems realistic that such traps could be realized with wires on a microchip. Furthermore, with the high confinement of microtraps, mono-mode atomic waveguides could be established to form a guided interferometer. However, in various experiments a fragmentation of the atomic density was reported when the atoms are brought close to the wires [Lea02, Kra02, For02, Lea03] limiting the possibility of a coherent manipulation of a BEC. The reason for the fragmentation is the roughness of the magnetic field from the wire which presents the current limitation for a coherent manipulation of a BEC. The cause and the order of magnitude of the roughness is studied in the present work. A cloud of cold atoms is used to probe the spatial variation of the magnetic field produced by a wire on a microchip and the results are compared to calculations that rely on an analysis of the geometry of the wire.

Optical collisions in a crossed beams experiment

Chapter 1

Theoretical description

1.1 Light absorption by a collision complex

The interaction of a collisional system with a light field results in a modification of the potential curves. Secondly, the optical excitation is not located precisely at a fixed distance of the collision partners. It takes rather place in a region around it. In the rest of this work, the limiting case of small light intensities is assumed for which the two effects are neglected. To justify the approximation, the magnitude of the effects will be calculated. Furthermore, the optical transition probability will be derived. For the calculations, the dressed states model is used and the molecular system is simplified by a two state model [Ban94, Coh92]. In the presented experiments, the duration of the laser pulse (several ns) is long compared to the duration of the collision (several ps). Therefore, the Hamilton operator for the light field is assumed to be time independent.

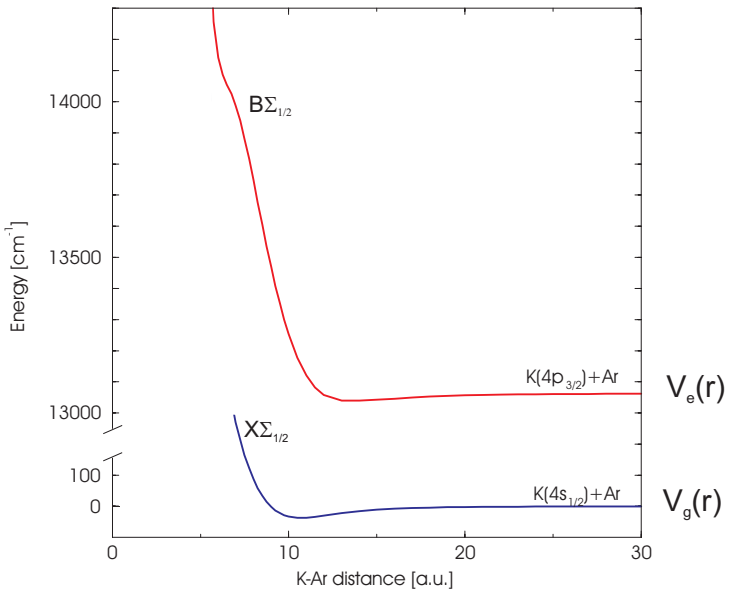


Figure 1.1: Potential curves for the KAr system [Czu02] as an example for a system of two atoms. Shown is the ground state $X\Sigma_{1/2}$ and the excited state $B\Sigma_{1/2}$ which is accessible with a positive detuning of the laser.

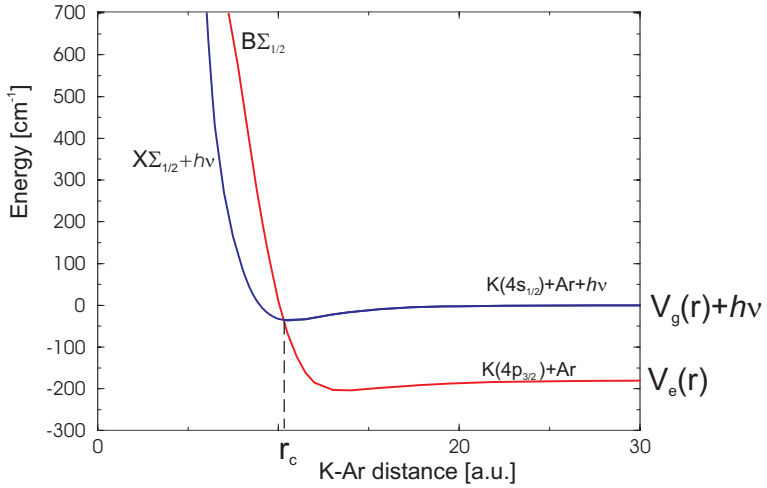


Figure 1.2: Potential energy curves of the KAr system including the energy of the photon. The asymptote of the ground-state potential is shifted to zero. The intersection of the two curves is denoted as the Condon radius r_c.

The optical transition occurs from a ground-state potential $V_g(r)$ to an excited-state potential $V_e(r)$. $V_g(r)$ and $V_e(r)$ are the eigenenergies of the Hamilton operator $H_{\text{atoms}}(r)$ (Figure 1.1). $H_{\text{atoms}}(r)$ includes the interactions of the two particles as a function of the interatomic distance r. H_{light} is the Hamilton operator corresponding to the energy of the photons. The eigenstates of $H_{\text{atoms}} + H_{\text{light}}$ can be described by coupled product states of the eigenstates $|\text{g}\rangle$ and $|\text{e}\rangle$ of H_{atoms} and the Bloch states of the photons: $|1\rangle = |\text{g}\rangle|\text{n}+1\rangle$ is the ground state of the molecular system in the presence of n+1 photons, and $|2\rangle = |\text{e}\rangle|\text{n}\rangle$ the excited state with n photons. In the experiment, the system is prepared in the initial state $|1\rangle$ and detected in the final state $|2\rangle$. The corresponding eigenenergies are

$$H_{11} = V_g(r) + h\nu \text{ and } H_{22} = V_e(r), \tag{1.1}$$

as illustrated in Figure 1.2. Note that at the Condon radius r_c, where $V_e(r_c) - V_g(r_c) = h\nu$, $H_{11} = H_{22}$. The interaction between the atoms and the light is described by H_{int}, so the Hamilton operator H that will be considered in the following is

$$H = H_{\text{atoms}} + H_{\text{light}} + H_{\text{int}}. \tag{1.2}$$

When written in the basis of $|1\rangle$ and $|2\rangle$, H_{int} introduces non-diagonal entries H_{12} into H. $H_{12} = \frac{\hbar\omega_R}{2}$ where $\omega_R = \frac{\mathbf{Ed}}{\hbar}$ is the Rabi frequency given by the electric dipole interaction for an electric field of magnitude $\mathbf{E}$ and the transition dipole moment $\mathbf{d} = \langle 2|e\mathbf{r}|1\rangle$. With typically used laser pulse energies of 0.1 mJ, a pulse duration of 12 ns and a transition dipole moment of 1 a.u., the value of the Rabi frequency is at maximum $2.3 \cdot 10^{11}\text{s}^{-1}$ and

$$H_{12} \leq 6.0 \cdot 10^{-1}\,\text{cm}^{-1}. \tag{1.3}$$

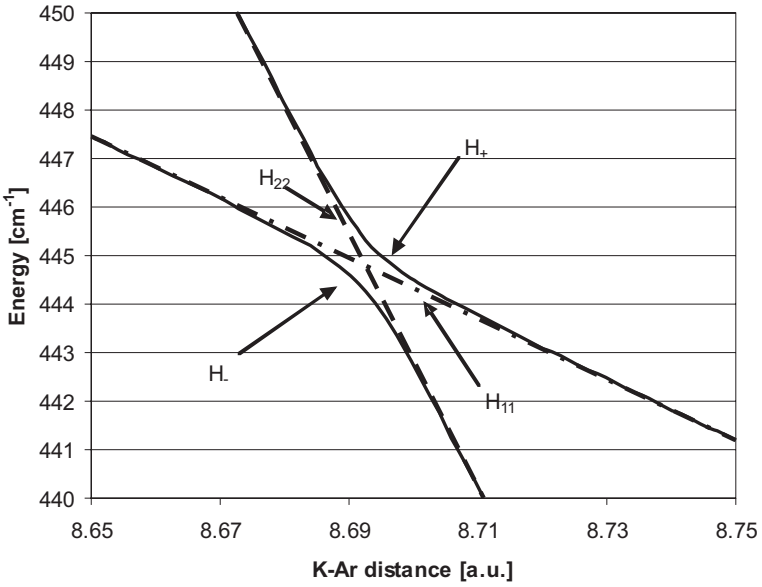


Figure 1.3: Modification of interatomic potentials by light shown for the KAr $X\Sigma_{1/2}$ and $B\Sigma_{1/2}$ state. Detuning is $480\,\mathrm{cm}^{-1}$. Dashed lines: Potentials without atom-light interaction, solid lines: interaction included.

The eigenenergies $H_{+,-}$ of H are calculated by diagonalizing H:

$$H_{+,-} = \frac{H_{11}+H_{22}}{2} \pm \sqrt{\left(\frac{H_{11}-H_{22}}{2}\right)^2 + H_{12}^2}. \tag{1.4}$$

$H_{11,22}$ and $H_{+,-}$ are shown examplarily for the KAr system in Figure 1.3 for a detuning of $480\,\mathrm{cm}^{-1}$. In the limit of small light intensities, $H_{12} \to 0$ and the eigenvalues of H pass into the eigenvalues H_{11} and H_{22} of $\mathrm{H_{atoms}} + \mathrm{H_{light}}$. For nonzero H_{12}, the crossing of the potential curves at r_c becomes an avoided crossing. The modification due to the light field depends on r and is at maximum directly at the Condon radius with a magnitude of H_{12}. This is small compared to typical accuracies of calculated potentials of 10-50 cm^{-1}. Furthermore, the modification is significant only in a region around the Condon radius where $H_{12} \geq |H_{11} - H_{22}|$. The region's dimension is less than 0.01 a.u. It is thus justified to neglect the change of the potential curves due to the interaction of the atoms with the light field.

Now we turn to the estimation of the region of transition from $|1\rangle$ to $|2\rangle$. For this reason, the eigenfunctions $|+\rangle$ and $|-\rangle$ of H are calculated. In the basis of $|1\rangle$ and $|2\rangle$ they can be expressed by:

$$|+\rangle = \cos\alpha|1\rangle + \sin\alpha|2\rangle \qquad |-\rangle = \sin\alpha|1\rangle - \cos\alpha|2\rangle \tag{1.5}$$

with the mixing angle α given by

$$\cot(2\alpha) = \frac{H_{11}-H_{22}}{2H_{12}}. \tag{1.6}$$

α can vary from zero to $\pi/2$. In a certain region around the Condon radius, α changes from values close to zero to values close to $\pi/2$. Accordingly, the composition of $|+\rangle$ goes from almost only $|1\rangle$ to almost only $|2\rangle$. The change takes mainly place where $H_{12} \geq |H_{11} - H_{22}|$. This is the same region in which the modifications of the potentials are significant. For the present experimental conditions, the optical excitation takes place at distances of 0.01 a.u. around the Condon radius. The assumption of a well localized transition is thus legitimate.

For calculating the optical transition probability, a collision process has to be considered. We start in the state $|1\rangle$ for large distances r. When the atoms approach, r is decreased. An adiabatic (slow) following of the system would lead to the state $|2\rangle$ after having passed the avoided crossing at r_c. On the contrary, a sudden, diabatic behavior would conserve the initial state $|1\rangle$. The probability p_d for a diabatic passage can be calculated using the Landau-Zener model [Nik84]:

$$p_d = e^{-\pi\gamma} \tag{1.7}$$

with the Massey parameter $\gamma = \frac{2H_{12}^2}{\hbar|\Delta H'|v(r_c)}$ where $\Delta H' = \partial_r(H_{11}(r_c) - H_{22}(r_c))$ is the difference in slope of the two potentials and $v(r_c)$ is the radial velocity, both taken at the Condon radius. Correspondingly, the probability for an adiabatic passage is $p_a = 1 - p_d$. In a full collision, the system passes the Condon radius twice and the probability p_{oc} for the initial state $|1\rangle$ to transform into the final state $|2\rangle$ is

$$p_{oc} = p_d(1 - p_d) \tag{1.8}$$

Under the experimental conditions, p_d is close to one and transition probabilities for KAr are in the order of a hundredth percent. In this case, p_{oc} can be expanded in γ:

$$\lim_{\gamma\to 0} p_{oc} = \pi\gamma = \frac{\pi(\mathbf{Ed})^2}{2\hbar|\Delta H'|v(r_c)} \tag{1.9}$$

Note that p_{oc} depends on the relative orientation of the polarization with respect to the transition dipole moment.

1.2 Semiclassical description

A discussion of the semiclassical method opens an intuitive understanding of the collision process The deviations between the classical and quantum mechanical treatment are small enough to use a semiclassical treatment for qualitative discussions [Hof99]. For quantitative comparisons, the quantum mechanical approach is used which is outlined in section 1.3. In this section, the concept of trajectories and deflection functions will be

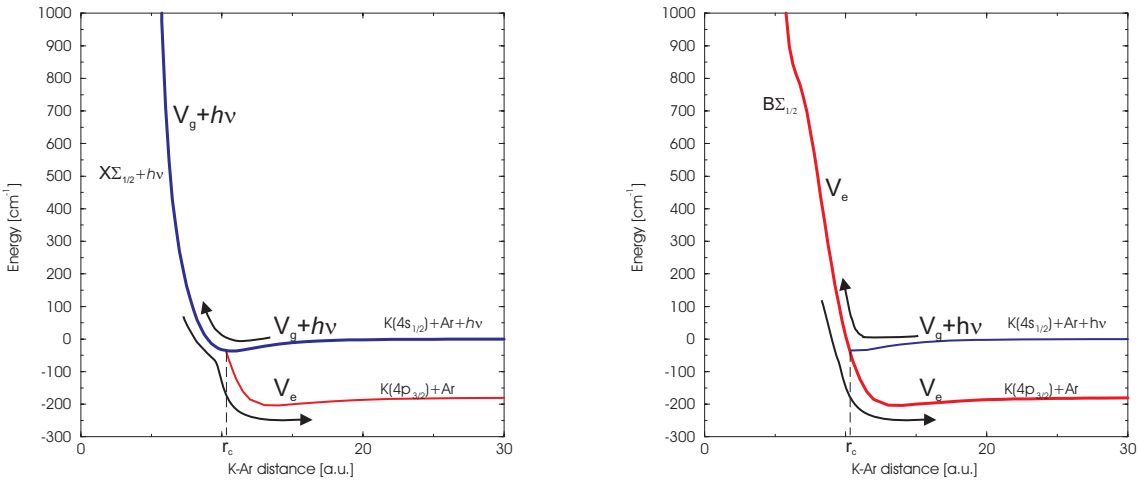


Figure 1.4: Potential curves for the KAr system including the energy of the excitation photon. The asymptote of the incoming state is shifted to zero. Left figure corresponds to the excitation taking place in the outgoing part of the collision, right figure in the incoming part.

introduced for the case of atom–atom collisions. The deflection functions will be used to derive an expression for the phase of the trajectory and for the differential cross section.

The starting point for a semiclassical calculation are again the two potential energy curves $V_g + h\nu$ and V_e. From these, $V(r)$ is constructed which changes at the Condon radius from $V_g + h\nu$ to V_e. To provide uniqueness, $V(r)$ is split into $V_1(r)$ and $V_2(r)$ for the incoming part of the collision ($\dot{r} < 0$) and the outgoing part ($\dot{r} > 0$), respectively. There are two possible combinations of $V_g + h\nu$ and V_e since the excitation can take place when the Condon radius is passed in the incoming part of the collision or in the outgoing part, as can be seen in Figure 1.4. Each of the two constructed $V(r)$ is used to set up equations of motion and calculate trajectories $\mathbf{r}(t)$ where $\mathbf{r}(t)$ is the relative position vector of the nuclei. From the conservation of the orientation of the angular momentum follows that the trajectories are confined to the plane that is set by the initial positions and the initial relative velocity of the atoms $\mathbf{v}$. Suitable coordinates to describe the motion of the system are thus the polar coordinates $r(t)$ and $\phi(t)$ as illustrated in Figure 1.5. The equations of motion are derived from the conservation of angular momentum and from the conservation of

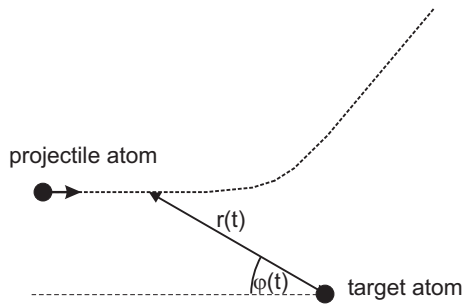


Figure 1.5: Illustration for the coordinates r and ϕ that are used to describe a collision.

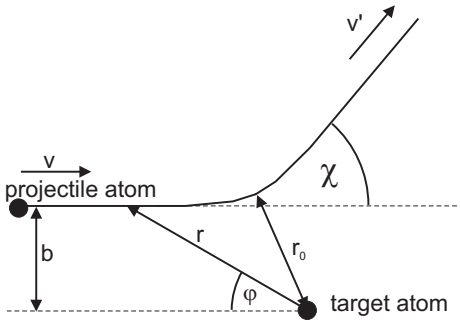


Figure 1.6: A classical trajectory. b is the impact parameter, χ the deflection angle, v and v' the velocities before and after the collision, respectively, and r_0 the classical turning point.

energy E [Chi74]:

$$\dot{r}(t) = \pm v\sqrt{1-\frac{V(r)}{E}-\frac{b^2}{r^2(t)}} \tag{1.10}$$

$$\dot{\varphi}(t) = \frac{vb}{r^2(t)}. \tag{1.11}$$

Initial conditions are the initial relative velocity $v=\sqrt{\frac{2E}{m}}$, m being the reduced mass of the system, and the impact parameter b. The negative sign in Equation 1.10 corresponds to the incoming part of the collision, the positive to the outgoing part. The distance r_0 for which $\dot{r}=0$ is the classical turning point. From Equation 1.11 and Equation 1.10, the trajectory can be calculated numerically.

The deflection angle χ (see Figure 1.6) is found by integrating φ over r from and to a distance R large enough to neglect the atomic interactions, resulting in

$$\chi(v,b) = \pi - \int_{r_0}^{R} \frac{b}{r^2}\left(\frac{1}{\sqrt{1-\frac{V_1(r)}{E}-\frac{b^2}{r^2}}}+\frac{1}{\sqrt{1-\frac{V_2(r)}{E}-\frac{b^2}{r^2}}}\right)dr. \tag{1.12}$$

$\chi(v,b)$ is the deflection function which assigns every impact parameter b the corresponding deflection angle for a fixed collision energy E as given by v. It can be calculated numerically in a straightforward way. A typical deflection function for an optical collision with the excitation taking place in the outgoing part of the collision is shown in Figure 1.7. There is a largest possible impact parameter. Trajectories with larger impact parameters do not reach the Condon radius anymore. The minimum in the deflection function at the impact parameter b_r is denoted as the rainbow scattering angle θ_r. The experimentally accessible scattering angle θ is related to the deflection angle by $\theta = |(\chi+\pi)mod(2\pi)-\pi|$ since a negative and a positive deflection angle of the same absolute value can experimentally not be distinguished. The same is true for deflection angles modulo 2π.

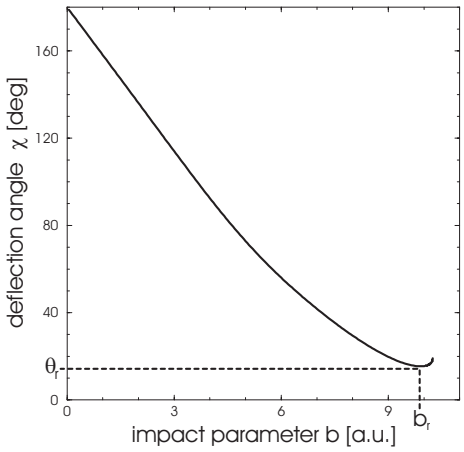


Figure 1.7: Deflection function. b_r is the impact parameter for which the scattering angle has a minimum θ_r.

To account for interference effects, each trajectory is assigned a phase $\phi(r)$ which can be calculated by the stationary phase method [Chi91]. A more intuitive way, however, is an integration of the wavenumber $k(\mathbf{r}) = \frac{m|\dot{\mathbf{r}}|}{\hbar}$ over the pathway of the trajectory:

$$\phi(r) = \int_R^r k(\mathbf{r}) ds \tag{1.13}$$

In comparison to the stationary phase method, Equation 1.13 gives the same result apart from several constant contributions of $\frac{\pi}{4}$ which are, however, not of interest for the following discussion. On this basis, the phase $\phi(v,b)$ of the trajectory after the collision can be calculated. Some transformations which are given in detail in Appendix A result in a rather simple expression:

$$\phi(v,b) = -k \int_b^{b_r} \chi(b') db' - kb\chi + C'. \tag{1.14}$$

The integral is the area under the deflection function as illustrated in Figure 1.8. In the case of an optical collision, there are two potentials that can be constructed leading to two deflection functions (see Figure 1.8). They merge at the largest possible impact parameter. For all other impact parameters, the two deflection functions result in more than one trajectory that contribute to one scattering angle. We will discuss the case of positive deflections angles with the contribution of two trajectories which is relevant for the discussion of the experimental results. When interference of these indistinguishable pathways shall be taken into account, their relative phase $\Delta\phi$ has to be determined. The trajectories have different impact parameters $b_1(\theta)$ and $b_2(\theta)$ and can belong to different deflection functions χ_1 and χ_2. The phase difference $\Delta\phi(\theta)$ is:

$$\Delta\phi(\theta) = k \int_\theta^{\theta_r} \left(b_1(\theta') - b_2(\theta')\right) d\theta'. \tag{1.15}$$

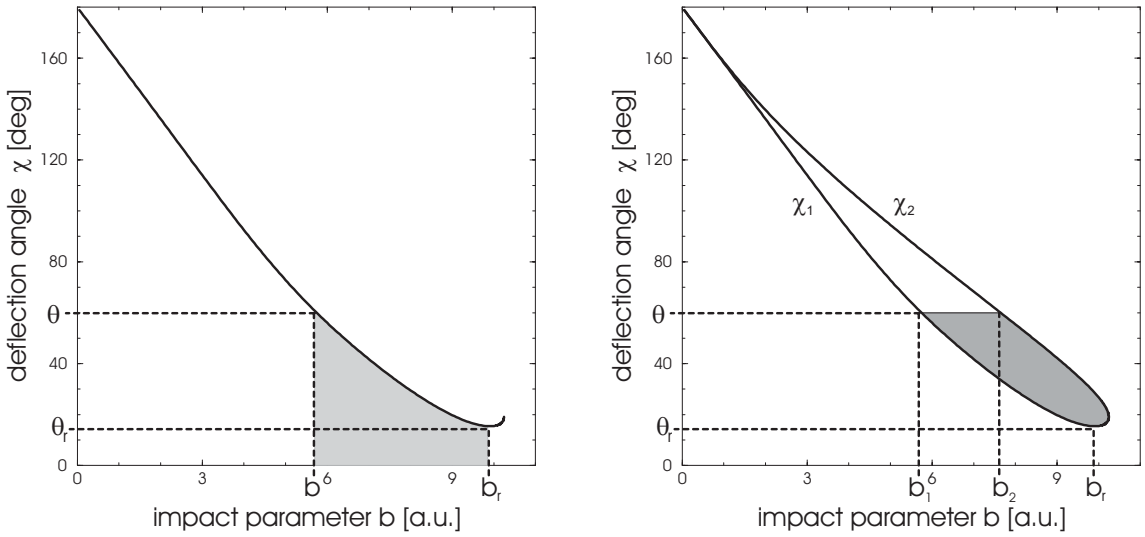


Figure 1.8: Left: Graphical illustration of Equation 1.14. The shaded area is, apart from constant addends, proportional to the phase of the corresponding trajectory. Right: Typical example for two deflection functions χ_1 and χ_2 for one Condon radius for a positive detuning. The difference in phase of the two trajectories is proportional to the shaded area.

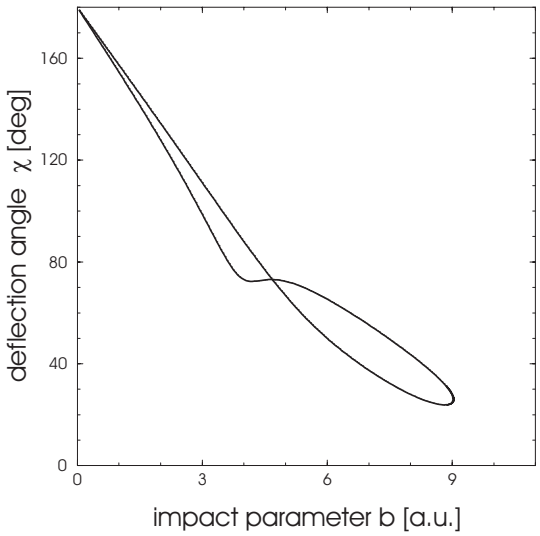


Figure 1.9: A situation in the KAr system where the two deflection functions cross. The collision energy is 1000 cm^{-1}, the detuning is 480 cm^{-1}.

For a derivation of this expression refer again to Appendix A. $\Delta\phi$ is directly proportional to the area that is comprised by the deflection function at the considered scattering angle, as illustrated in Figure 1.8. It changes with the scattering angle with an oscillation frequency that is given by the difference of the corresponding impact parameters and k. $\Delta\phi$ is strictly increasing for increasing scattering angles as long as the two deflection functions do not cross. In the case of a crossing, $\Delta\phi$ decreases for increasing scattering angles from the crossing point. An example for such a situation is shown in Figure 1.9. As can be seen from Equation A.3, $\Delta\phi$ depends mainly on the region of the potentials from the Condon radius to the classical turning point.

The differential cross section $\frac{d\sigma}{d\Omega}(\theta)$ is a measure for the intensity of elastically scattered atoms into a solid angle $d\Omega$ around the scattering angle θ. Classically, it is calculated

from the deflection function. Taking into account the probability of the optical excitation as calculated in section 1.1, and the phase corresponding to each trajectory results in

$$\frac{d\sigma}{d\Omega} = \left| \sum_j \sqrt{\left| \frac{b_j}{sin\chi (d\chi/db)|_{b_j}} \right| \cdot \frac{\pi(\vec{E}\vec{d}_j)^2}{2\hbar|\Delta H'|v(r_c)}} \cdot e^{i\phi_j} \right|^2 \tag{1.16}$$

with the sum including all trajectories j with deflection angle χ contributing to the scattering angle θ. Singularities in the differential cross section result classically in an infinite signal and are denoted as rainbow structures. They are found for instance at the smallest possible deflection angle ($d\chi/db) = 0$) and at extreme values of the potential difference ($\Delta H' = 0$).

Equation 1.16 is the basis for the discussion of differential optical collisions. When the scattering angle is scanned, the change of the relative phase results in interference structures in the differential cross sections. For linear polarized light, the measured signal depends on the relative orientation of $\vec{E}$ and $\vec{d}$. Polarization experiments for which the direction of $\vec{E}$ is varied, give information about the orientation of the transition dipole moments. The light contributes as well to the phase of the trajectories. When using elliptically polarized light, the oscillation maxima of the differential cross section can be shifted in analogon to a tunable interferometer

1.3 Quantum mechanical treatment and nonadiabatic couplings

For a quantitative description of optical collisions, differential cross sections are calculated from a given set of potentials using coupled channels equations. A detailed description of the procedure can be found in [Reb98]. Only a limited number of potential curves and eigenstates are included. This is a justified approximation since only eigenstates are neglected for which the coupling to the states of interest is much smaller than the distance of the corresponding potential curves. Furthermore, the hyperfine structure is neglected. The equations are solved for the limiting case of zero light intensity. As discussed in section 1.1, this is justified and implies a transition that is localized precisely at the Condon radius and neglects the modification of the potentials due to the interaction of the atoms with the light field. A significant influence on the interference pattern of differential cross sections is only expected for laser intensities that are a factor 10 higher than presently used [Reb03]. The coupling that is included at present is the spin-orbit coupling which is assumed to be independent of the internuclear distance.

The spin-orbit coupling is the cause for nonadiabatic transitions. It is relevant in the asymptotic parts of molecular potentials that connect to atomic states with a fine-structure splitting as Na(3p) and K(4p). In the case of alkali+rare-gas collisions, with a positive detuning the $B\Sigma_{1/2}$ state is excited. It is adiabatically connected to the $nP_{3/2}$ state of the free

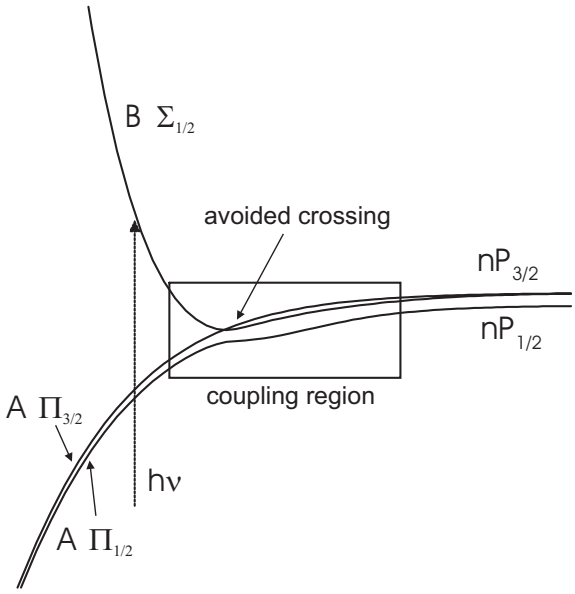


Figure 1.10: Region of coupling in which transitions from B$\Sigma_{1/2}$ to nP$_{1/2}$ can occur.

alkali atom. In the asymptotic parts of the potentials, where the angular momentum coupling scheme changes from Hund's case a or b to Hund's case e or c, the B$\Sigma_{1/2}$ potential is coupled to the nP$_{1/2}$ state with the coupling constant given by the spin-orbit splitting. The transition probability from B$\Sigma_{1/2}$ to nP$_{1/2}$ goes to zero for low collision energies approaching the extreme case of adiabaticity. For high collision energies, the B$\Sigma_{1/2}$ state is conserved which is expressed in the basis of the atomic states by the Clebsch-Gordan coefficients:

$$|B\Sigma_{1/2}\rangle = \sqrt{\frac{1}{3}}\ |\mathrm{nP}_{1/2}\rangle + \sqrt{\frac{2}{3}}\ |\mathrm{nP}_{3/2}\rangle. \tag{1.17}$$

Thus, a sudden passage through the coupling region leads to a characteristic transition probability of 1/3.

Another case for which the spin-orbit coupling introduces nonadiabatic transitions is an avoided crossing of the two curves with angular momentum projection $\Omega = 1/2$ which is present in some systems. The effectiveness depends on the energy and the details of the potentials in this region. This can lead to transition probabilities greater than 1/3 as observed in Na-Ar and Na-Kr collisions [Gro99b]. In collisions with molecules, the probability is furthermore a function of the rotational temperature of the molecules.

The two regions of transitions are indicated in Figure 1.10. Transition probabilities for alkali+rare-gas systems were determined in gas cell experiments [Hav86]. However, in these measurements the quite essential value of the collision energy cannot or only indirectly be determined. This is the major advantage of the method of differential optical collisions compared to previous experiments. The determination of the collision energy allows a direct comparison to theoretical calculations.

Chapter 2

Experimental method

2.1 Overview

The core of the experiment are the three beams that take part in the optical collision: the target beam, the projectile beam and the excitation laser (Figure 2.1). They intersect roughly at right angles (exact values can be found in Table 2.1). The scattered projectile atoms are detected by the detection laser in combination with the Rydberg detector. The scattering volume is defined as the region where all four beams overlap. The detector is rotatable around the axis of the laser beams to select a desired scattering angle. The detection is state selective as well as angular and velocity resolved. The scattering angle in the laboratory frame is measured relative to the projectile beam. The position of the detector as seen in Figure 2.1 corresponds to a negative scattering angle.

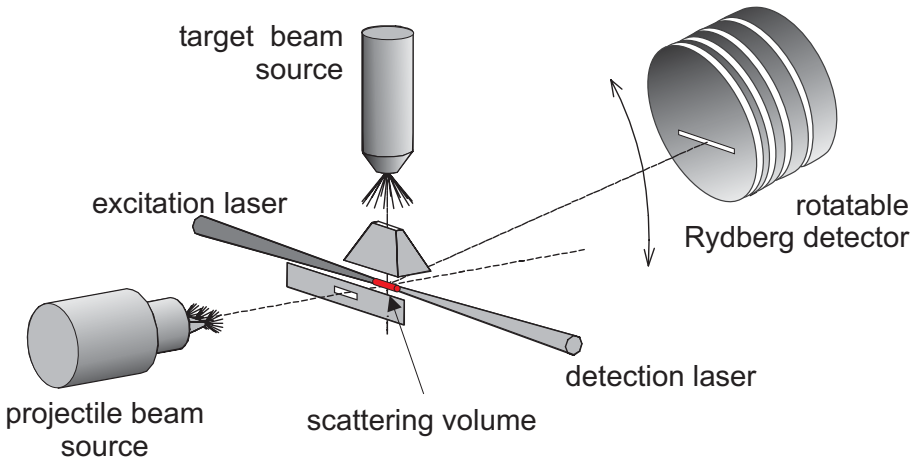


Figure 2.1: Principle of the experimental set-up.

Measurements that will be presented are the number of detected atoms as a function of

1. **the scattering angle** (differential cross sections): The collected data can be used to improve a given set of potentials.
2. **the energy of the excitation photon,** to probe the strength of the optical transition in dependence on the interatomic distance.
3. **the detected state** to measure nonadiabatic transition probabilities.

In order to completely characterize a collision between two particles, the velocity vectors of the particles as well as their internal states before and after the collision have to be known. In this experiment, the particles are prepared in their electronic ground state. When the optically excited collision complex separates, an excited state (Equation 0.3) of the scattered projectile atom is selected by the detection scheme. The target particle leaves the collision in its ground state. In measurements of atom-molecule collisions, it was ensured that no energy transfer into rotational or vibrational degrees of freedom of the molecule occurs. The directions of the target and projectile beam before the collision are fixed by apertures and the mean value of the velocity of the target atoms before the collision can be calculated. The velocity of the scattered projectile is measured by a time of flight analysis, and the direction is selected by the detector aperture. With these information, the remaining four parameters can be calculated from the conservation of energy and momentum, in particular the velocity of the projectile atom before the collision and thus the collision energy. In conclusion, a complete characterization of the observed collision is achieved.

Errors in the characterization of the collision event are introduced for example by systematic errors in the measurement of the scattering angle, the angle between the particle beams, the time of flight of the scattered projectile atoms and the corresponding distance, and the wavelength and polarization of the excitation photon. Furthermore, the experimental resolution of the kinematic quantities have to be taken into account. For this reason, it is necessary to measure or calculate the angular and velocity distributions of the particle beams, the dimensions of the scattering volume, and the dimensions of the detection aperture. Errors in all these quantities and distributions introduce errors into the interpretation of the experimental results. Their determination together with the corresponding uncertainties will be presented in the corresponding sections of this chapter.

angle between target and projectile beam	90.1°-90.7°
angle between laser and particle beams	90°
dimensions of scattering volume	ø 1 mm, length 10 mm
accessible laboratory scattering angle	-18°…92°

Table 2.1: General quantities of the experimental set-up

2.2 Laser system and optical components

The two laser pulses are produced by dye lasers[1] which are pumped by an excimer laser[2]. The excimer laser emits pulses at a wavelength of 308 nm with an energy of around 300 mJ. The maximum repetition rate is 80 Hz [Lam85]. The pump pulse is divided by a beam splitter to pump both dye lasers simultaneously. Dyes that are used for the different projectile atoms are given in Table 2.2. The resulting pulses of the dye lasers have a duration of 10-20 ns with a typical maximum energy of 5 mJ. The bandwidth of the lasers is 0.2 $cm^{-1}$and the wavelength reproducibility 0.0006 nm [Lam87].

For an overview of the laser systems and optical components refer to Figure 2.2. The lasers and the vacuum chamber are placed in two rooms which results in a pathway of around 12 m of the light. The frequency filter for the excitation laser benefits from the pathway. It is described below in more detail. To decrease resulting spatial instabilities of the laser beams at the position of the vacuum chamber, they are enlarged by telescopes to a diameter of 1-2 cm. For manipulating the polarization of the lasers, polarizers in combination with fresnel rhombs are used. The fresnel rhombs are turned to change the plane of polarization of the linear polarized light. The fraction of linear polarized light thus produced is more than 99%. The direction of the polarization is adjustable with

[1] Dye Laser FL 3002, Lambda Physik, Göttingen
[2] Excimer laser EMG 201 MSC, Lambda Physik, Göttingen

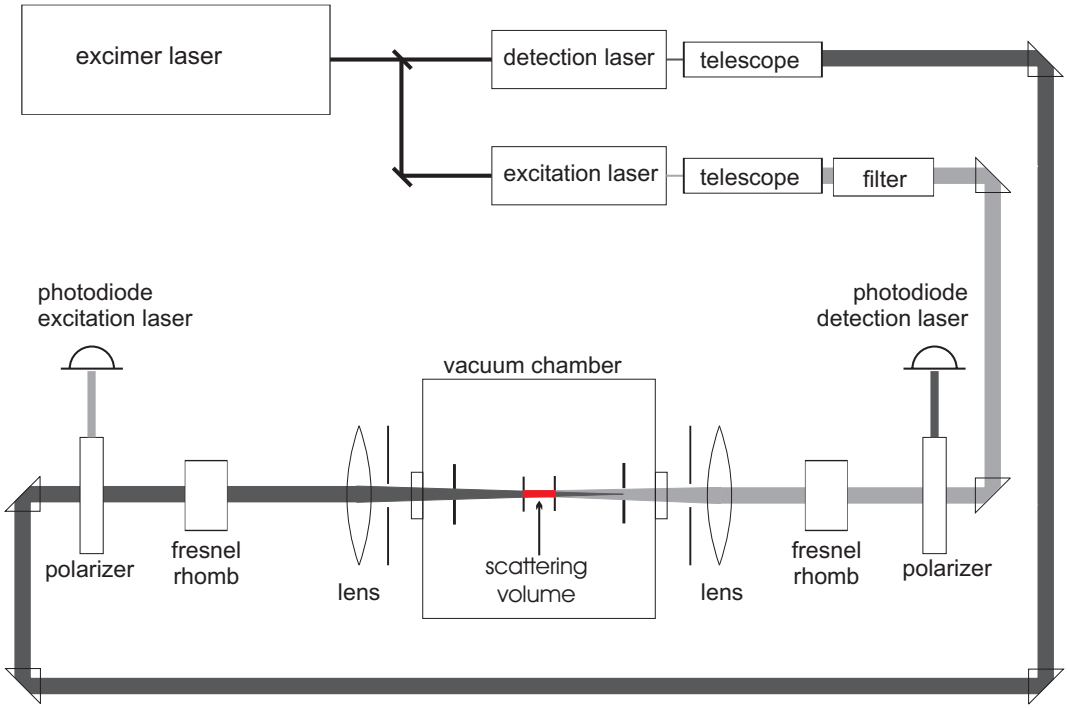


Figure 2.2: Layout of the optical components.

projectile	excitation laser	detection laser
K	Pyridine 2	Coumarin 47
	695-790 nm	440-484 nm
Na	Rhodamine 6G	DPS
	569-608 nm	399-415 nm
Ca	Coumarin 2	DMQ
	432-475 nm	346-377 nm

Table 2.2: Laser dyes used for measurements with different projectile atoms and the wavelength at which they operate [Bra94].

an accuracy of 1°. The lasers enter the vacuum chamber through plan parallel plates with an anti-reflection coating so that intensity variations with the wavelength due to interference in the plates are excluded. By a combination of lenses and apertures inside the vacuum chamber, it is ensured that the lasers overlap with the particle beams and that the scattering volume is confined to a diameter of 1 mm. The power density in the scattering volume is typically 2 MW / cm^2. Iris diaphragms outside the vacuum chamber are placed in line with the inner apertures for easier adjustment of the laser beams and to avoid stray light in the vacuum chamber. Photodiodes equipped with suitable glass filters monitor the intensities of the lasers after the passage through the vacuum chamber.

Elimination of resonant light

Besides the peak at the selected wavelength, the lasers produce a broad amplified spontaneous emission (ASE) background over the entire spectrum of the dye with intensities more than a factor 10^3 smaller than the peak intensity. The resonant fraction of the ASE of the detection laser can excite the projectile atoms K and Na as free atoms which causes a background signal. Thus, the resonant wavelengths have to be suppressed. For the measurements with Ca a suppression is not necessary because the corresponding transition of the free calcium is dipole forbidden. In previous experiments with Na, the resonant frequencies were eliminated by a sodium vapor cell. The vapor absorbed the resonant light and reemitted it in all directions leading to an efficient suppression of the resonant fraction of the laser. This solution requires a different vapor cell for every projectile. Since the range of projectile elements was expanded with this work from Na to K and Ca, a filter suitable for a broad range of wavelengths was designed (Figure 2.3): By backreflecting the beam through two SF 10 dispersion prisms[3], a dispersion of 10^{-3} rad / nm at the Na D1-line and of $6{\cdot}10^{-4}$ at the K D1-line is reached [LIN03]. Because of the long pathway of the laser beam, it is easily possible to suppress the resonant fraction with iris diaphragms before the dispersion prisms and in front of the vacuum chamber down to a detuning of 120 cm^{-1} even without taking much care about the adjustment. If measurements with a smaller detuning should be made, more prisms can be employed or the diameter of laser beams can be decreased. A drawback of this solution is the need of readjusting the mirrors after a change of the detuning.

[3]LINOS, Göttingen

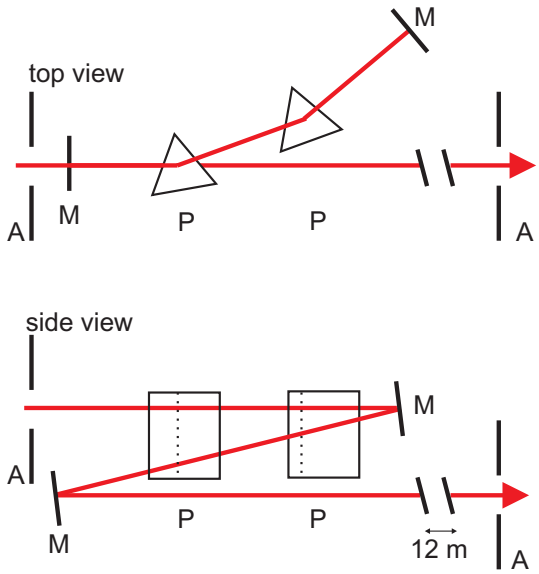


Figure 2.3: The set-up to filter the excitation laser. P indicates a dispersion prism, S a mirror, A an iris diaphragm. Shown is only the pathway of the beam for the selected wavelength.

Calibration

The wavelength of both lasers is calibrated by scanning the detection laser over Rydberg series of the projectile and measuring the yield of Rydberg atoms. For this, the excitation laser is set to a chosen detuning, so that excited projectile atoms A^* are produced in an optical collision. The detection laser is scanned over Rydberg series of transitions $\mathrm{A}^* + h\nu_{\mathrm{detection}} \rightarrow \mathrm{A}(nl)$, as shown in Figure 2.4. With the measured spectrum, the detection laser is calibrated. To calibrate the excitation laser, the detection laser is scanned over a different Rydberg series corresponding to two-photon transitions $\mathrm{A} + h\nu_{\mathrm{excitation}} + h\nu_{\mathrm{detection}} \rightarrow \mathrm{A}(nl)$ from the ground state of the projectile to a Rydberg state (see Figure 2.5). As the detection laser is calibrated already, the wavelength of the excitation laser can be calculated. Alternatively, the excitation laser can be calibrated by tuning the laser to a resonant transition from the ground state to the excited state of the projectile by observing the fluorescence from the projectiles through a window in the vacuum chamber. However, this method is suitable only for sodium with the transition being in the yellow region of the visible spectrum. The transitions of K and Ca are near the infrared and the UV, respectively so that the fluorescence cannot be perceived with the bare eye.

The energies $T_{n,l}$ of the Rydberg states with principal quantum number n and angular momentum quantum number l are calculated according to the formula

$$T_{n,l} = T_\infty - \frac{R_m}{(n-\delta_l)^2} \tag{2.1}$$

where T_∞ is the ionization energy and δ_l is the corresponding quantum defect. $R_m = R_\infty/(1+\frac{m_e}{m})$ is the Rydberg constant for the nuclide with mass m, m_e being the mass of the electron and R_∞ the Rydberg constant. Ionization energies are taken from [Bas75], quantum defects from [Rad85]. The uncertainties in the quantum defects of a Rydberg series

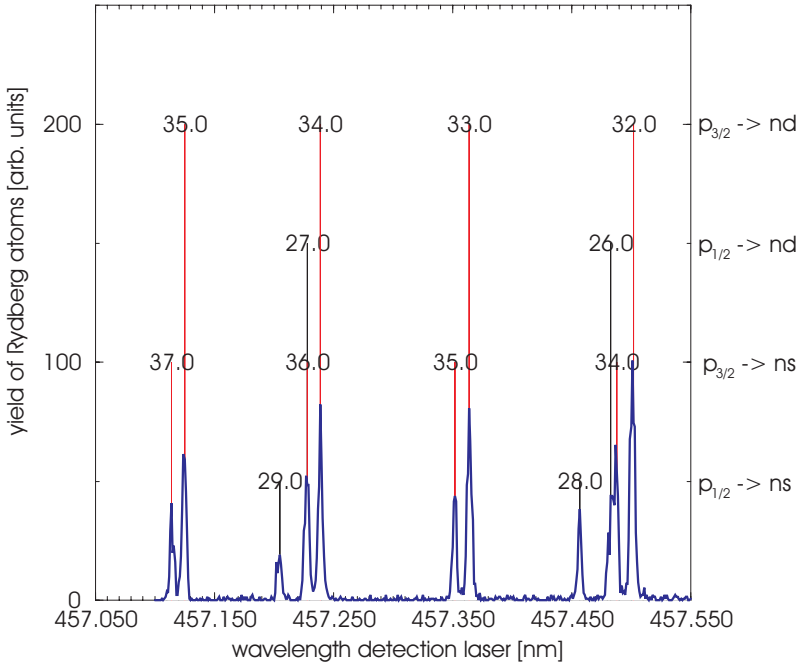


Figure 2.4: Spectrum of transitions from K(4p) to a Rydberg state nl. Vertical lines indicate the calculated position of the peaks. The principal quantum number n of the Rydberg state is given above the lines. The fine-structure state of the detected state and the angular momentum l of the Rydberg state are indicated at the right side of the graph. Detuning of the excitation laser is 220 cm^{-1}, laboratory scattering angle is 5.4°. Most measurements on this system were made using the $K(4p_{3/2}) \rightarrow K(35d)$ transition.

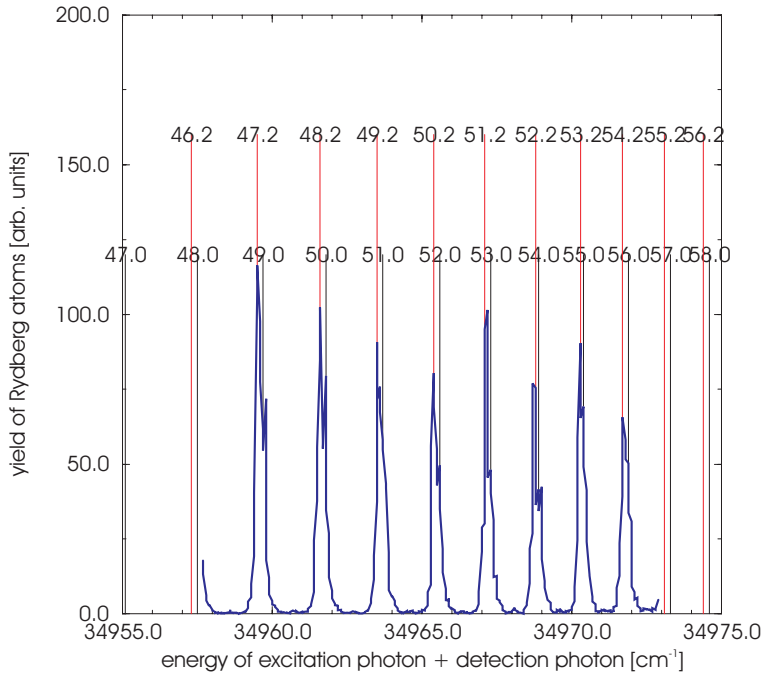


Figure 2.5: Spectrum of transitions from K(4s) to a Rydberg state nl. The wavelength of the detection laser is scanned. Vertical lines indicate the calculated position of the peaks. The principal quantum number n is given above the lines followed after a dot by the angular momentum l. Measurement is without target gas in forward direction of the potassium beam.

projectile	uncertainty excitation laser [cm^{-1}]	uncertainty detection laser [cm^{-1}]
K	0.07	0.2
Ca	0.3	0.3
Na	0.1	0.2

Table 2.3: Uncertainty in the frequency of the lasers. Included is the uncertainty of the quantum defects which are used to calculate the Rydberg spectra, the wavelength reproducibility of the lasers and a typical drift of the wavelength during operation.

introduce uncertainties in the position of the calculated lines and thus in the calibration. More sources for uncertainties of the wavelength are the reproducibility of the lasers in wavelength and a drift of the wavelength that is observed by calibrating the lasers after different durations of operation. A typical range for this drift is 0.004 nm. These three effects give the total uncertainty of the wavelength which is given in Table 2.3 for the different projectiles. It is in the order of 0.1 cm^{-1}.

2.3 Detection scheme

Na(3p) and K(4p) have a lifetime in the order of 10^{-8}s [Vol96]. With the velocity being in the order of 10^3 m / s, they decay back to the ground state before leaving the scattering volume. To make a detection nevertheless possible, the detection laser transfers the collision products into Rydberg states. The lifetime of the Rydberg atoms is long enough to reach the detector while the fraction of the Rydberg atoms that are scattered elastically by the background gas on the way to the detector is neglectable even for higher pressures than present [Klo96]. Inside the detector, Rydberg atoms are ionized and detected by a channeltron. Alternatively, ground state projectile atoms can be detected if the photon energies of detection and excitation laser add up to a transition from the ground state to a Rydberg state. If the detection wavelength is chosen appropriately, only one transition contributes to the signal.

The detector is shown in Figure 2.6. It consists of an array of nickel meshes serving as electrodes and a channeltron[4]. Between the first two meshes, the electric field force of about 170 V / mm is high enough to field ionize Rydberg atoms with a quantum number of $n = 15$ and higher [Gun93]. The ionization takes place in the vicinity of the first mesh. The ions that are thus produced inside the detector are focussed onto the channeltron. The first and fourth mesh are set to a positive potential of +60 V and +100 V, respectively (all potentials are given with respect to the ground potential of the vacuum chamber). They shield the channeltron from positive ions that might be present in the vacuum chamber. The channeltron itself is set to a negative potential of -2.7 kV, so that electrons that might enter the detector do not reach the channeltron. The channeltron is not visible from both the beam sources so that neutral particles from the beams do not reach the channeltron

[4]Elektronenvervielfacher-Kanal Typ KBL10RS, Dr. Sjuts Optotechnik GmbH, Göttingen

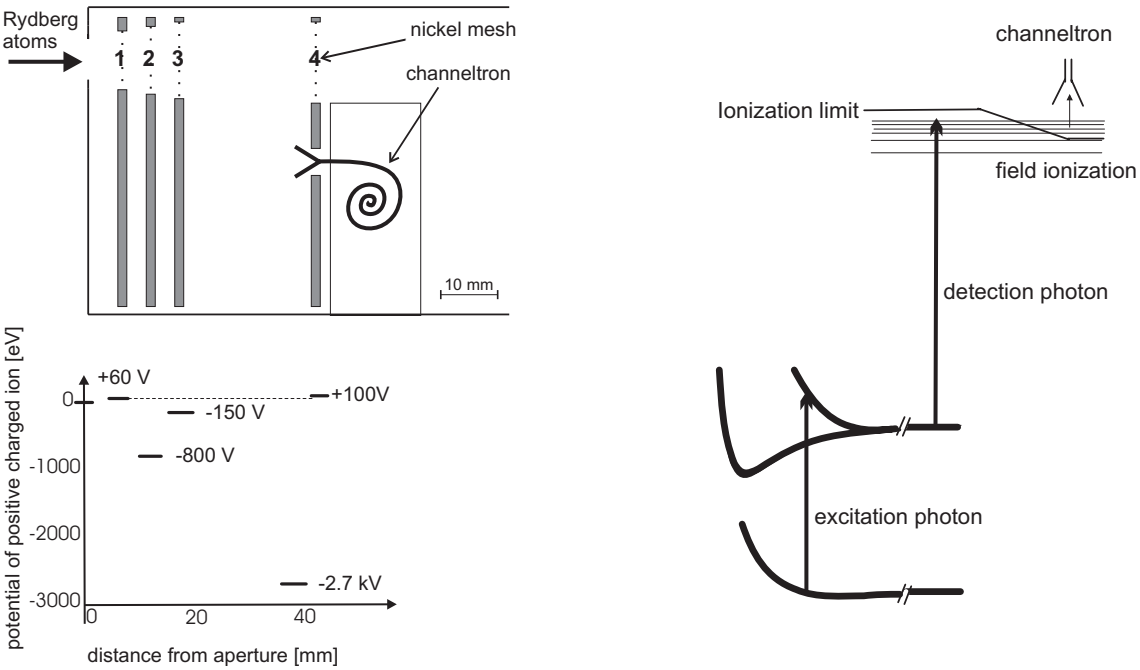


Figure 2.6: The Rydberg detector. The figure on the top left shows the design of the detector. The potentials of the meshes are shown in the figure below. The dashed line indicates the energy of the ions inside the detector. The figure on the right illustrates the detection scheme by showing the potential energies.

either. From the Rydberg atoms, a fraction of 70% reaches the detector under typical experimental conditions and 70% of those are counted by the channeltron leading to a detection efficiency of around 50% [Mae94].

The velocity of the scattered atoms is basically determined by the time of flight t_{run} from the scattering volume to the first mesh of the detector. t_{run} is in the order of 100 µs and the distance is 70 mm. To determine t_{run}, corrections to the actual measured time t_{exp} have to be made. t_{run}=0 is the time at which the Rydberg atoms are produced, i.e. the arrival of the laser pulse in the scattering volume. It is determined by the use of a photodiode inside the detection laser. t_{exp} is the time difference between the photodiode pulse to the amplified pulse from the channeltron (see Figure 2.7) measured by a multichannel analyzer PC-Card[5] (MCD-2 card). To t_{exp}, the running time of the photodiode pulse to the card and the difference in processing time of the trigger and the signal pulse of the MCD-2 card [FAS] have to be added. The time of flight of the light from the laser to the scattering volume, the time of flight t_{ion} of the ions inside the detector (which is different for every projectile), the running times of the pulse in the cables, and the processing time of the preamplifier have to be subtracted. Combining all corrections, the time of flight of the atoms from the scattering volume to the first mesh of the detector t_{run} is

$$t_{run} = t_{exp} - t_{ion} - 68\,\text{ns} \tag{2.2}$$

[5]MCD-2 Dual Input Multiscaler / Multichannel Analyzer, FAST ComTec GmbH, Oberhaching

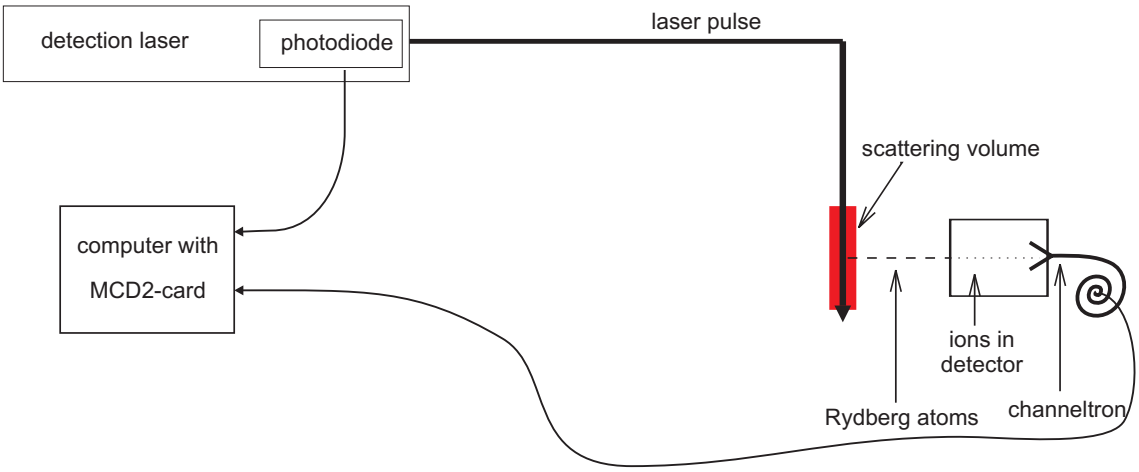


Figure 2.7: Determination of the time of flight of the Rydberg atoms

t_{ion} was calculated by simulating the pathways of the ions inside the detector with the software package SIMION [6]. The values of t_{ion} in Table 2.4 are mean time of flights for an aperture of 3 mm x 30 mm. They are used to calculated the velocity. The uncertainties in the determination of the time of flight sum up to a total uncertainty of 80 ns in t_{run}. The path length is determined with an accuracy of 0.3 mm. For a velocity of 1000 m/s this results in a total uncertainty of 0.4%.

The assumption of nominal values for the traveling distance of the Rydberg atoms and the time of flight of the ions is an approximation: The traveling distance of the atoms depends on the point of origin in the scattering volume and the entrance point at the detector. t_{ion} depends on the point of origin of the ions. The errors thus made are corrected for when experimental results are compared to calculations as described in more detail in section 2.9.

Figure 2.4 and Figure 2.5 show two typical measured spectra of detected transitions. In Figure 2.4, K($4p_{1/2,3/2}$) is detected after an optical collision, in Figure 2.5, K(4s) is detected directly. For each line, the detected state and the Rydberg state are given. If the wavelength of the detection laser is not chosen carefully, more than one state can be detected as can be seen for example in the second line from the right in Figure 2.4. On the other

[6] D. A. Dahl and J E Delmore, *Simion Electrostatic Lens Analysis and Design Program*, Idaho Falls, 1983

Element	Time of flight of ions inside Rydberg detector [ns]
K/Ca	1113
Na	840
Li	461

Table 2.4: Time of flight of ions from the first mesh of the Rydberg detector to the channeltron. Mean values for an aperture of 3 mm x 30 mm.

hand, isolated lines are found that can be assigned to one detected state, for example both the lines around 457.35 nm which were used for most measurements on the KAr system.

In order to change the detected scattering angle, the detector is mounted on a swivel arm. The scattering angle is given with respect to the forward direction of the projectile beam which is measured by a direct detection of the ground state projectile. The accuracy of the 0° scattering angle and the accuracy of the swivel arm add up to an uncertainty of 0.3° in the given scattering angle.

The detector is also used to determine the angle between the two particle beams. This has to be done regularly because the angle depends on the mounting of the beam sources and can vary up to 1°. A 0.8 mm x 8 mm aperture is mounted on the swiveled support of the detector. With a direct detection of the ground state projectile, the direction of the projectile beam is determined. Without changing the aperture, the Rydberg detector is replaced by an ionization detector to measure the direction of the target beam. Thus, the angle between the beams is measured with an accuracy of 0.3°.

2.4 Projectile beam

The projectile beam sources consist basically of two heatable stainless steel cylinders: the reservoir and the head. The two parts are heated to different temperatures which are measured with thermocouples. The temperature of the reservoir determines the vapor pressure of the projectile atoms inside the reservoir and the head and thus the particle density in the scattering volume. From the reservoir, the atoms reach the head which is heated to a higher temperature. The reason for the two chamber configuration is the resulting decrease of the fraction of dimers in the beam which cause a background signal. For typical temperatures, the fraction is decreased by a factor of 30 for K and a factor of 60 for Na to 0.03% (Table 2.6). Calcium atoms are less likely to form dimers, even without the two chamber configuration the fraction does not exceed 0.001%. Apart from the fraction of dimers, the temperature of the head determines the velocity distribution of the projectile atoms. The atoms leave the head through a line of capillaries. The sources are mounted inside a cooled copper chamber with an aperture that confines the projectile beam to the scattering volume. On the cold copper surface, the projectile atoms that do not leave the chamber directly are deposited so that the projectile background pressure in the scattering volume is reduced.

There are two types of projectile beam sources (Figure 2.8) that are different, however, only in the technical realization. While for potassium and sodium the maximum required temperature of the reservoir is about 750 K, for calcium temperatures up to 1100 K are needed. Hence, the sources for potassium and sodium can be heated by commercial heating devices (heating cartridge[7] and heating cable[8]), while for the calcium source a

[7] T+H HLP 0203, Türk+Hillinger GmbH, Tuttlingen
[8] 2ZE / 15 / 25-44 / Ti / CW2 15, Thermocoax, Stapelfeld

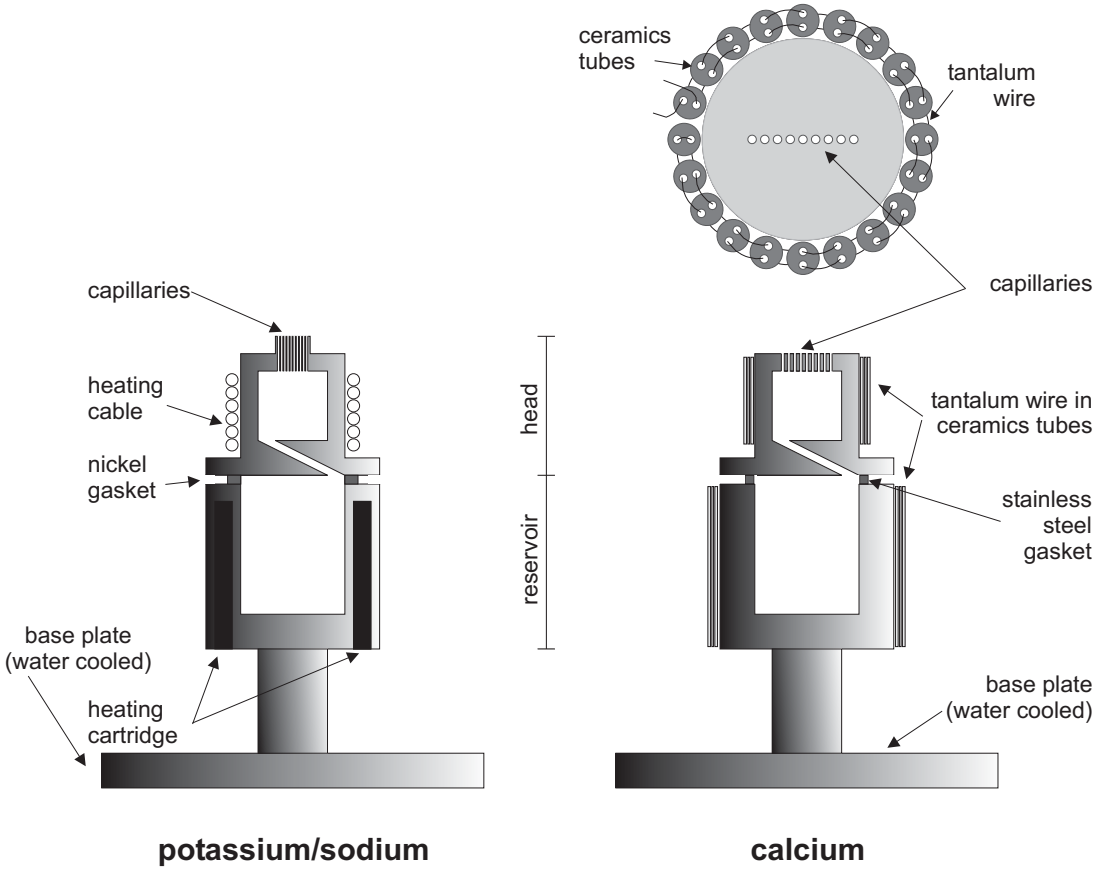


Figure 2.8: Front view of the projectile beam sources and top view of the calcium beam source.

	Potassium / Sodium	Calcium
reservoir		
heating device	heating cartridge	tantalum wire (ø0.5 mm)
temperature	550-750 K	970-1070 K
volume	11.4 cm^3	11.4 cm^3
head		
heating device	heating cable	tantalum wire (ø0.5 mm)
temperature	850-970 K	1040-1140 K
distance capillaries-scattering volume	71.2 mm	63.6 mm
diameter and length of capillaries	ø0.8 mm; 8 mm	ø0.8 mm; 5 mm
number of capillaries	10 per 10.6-11.8 mm	9 or 10 per 9 mm
gasket	nickel ring	stainless steel ring
particle density in beam	$2 \cdot 10^{21}$-$3 \cdot 10^{22}$ / m^3	$1 \cdot 10^{21}$-$8 \cdot 10^{21}$ / m^3
mean velocity	730-1030 m / s	800-840 m / s
aperture	1 mm x 10 mm	1 mm x 10 mm
distance aperture – scattering volume	7.2 mm	7.2 mm

Table 2.5: Relevant quantities of the projectile beam sources

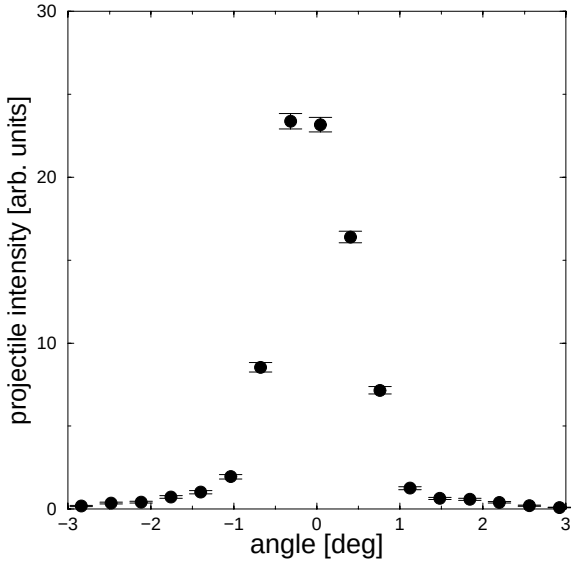


Figure 2.9: Profile of the projectile beam. Full width at half maximum is 1.3° which includes the angular resolution of the detection aperture of 0.7°.

tantalum wire is used. A second difference is the gasket which seals the reservoir to the head. It is a ring made of nickel for potassium and sodium. Nickel has a high enough melting point of 1728 K being nevertheless soft enough to serve as a gasket. With calcium, nickel cannot be used because it forms an alloy with calcium with a melting point as low as 878 K at a weight percent of nickel of 16% [Mas90]. After use, the melted alloy makes it impossible to separate the head from the reservoir for refilling. Thus, a ring made of stainless steal is used as a gasket in the case of calcium. Concerns that the hard material does not seal satisfactorily have not been affirmed.

The beam profile as shown in Figure 2.9 is measured by directly detecting the projectile atoms by a two-photon transition as a function of the laboratory scattering angle. The angular resolution of the aperture of the detector was 0.7° for this measurement. The measured full width at half maximum is 1.3°.

The angular distribution of one capillary was calculated representatively for sodium (left

projectile	T_r [K]	p_r [mbar]	fraction of dimers in reservoir [%]	T_h [K]	fraction of dimers in head [%]
K	590	0.62	1.0	850	0.03
Na	665	0.40	2.0	970	0.03
Ca	1050	0.68	0.0003	1130	<0.0009

Table 2.6: Vapor pressure [Nes63] and fractions of dimers [Var87, All04] in reservoir and head for typical temperatures of the projectile sources. T_r: temperature of reservoir, T_h: temperature of head, p_r: vapor pressure in reservoir

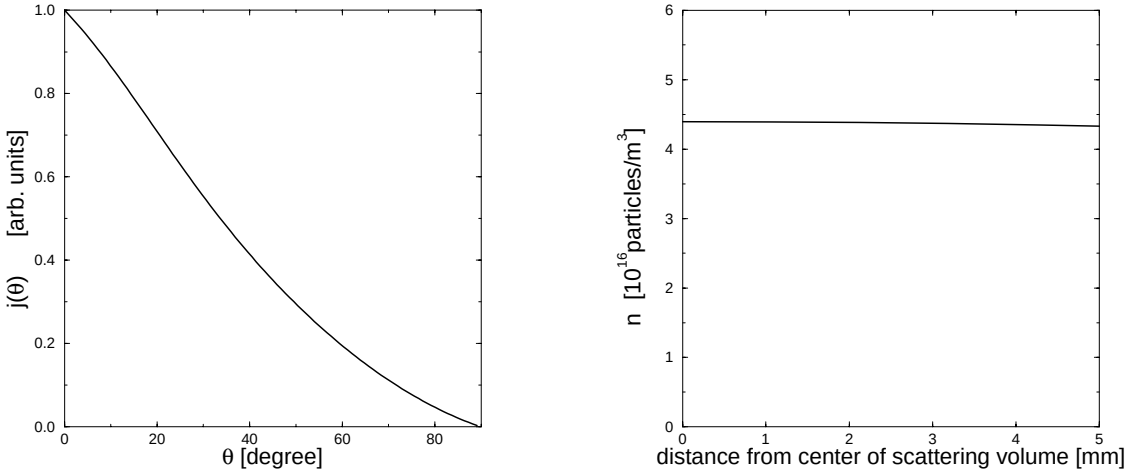


Figure 2.10: Calculated angular distribution of projectile atoms (left) and the resulting density over the scattering volume (right) shown representatively for sodium.

part of Figure 2.10). The concepts for the calculation are described in [Gol04, Hof95, Mil88]. The density distribution in the scattering volume along the axis of the lasers as it results from the contribution of all capillaries is presented in the right part of Figure 2.10. The density is almost constant over the scattering volume: In the outmost parts of the scattering volume the density is 3% lower than in the center.

For low vapor pressures, the projectile beam is in the effusive regime. Thus, the velocity distribution $p(v)$ of the particles can be described by a Maxwell-Boltzmann distribution

$$p(v) \sim v^2 e^{-\left(\frac{v}{v_w}\right)^2} \tag{2.3}$$

with $v_w = \sqrt{\frac{2 \cdot k_B \cdot T_h}{m_1}}$ and T_h the temperature of the head. However, this does not describe the real velocity distribution correctly. Firstly, the temperature is measured at the outside of the head, so the real temperature is most probably higher. Secondly, for the sake of high projectile densities, the projectile source is operated at higher vapor pressures than those for which a purely thermal behavior is expected. Both effects lead to higher velocities than calculated with Equation 2.3. To derive a more realistic assumption, the velocity distribution of the projectile atoms before the collision is measured by detecting the projectile atoms directly by a two-photon transition in forward direction of the projectile beam. Thus, a fraction α of the projectile atoms in the scattering volume V is transferred into a Rydberg state, depending on the intensity and duration $\Delta t = 10^{-8}$ s of the laser pulses. There are $n(v) \cdot V$ atoms in the scattering volume, where $n(v)$ is the velocity-resolved density distribution of the projectile atoms, and $V = 2.5\pi \cdot 10^{-9}\,\mathrm{m}^3$ the volume of the scattering volume. Additionally, $v \cdot n(v) \cdot A \cdot \Delta t$ atoms enter the scattering volume during the laser pulse. $A = 10^{-5}\,\mathrm{m}^2$ is the projection of the scattering volume onto a plane perpendicular to the projectile beam. The atoms have a mean length of flight through the scattering volume of $\frac{2}{\pi} \cdot d$ ($d = 10^{-3}$ m is the diameter of the scattering

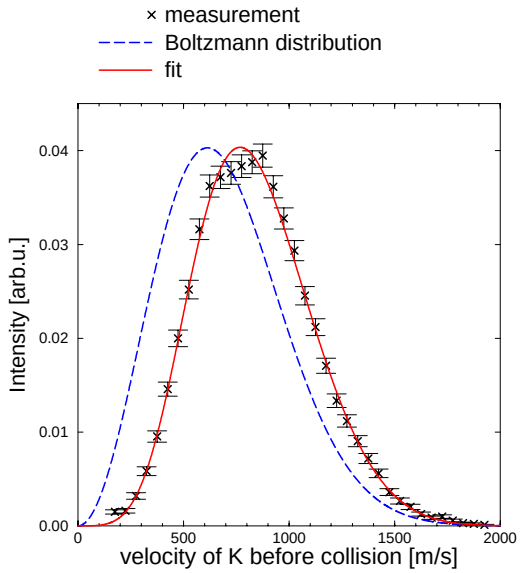


Figure 2.11: Comparison of measured velocity distribution of the flux of potassium atoms in comparison with a Maxwell-Boltzmann distribution (dashed line) for a measured temperature of 887 K of the head of the beam source and a fit according to Equation 2.4 (solid line).

volume) and thus a mean time of dwelling in the scattering volume of $\frac{2d}{\pi v}$. For a typical velocity of 1000 m / s, this is long compared to the duration of the laser pulse. So the atoms that additionally enter the scattering volume are still there when the laser pulse is over. However, for them the mean pulse duration is only half of the real pulse duration. This can be combined to the intensity of the signal $I(v)$

$$\begin{aligned} I(v) \quad &\propto \quad n(v)\cdot V\cdot\alpha + v\cdot n(v)\cdot A\cdot\Delta t\cdot\frac{\alpha}{2} = \\ &\alpha\cdot n(v)\cdot(\pi\cdot 2.5\cdot 10^{-9}m^3 + v\cdot 5\cdot 10^{-14}m^2/s). \end{aligned} \tag{2.4}$$

Thus, for the velocity range that is relevant for the collisions (i.e. up to 2000 m / s), the second term of Equation 2.4 can be neglected. In the above considerations, the atoms that leave the scattering volume are not accounted for. Their number is a fraction of the second term in Equation 2.4 which makes its neglection even more justified. In conlculsion, the velocity distribution of the measured signal is directly proportional to the velocity distribution of the density of the projectile atoms before the collision. For a description of $I(v)$, the function

$$\mathrm{I_{fit}(v)} \sim \mathrm{v^2 e^{(p(v))}} \tag{2.5}$$

is fitted to the measured data where the fitting parameters are the coefficient of a polynomial of fifth grade $p(v)$. A measured velocity distribution is shown in Figure 2.11 together with the fitted function in Equation 2.5 and the Maxwell-Boltzmann distribution (Equation 2.3) of the measured temperature. Indeed, the velocity is higher than expected from a thermal distribution and the description by the fit is therefore necessary and realistic.

2.5 Target beam

Argon beam source

The argon beam is produced by a nozzle[9] in combination with a skimmer (Figure 2.12). The nozzle is pulsed to reduce the pressure of the background gas being triggered by a commercial control unit[10]. The design of the source is such that the expansion of the beam is supersonic [Hoh95, Weh95]. A detailed treatment of supersonic beams is left out here but can be found in [Mil88]. The velocity distribution $p(v)$ of a supersonic beam can be approximated by a Gaussian:

$$p(v) \propto e^{-\frac{m(v-v_\mathrm{m})^2}{2k_\mathrm{B}T_\mathrm{t}}}. \tag{2.6}$$

m is the mass of the atom, k_B the Boltzmann constant. The width is given by the translational temperature T_t. The mean velocity v_m is higher than the mean velocity of a corresponding thermal distribution. The parameters v_m and T_t depend on physical properties of the gas, the pressure in the reservoir, the diameter of the nozzle, and the temperature of the reservoir. Typical calculated values for an argon beam are:

$$v_\mathrm{m} = 540\,\mathrm{m/s} \qquad\qquad T_\mathrm{t} = 4.5\,\mathrm{K}.$$

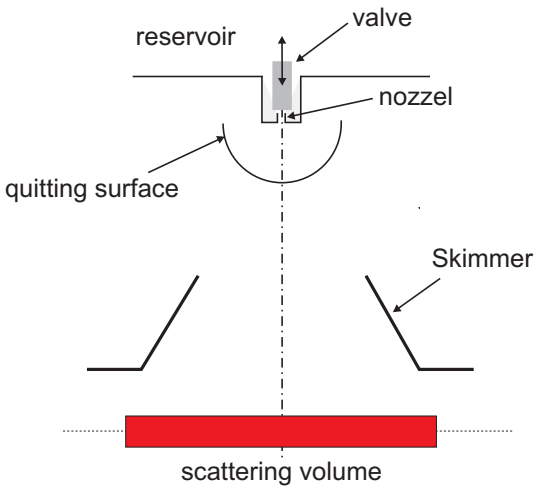
The angular distribution $I(\theta)$ is given by

$$I(\theta) \propto \cos^2(1.15\theta). \tag{2.7}$$

For a typical distance of the nozzle from the scattering volume this results in a target density of 80% at the outmost parts of the scattering volume compared to the one in the center. Angular distribution and density distribution over the scattering volume are shown in Figure 2.13.

It turned out that the velocity distribution given by Equation 2.6 is not realistic if the pressure in the reservoir exceeds a critical value. A reason for this may be found in the expansion of the so-called quitting surface with increasing pressure in the reservoir. Following the definition of [Mil88], the quitting surface divides the region of continuum flow from the region of free molecular flow. Having passed the quitting surface, the atoms are assumed not to undergo collisions anymore. In Figure 2.12 the quitting surface is indicated by the arc. The distance of the quitting surface to the nozzle increases with the pressure in the reservoir. If the quitting surface reaches the skimmer, the expansion can be disturbed so that no supersonic beam is established. Clearly, a critical reservoir pressure has to be found for which the argon velocity is still under control.

[9] series 9 high speed solenoid nozzle, General Valve, Fairfield
[10] IOTA pulse driver, General Valve, Fairfield



aperture of skimmer	5.38 mm x 0.76 mm
inclination of skimmer	53°
distance skimmer – scattering volume	5.02 mm
distance nozzle – scattering volume	12.5 mm
dimensions of nozzle	diameter: 0.2 mm
pressure in reservoir	100-800 mbar

Figure 2.12: Design of argon beam source with relevant quantities of the source.

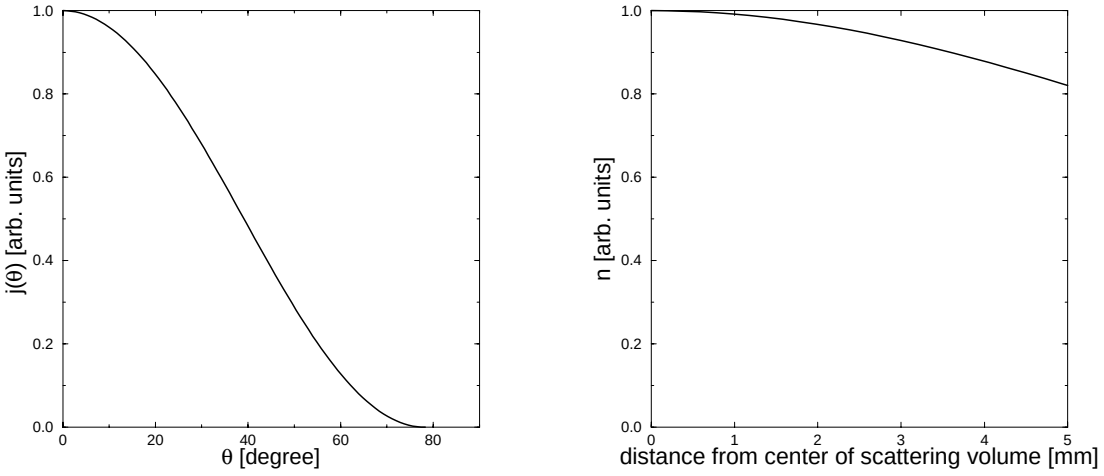


Figure 2.13: Calculated angular distribution of argon atoms (left) and the resulting density over the scattering volume (right). Both distributions are normalized to the values in forward direction.

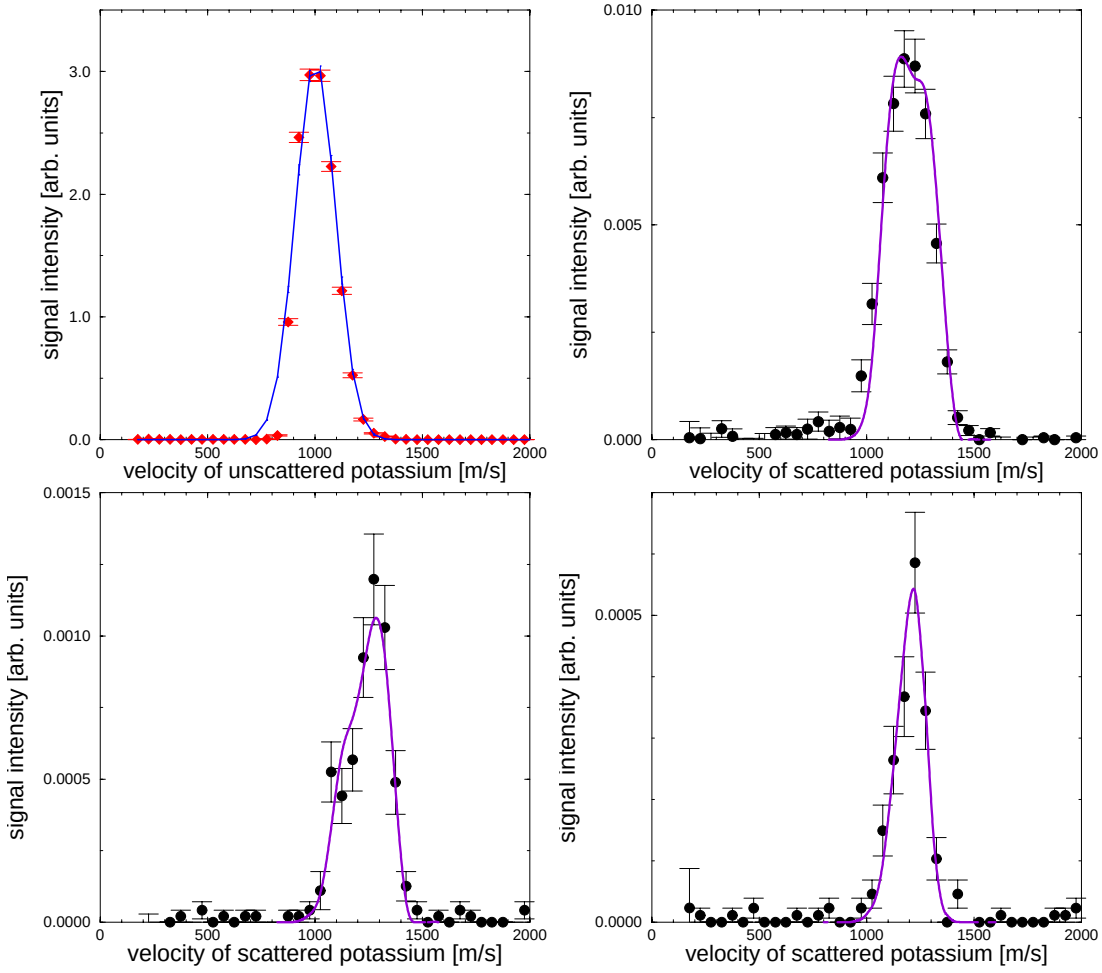


Figure 2.14: Experimental test of argon velocity distribution for three different scattering angles. Top left: measured velocity of potassium before collision (data points with error bars). The line describes the velocity distribution by a Gaussian. Top right to bottom right: Comparison of calculated (line) and measured (data points with error bars) velocity of scattered potassium atoms after optical collision. Laboratory scattering angle is 18°, 27°, and 34°, respectively from top right to bottom right. Detuning of the excitation laser is 480 cm^{-1}.

The experimental determination of the argon velocity was achieved indirectly: The velocity of the potassium atoms before the collision was measured by a two-photon excitation of the ground state potassium into a Rydberg state. The resolution was increased by a chopping wheel inserted into the projectile beam which is described in detail in [Gol04]. Thus, the velocity distribution before the collision could be described by a Gaussian with a maximum at 1002 m/s and a full width at half maximum of 219 m/s (see Figure 2.14 top left). Assuming a supersonic argon beam, the velocity of the postassium after an optical collision was calculated taking into account the experimental resolutions. Results for three different scattering angles with an argon pressure of 100 mbar are presented in Figure 2.14. It was found that the potassium velocity could be reproduced within ± 3 m/s with an error of ± 4 m/s. This can be transformed into an uncertainty of the argon velocity of ± 8 m/s. However, the uncertainties of the quantities that are needed for the convolution of the theoretical differential cross sections to get the velocity distribution after the collision are estimated to sum up to a total uncertainty of ± 15 m/s in the argon velocity at this pressure. In comparison, for an argon pressure of 150 mbar and 250 mbar, the measured velocities were found to be shifted by 20 m/s and 35 m/s, respectively, towards lower values. Thus, the argon velocity can be assumed to be 33 m/s and 58 m/s lower than the velocity of a supersonic beam. The exact meachnisms that lead to a slower argon beam, however, had not been studied, so that the velocity distribution is questionable for pressures exceeding 100 mbar. Almost all measurements were performed with an argon pressure of 100 mbar or less. In the experiments with CaAr, a background signal that is negligible in the other experiments dominated over the signal of an optical collision at argon pressures of 100 mbar. Therefore, a higher Ar pressure was exeptionally used. Assuming a thermal velocity distribution of the argon beam as the worst case, the resulting systematic errors of the calculated collision energies are estimated to be in the order of 100 cm^{-1}.

Molecular target beam source

In previous measurements, the atomic target beam source was also used for molecular targets. However, it turned out that it was not possible to produce a supersonic beam for molecular gases under the present experimental conditions. Therefore, a thermal beam source is used in measurements with molecular targets for which the kinematic quantities are well defined accepting the drawback of a wider velocity distribution.

While the beam is also pulsed, the design is such that the beam is effusive, so that the velocity distribution can be described by a Maxwell-Boltzmann distribution (Equation 2.3) which was checked experimentally just as described above for the argon beam source. The calculated values were found to agree with the experimental data within 10 m/s (Figure 2.17). Relevant quantities of the nozzle can be found in Figure 2.16 together with a drawing of the source itself. The angular distribution of the beam and the resulting density distribution in the scattering volume was calculated in the same manner as for the argon beam source. It is shown in Figure 2.15 for both molecules. The target density changes about 30% over the scattering volume.

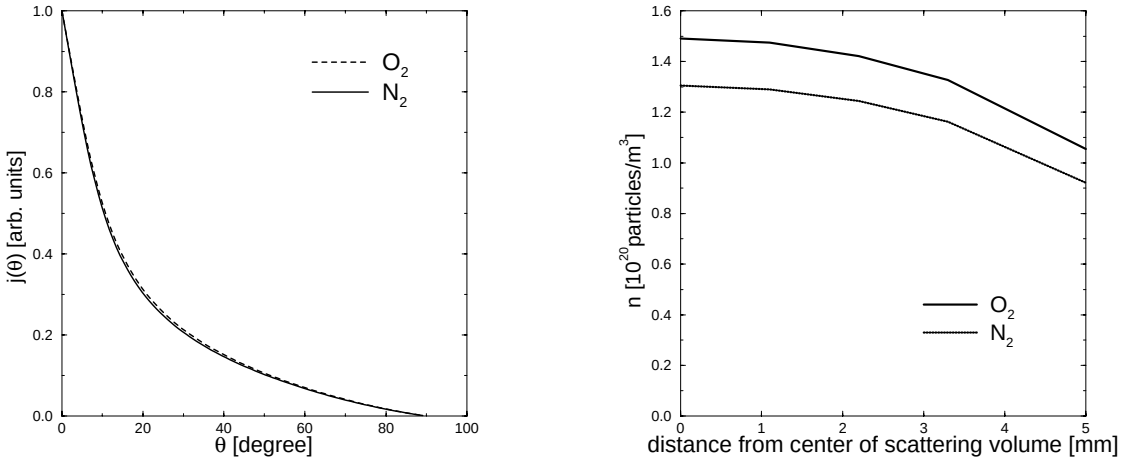
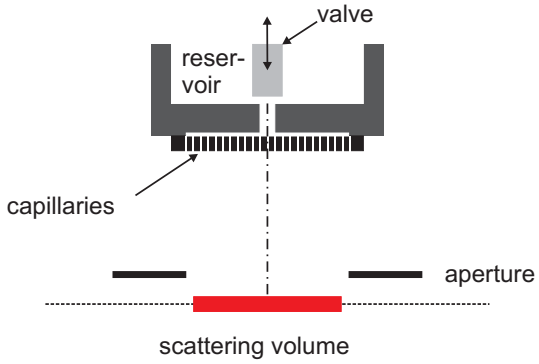


Figure 2.15: Calculated angular distribution of target atoms (left) and the resulting density over the scattering volume (right) for the molecules N_2 and O_2.



dimensions of capillaries	diameter: 10 µm, length: 1 mm
distance between capillaries	12 µm
area of array	1.2x11 mm^2
distance array – scattering volume	10.3 mm ± 0.1 mm
dimensions of aperture	1.1 mm x 11 mm
distance aperture – scattering volume	2.0 mm
pressure in reservoir	N_2: 40 mbar, O_2: 35 mbar
density in center of scattering volume	N_2: 1.3 x 10^{20} m^{-3}
	O_2: 1.5 x 10^{20} m^{-3}
temperature	290 K
mean velocity	N_2: 468 m / s, O_2: 438 m / s

Figure 2.16: Design of molecular target beam source with relevant quantities of the source.

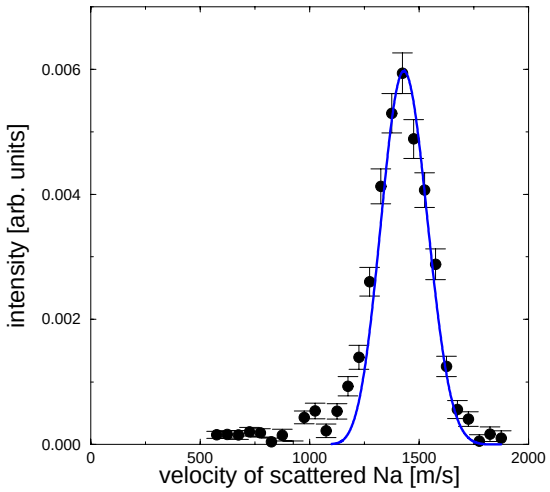


Figure 2.17: Experimental tests of N_2 velocity distribution. Comparison of calculated (line) and measured (data points with error bars) velocity of scattered Na atoms after an optical collision with N_2. Laboratory scattering angle is 18.9°, detuning is 240 cm^{-1}.

2.6 Vacuum system

The vacuum system consists of two differentially pumped vacuum chambers. Everything but the target gas nozzle is placed in the scattering chamber which is pumped by an oil diffusion pump reaching pressures around 10^{-6}-10^{-7} mbar without operating beams and 10^{-5}-10^{-6} mbar with beams in operation. The target gas nozzle is placed in a second chamber. It is pumped by a turbo molecular pump. The pressure is around 10^{-7} mbar if the nozzle is closed and rises typically to 10^{-4}-10^{-3} mbar when the nozzle opens for 300 μs with a repetition rate of 80 Hz.

2.7 Background signals and corrections

Projectile atoms are detected after an optical collision in an excited state A^* by transferring them into a Rydberg state $A(nl)$ with n typically larger than 20. If projectile atoms reach a Rydberg state by a process other than an optical collision with a target particle and a subsequent transfer to a Rydberg state by the detection laser, they can cause a signal that is denoted in the following as background signal. There are various mechanisms that lead to background signals, some of which can be suppressed while others have to be corrected for. The process of detecting a projectile atom after an optical collision is characterized by employing one particle of each of the four beams. Background signals usually require not all of the beams or more than one particle from a beam, making it possible to identify competing processes, minimize or quantitize them.

Identified sources of background signal are:

1. **Directly excited projectile atoms:** Projectile atoms can be excited directly, i.e. not during a collision but as a free atom:

$$A + h\nu \rightarrow A^*. \tag{2.8}$$

This can be caused by resonant fractions in the spectrum of the excitation laser. By suppressing the resonant fractions with the dispersion prisms (Figure 2.3), the process is completely eliminated. A direct excitation can also occur by multi-photon processes, for example hyper-Raman excitation: The projectile absorbs two photons from the excitation laser emitting one photon of another frequency to end in the detected excited state,

$$A + 2h\nu \rightarrow A^* + h\nu'. \tag{2.9}$$

If $h\nu$ or $2h\nu$ are energetically close to a transition from the ground state, this process is enhanced. This is for example the case for small detunings of the laser. As two photons from the excitation laser are needed, the ratio of the background to the entire signal can be decreased by using a lower intensity of the excitation laser. Since no collision partner is involved, the angular distribution is the one of the projectile beam.

2. **Projectile-projectile optical collisions:** An excitation of the projectile atom can take place during a collision with another projectile atom,

$$A + A + h\nu \rightarrow (AA)^* \rightarrow A^* + A. \tag{2.10}$$

A is either directly from the beam or from undirected projectile atoms from the background pressure in the copper chamber of the projectile source. The process requires two projectile atoms, so its intensity in relation to the entire signal is decreased by decreasing the projectile density. Secondly, when the temperature of the copper chamber is lowered, a decrease of this type of background is achieved since the background pressure is reduced. The angular distribution of this background is broad and is not changed considerably by the target gas.

3. **Projectile dimers:** Remaining dimers in the projectile beam can be photodissociated with at least one of the projectile atoms ending up in the excited state,

$$A_2 + h\nu \rightarrow A^* + A. \tag{2.11}$$

This process is decreased by using a higher temperature of the head of the projectile source to decrease the fraction of dimers in the beam. It has also got a broad angular distribution.

4. **Spontaneous emission:** A projectile atom that was excited either during an optical collision or by another process can decay. The emitted photon can be absorbed by another projectile atom,

$$A^* + A \rightarrow A + A + h\nu \rightarrow A + A^*. \tag{2.12}$$

The background signal was found to decrease if the detection laser pulse arrives around 2 ns before the excitation laser pulse in the scattering volume [Mae94], probably because a reasonable fraction of A^* is transferred into $A(nl)$ before decaying. Under these conditions, the contribution of spontaneous emission to the background signal can be neglected.

5. **Directly detected projectile atoms:** For small or negative detunings the energy of the excitation laser plus detection laser can be resonant to a direct transition from the ground state into a Rydberg state,

$$A + h\nu_1 + h\nu_2 \rightarrow A(nl). \tag{2.13}$$

The yield of this process is much larger than that of an optical collision and prevents measurements if present. However, the process is easily avoided by selecting a suitable detection transition $h\nu_2$ for which no two-photon transition is resonant.

6. **Detection during optical collision:** If the intensity of the detection laser is increased, the signal saturates, as can be seen in Figure 2.22. At the same time, when scanning the wavelength of the detection laser the signal does not decrease to zero between the lines. A possible explanation for this is the detection transition occuring also during the collision for which the saturation takes place at much higher intensities as for the detection of a free atom. When this is the case, a determination of the internal state of the projectile is no longer possible. By chosing the laser intensity low enough, the process is sufficiently suppressed

7. **Background signal without lasers**

In measurements with alkali-atoms as a projectile, there is a vanishing counting rate when the lasers are turned off. It turns out to be the dominating background signal when the calcium beam source is in operation. Two processes were identified that contribute to the so called “dark” signal. One process involves charged particles, probably electrons evaporating from the glowing tantalum wire. After two electrodes at 0 and around 100 V were placed as well in front of the aperture of the projectile beam and in front of the detector aperture, charged particles are deflected by the electric fields and cannot exit the copper chamber of the particle beam source or enter the detector, respectively. The “dark” signal was thus reduced drastically about a factor of 100. A different set-up was tested where the beam source as a whole was shielded by a stainless steel containment that could be set to a desired potential. This has proven to be an even more promising approach after care was taken that a layer of calcium does not electrically connect the containment to the ground potential. The remaining contribution to the “dark” signal might come

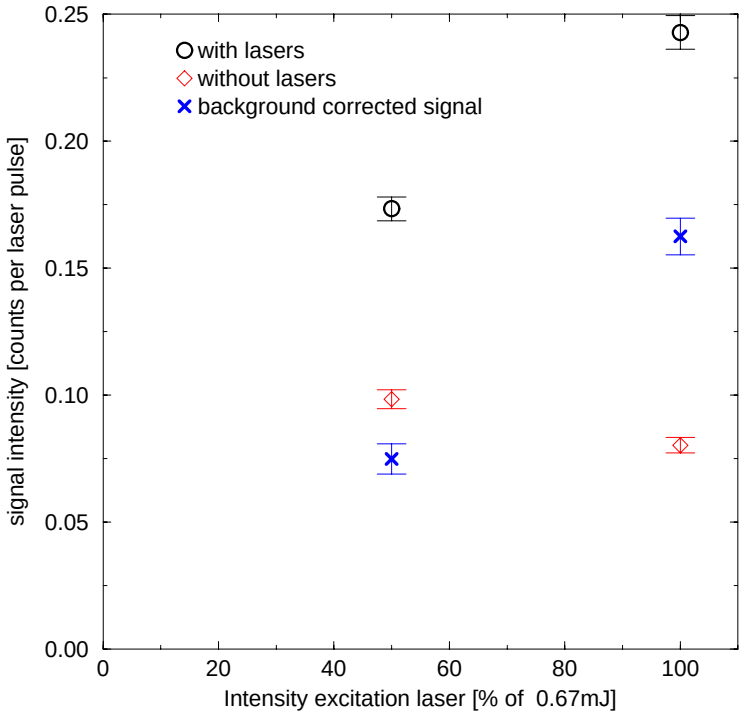


Figure 2.18: Signal of CaAr optical collision for two intensities of the excitation laser. Detuning: 300 cm^{-1}, scattering angle: 21.6°. The background signal is measured by turning off the lasers.

from metastable calcium atoms that are ionized when they hit the meshes of the detector. As a solution, a detector without meshes could be used, a suitable design for such a detector having been proposed [Mat95].

The experimental parameters are chosen such that all background signals are minimized. But in favor of realistic data taking periods, not all of it can be avoided. In measurements with calcium, the background signal 7. dominated over all the others so that as the only correction procedure the signal without lasers is measured and subtracted from the signal with lasers. The dependency of the thus quantified signal on the excitation laser was tested and found to double with double intensity (Figure 2.18) which is a strong indication that the intensity of the optical collision is quantified correctly.

In measurements with sodium and potassium, process 7. is negligible and processes 5. and 6. are avoided. There remain two types of background signal to be corrected for: Type I with a broad angular distribution which remains essentially unchanged by the target gas (2.-4.) and type II with the same narrow angular distribution as the projectile beam (1.). The background of type I is measured without the target gas as a function of the scattering angle. Due to the broad angular distribution it can be interpolated from higher angles to the forward direction of the projectile beam. The unscattered background signal of type II in forward direction is calculated by subtracting the interpolated background signal type I from a measurement in forward direction without target gas. The fraction of the projectile atoms that are scattered from the beam to higher scattering

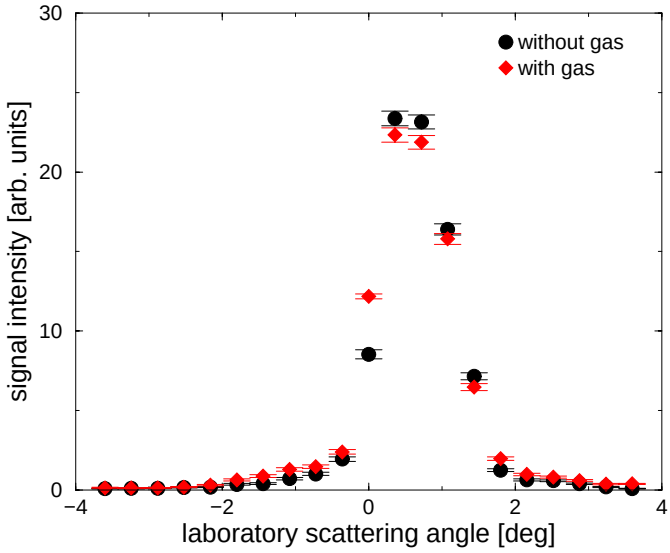


Figure 2.19: Projectile beam profile with and without target gas.

angles by the target gas is measured by directly detecting the projectile atoms with the target gas turned off in forward direction and with the gas turned on at scattering angles. The background signal of type II is scattered likewise and can thus be calculated. Due to the large detuning of the excitation laser, the background signal of type II contributes less than one percent to the entire signal in the here presented measurements. The background signal of type I, however, can be much higher. Although the stability of the experimental conditions would in principle allow a precise determination of the background signal of higher percentages than 25%, data with a background contribution of more than that are discarded to ensure that uncertainties due to imprecisions in the background quantification are negligible. The measurements shown in this work are always corrected for both types of background. The error bars of the data points correspond to one standard deviation and include usually only the statistical error.

The Rydberg atoms can not only be elastically scattered by the target gas but also stabilized. The stabilizing process relies on a change of the angular momentum of the Rydberg atom by a collision with a target-gas atom by which the probability of an optical decay of the Rydberg atom is decreased and thus the detection efficiency is higher. The background signal type I is then understimated since it is measured without gas. The amount of stabilization can only roughly be estimated. It depends on the target element and was found to be more effective for molecular targets than for atomic targets. The angular distribution of the projectile atoms is measured with and without target gas, see Figure 2.19. When the target gas is turned on, the width of the distribution is increased due to elastic scattering. If there is a not neglectable amount of stabilization, the total signal increases. In the example for KAr that is shown in Figure 2.19, the width increases by 0.1° when the gas is turned on while a significant stabilization is not observed.

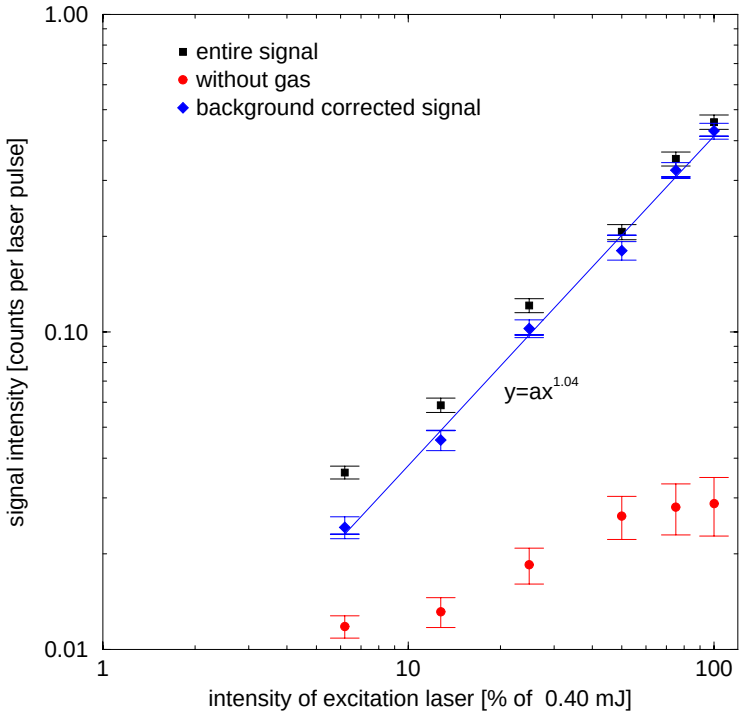


Figure 2.20: Signal dependency on intensity of excitation laser. Detuning is 480 cm^{-1}, scattering angle 21.6°.

The dependence of the signal on both laser intensities is presented for the KAr system. If the intensity of the excitation laser is varied, as shown in Figure 2.20, the background-corrected signal increases linearly. The background signal of type I shows saturation.

For low intensities of the detection laser, the signal shows an increase with the intensity that can be sufficiently approximated by a power function (Figure 2.21). For higher intensities, saturation is reached, as seen in Figure 2.22. The onset of this plateau depends on the other experimental parameters. The detection laser intensity is chosen well below the plateau to ensure a correct state selection (see 6. on page 40).

Another source for systematic errors is the fact that the intensity of the beams, especially the one of the laser beams, cannot be kept constant for longer measurements. This is accepted only if the decrease in signal is slow compared to one cycle of the measurement. To correct for this, two procedures can be employed. One data point can be measured several times during the measurement. Its intensity is used as a reference to correct the intensity of the other data points in between the reference point. Another possibility is to run the experimental cycle alternating forward and backward so that changes in the beam intensities are averaged.

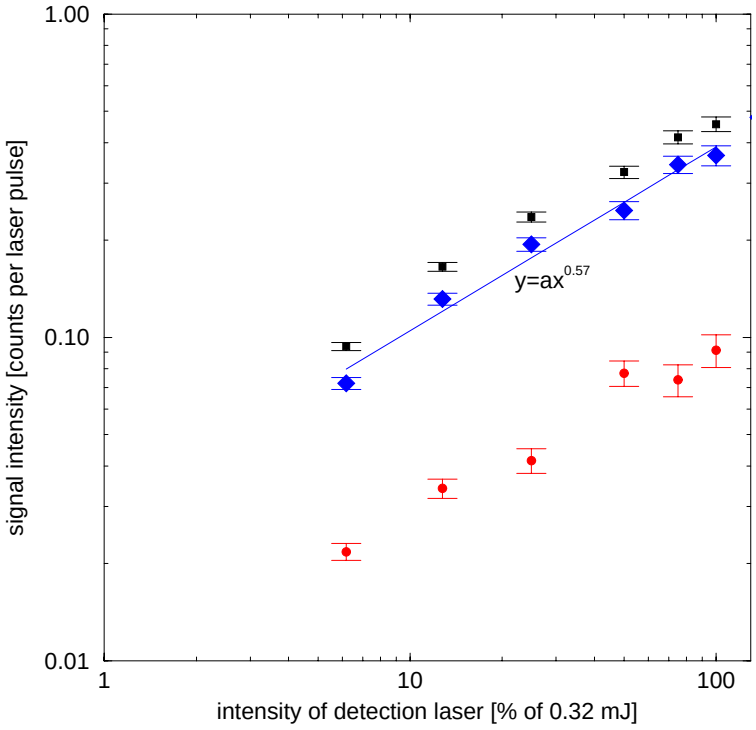


Figure 2.21: Signal dependency on detection laser intensity: Low intensities. Detuning: 640 cm^{-1}, scattering angle: 21.6°

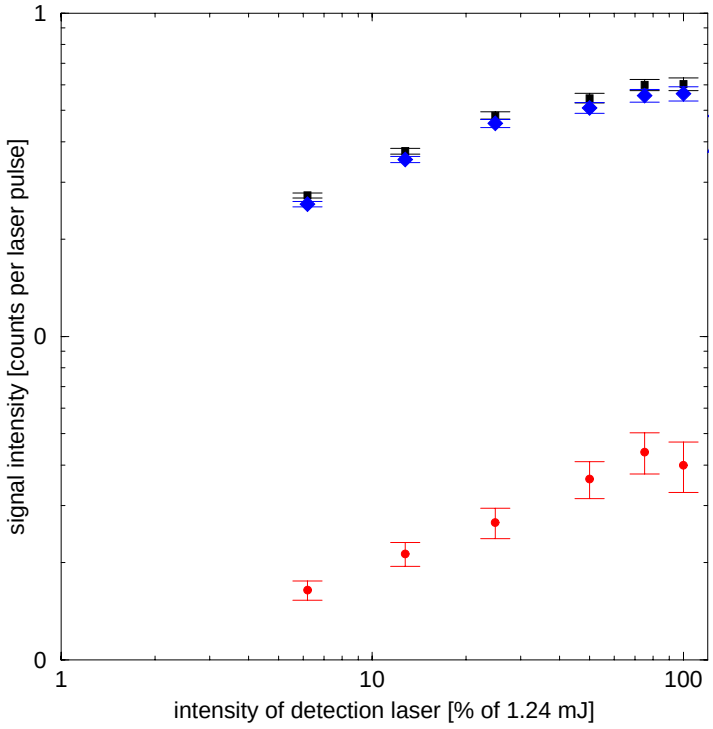


Figure 2.22: Signal dependency on detection laser intensity: High intensities. Detuning: 480 cm^{-1}, scattering angle: 21.6°

2.8 Data acquisition, automatization and electronics

The measurements are conducted automatically by a computer with a program written in LabView[11]. There are seven parameters that can be set automatically, as listed in Table 2.7 with the corresponding step width, and illustrated in Figure 2.23. The TTL pulses for the stepping motors that rotate the Fresnel rhombs and the swivel arm of the detector are given by a multi function PC-Card[12] (DaqBoard). A digital output of the DaqBoard controls the trigger for the nozzle while two analog digital converter inputs read the voltages of the photodiodes that monitor the laser intensities. The wavelength of the lasers is set by sending commands via a GPIB interface of the computer. The possibility to adress a third laser via the COM1 port of the computer was included for future experiments. The communication of the computer with the hardware is illustrated in Figure 2.23. Time insensitive communications paths are indicated by thin arrows. They are in use before taking a data point to set all parameters to the desired value.

The process of taking a data point is initiated by the excitation laser that sends trigger pulses to a trigger switch with a repetition rate that is specified by the computer. The trigger switch sends a trigger to the control unit of the nozzel. After a tunable delay in the order of milliseconds follows a trigger to the excimer laser, so that the dye laser pulses are produced. The data are taken by a multichannel analyzer PC-Card[13] (MCD-2 card). It is triggered by a pulse from the photodiode in the detection laser. The amplified pulses from the channeltron are sorted into 4096 channels corresponding to time intervals of 125 ns. The data are read out by the program from the MCD-2 card and the number of laser pulses is counted. When the desired number is reached, the excitation laser is given the command to stop sending the trigger and the counts of the MCD-2 card are

[11] National Instruments, München
[12] DaqBoard / 2000, IOtech, Cleveland
[13] MCD-2 Dual Input Multiscaler / Multichannel Analyzer, FAST ComTec GmbH, Oberhaching

Parameter	step width	controlled by means of
wavelength of excitation laser	0.3 nm	stepping motor that tilts grating in resonator of laser
wavelength of detection laser	0.3 nm	stepping motor that tilts grating in resonator of laser
orientation of polarization of excitation laser	0.225°	stepping motor that turns fresnel rhomb
orientation of polarization of detection laser	0.225°	stepping motor that turns fresnel rhomb
detected scattering angle	0.00475°	stepping motor that turns swivel arm of detector
trigger for Ar-nozzle	on / off	digital output (high / low)
wavelength of a third laser	0.0001 nm	stepping motor that tilts grating

Table 2.7: The parameters that can be varied automatically by the computer and their increments.

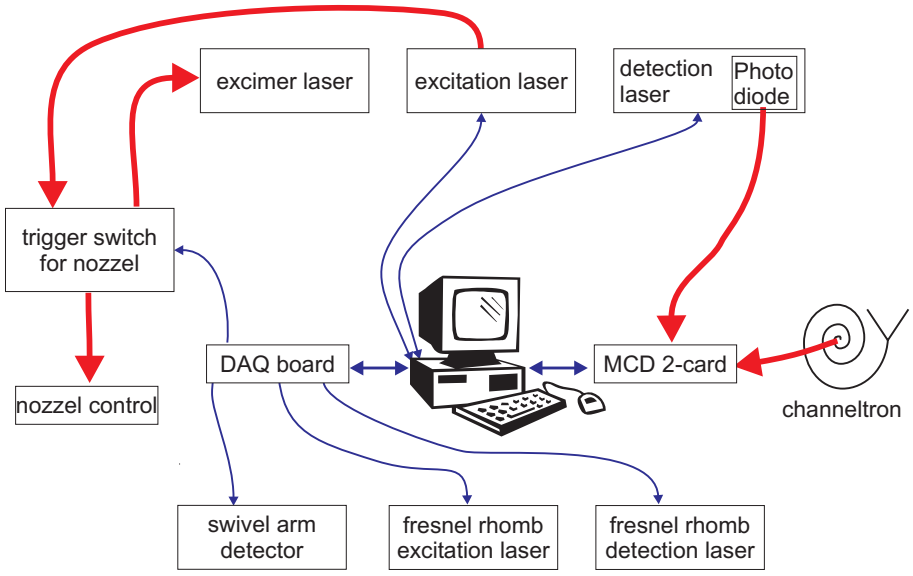


Figure 2.23: Illustration of the communication of computer with experimental hardware. Thick arrows indicate the trigger pulses that are time sensitive.

summed up for all laser pulses. The velocity that corresponds to the measured time of flight is calculated with nominal values for the distance from the scattering volume to the detector and the time of flight of the ions inside the detector (see section 2.3) and the data are sorted into velocity intervals that are usually equally spaced. The delay of the trigger switch is chosen such that the gas and the laser pulses overlap in the scattering volume. It is determined experimentally. The digital output of the DaqBoard is read by the trigger switch, and the trigger to the nozzel is only send if the output is high (i.e. the voltage is -5 V). Otherwise, the nozzel trigger is left out for a measurement without target gas. The measurements are done in cycles that are repeated automatically. The data are saved on a different computer at regular intervals for further processing.

2.9 Convolution of theoretical data

In order to compare calculated data to experimental results, the theoretical data are converted from center-of-mass coordinates to the laboratory-frame coordinates and the experimental resolutions are taken into account. The method is comparable to a convolution with an apparatus function and will hence be denoted such in the following. For the convolution, the relevant factors that influence the experimental resolution are taken into account: the velocity distribution before the collision of both the projectile and the target beam, the dimensions of the scattering volume and of the aperture of the detector and the resolution of the velocity of the scattered atoms. The nozzle of the target beam and the individual openings of the projectile beam source are assumed as point sources. The different times-of-flight of the ions inside the detector as a function of their point of origin are corrected for. Most of this section deals with the mathematical details of the transformation and convolution.

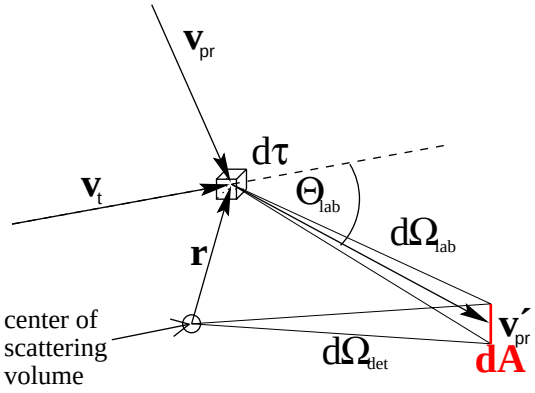


Figure 2.24: Illustration of the differential scattering rate.

We start with the differential scattering rate dI in laboratory coordinates. The optical collision of particles with velocities $\vec{v}_{\mathrm{pr}}$ and $\vec{v}_{\mathrm{t}}$ takes place in a finite volume $d\tau$ around $\vec{r}$ (as illustrated in Figure 2.24). The particles are scattered into the solid angle element $d\Omega_{\mathrm{lab}}$ around the scattering angle θ_{lab} .

$$dI(d\Omega_{\mathrm{lab}}, d\tau, \vec{E}) = |\vec{v}_{\mathrm{pr}} - \vec{v}_{\mathrm{t}}|\, n\, \frac{d\sigma_{\mathrm{lab}}}{d\Omega_{\mathrm{lab}}}\, d\Omega_{\mathrm{lab}}\, d\tau \tag{2.14}$$

with $n = n(\vec{v}_{\mathrm{pr}}, \vec{v}_{\mathrm{t}}, \vec{r}) = n_{\mathrm{pr}}(\vec{v}_{\mathrm{pr}}, \vec{r}) \cdot n_t(\vec{v}_{\mathrm{t}}, \vec{r})$ the product of the particle densities at $\vec{r}$ and $\vec{E}$ the electric field vector of the light. $\frac{d\sigma_{\mathrm{lab}}}{d\Omega_{\mathrm{lab}}} = \frac{d\sigma_{\mathrm{lab}}}{d\Omega_{\mathrm{lab}}}\left(\vec{v}_{\mathrm{pr}}, \vec{v}_{\mathrm{t}}, \vec{E}, \theta_{\mathrm{lab}}\right)$ is the differential cross section in the laboratory frame.

To obtain the total scattering rate I, Equation 2.14 is integrated over the velocities before the collision, the scattering volume and the solid angle of the detection aperture as seen from the center of the scattering volume:

$$I\left(\Omega_{\mathrm{det}}, \vec{E}\right) = \int d\vec{v}_{\mathrm{pr}} \int d\vec{v}_{\mathrm{t}} \int d\tau \int d\Omega_{\mathrm{det}} \left|\frac{d\Omega_{\mathrm{lab}}}{d\Omega_{\mathrm{det}}}\right| |\vec{v}_{\mathrm{pr}} - \vec{v}_{\mathrm{t}}|\, n\, \frac{d\sigma_{\mathrm{lab}}}{d\Omega_{\mathrm{lab}}} \tag{2.15}$$

where $\left|\frac{d\Omega_{lab}}{d\Omega_{\mathrm{det}}}\right| = \frac{\vec{v}'_{\mathrm{pr}} \cdot (\vec{v}'_{\mathrm{pr}} - \vec{r})\,|(\vec{v}'_{\mathrm{pr}} - \vec{r})|}{|\vec{v}'_{\mathrm{pr}}|^3}$ (see Figure 2.24).

All quantities on the right side of Equation 2.15 are converted to center-of-mass coordinates since the differential cross sections are calculated in the center-of-mass frame. But first, the velocity resolved detection of the scattered particles shall be discussed. For every combination $(\vec{v}_{\mathrm{pr}}, \vec{v}_{\mathrm{t}})$, the velocity v'_{pr} of the particle scattered into $d\Omega_{\mathrm{det}}$ can be calculated from the conservation of energy and momentum as described in detail in Appendix B. The velocity $\vec{v}'_{\mathrm{pr,a}}$ that is assigned to the detected particle by the data acquisition program can be slightly different, because a nominal pathway and a nominal time of flight of the ions inside the detector is assumed. $\vec{v}'_{\mathrm{pr,a}}$ is calculated by determining the time of flight that is be measured. It is the sum of the time of flight to the point of ionization in

the detector as caclulated from v'_{pr} , and the time of flight of the ions to the channeltron. Subtracting the nominal time of flight and dividing by the nominal pathway results in $\vec{v}'_{pr,a}$. In the data acquisition, the counts from particles with an assigned velocity between v_l and v_r are summed up. The sum is introduced into Equation 2.15 by a double step function $\theta_{v_l}^{v_r}(\vec{v}'_{pr,a})$ which is 1 for $v_l < \vec{v}'_{pr,a} \leq v_r$ and 0 otherwise:

$$I\left(\Omega_{det}, \vec{E}, v_l, v_r\right) = \int d\vec{v}_{pr} \int d\vec{v}_t \int d\tau \int d\Omega_{det} \left|\frac{d\Omega_{lab}}{d\Omega_{det}}\right| \theta_{v_l}^{v_r}(\vec{v}'_{pr,a}) \, |\vec{v}_{pr} - \vec{v}_t| n \frac{d\sigma_{lab}}{d\Omega_{lab}}. \tag{2.16}$$

What follows now is the transformation from the laboratory frame into the center of mass frame which is given in more detail in Appendix B. The relative velocity $\vec{v}_{rel}$ of the particles before the collision and the velocity of the center of mass $\vec{v}_{cm}$ are determined from $\vec{v}_t$ and $\vec{v}_{pr}$. The collision energy is $\varepsilon_{rel} = \frac{1}{2} m_{red} (\vec{v}_{rel})^2$ with the reduced mass $m_{red} = \frac{m_{pr} \cdot m_t}{m_{pr} + m_t}$. The scattering angle in the center-of-mass frame is given by

$$\theta_{cm} = \arccos\left(\frac{\left(\vec{v}'_{pr} - \vec{v}_{cm}\right)\vec{v}_{rel}}{\left|\vec{v}'_{pr} - \vec{v}_{cm}\right| \left|\vec{v}_{rel}\right|}\right). \tag{2.17}$$

Equation 2.16 can thus be converted into

$$I(\Omega_{det}, \vec{E}, v_l, v_r) = \int d\vec{v}_{cm} \int d\vec{v}_{rel} \int d\tau \int d\Omega_{det} \left|\frac{d\Omega_{lab}}{d\Omega_{det}}\right| \theta_{v_l}^{v_r}(\vec{v}'_{pr,a}) \, v_{rel} n_{cm} \frac{d\sigma_{cm}}{d\Omega_{cm}} \left|\frac{d\Omega_{cm}}{d\Omega_{lab}}\right|. \tag{2.18}$$

$n_{cm} = n_{cm}(\vec{v}_{cm}, \vec{v}_{rel})$ is the density of collision pairs with $\vec{v}_{cm}$ and $\vec{v}_{rel}$, $\frac{d\sigma_{cm}}{d\Omega_{cm}} = \frac{d\sigma_{cm}}{d\Omega_{cm}}\left(\varepsilon_{rel}, \alpha_{pol}, \theta_{cm}\right)$ is the differential cross section in the center of mass frame with α_{pol} the angle between $\vec{E}$ and $\vec{v}_{rel}$. The apparatus function $\left|\frac{d\Omega_{lab}}{d\Omega_{det}}\right| \theta_{v_l}^{v_r}(\vec{v}'_{pr,a}) \, v_{rel} n_{cm} \left|\frac{d\Omega_{cm}}{d\Omega_{lab}}\right|$ gives the weighing factors for $\frac{d\sigma_{cm}}{d\Omega_{cm}}$. The apparatus function containes the experimental resolution of center of mass parameters, e.g. the center of mass scattering angle and the collision energy.

Equation 2.18 is calculated by approximating the integrals by sums. Thus, the quality of the outcome depends on a suitable number of interpolation nodes for the distributions and care has to be taken not to set the grid too rough. However, computing time sets a limit to this, so that the number of interpolation nodes has to be chosen individually for each measurement.

The times-of-flight of the ions t_{ion} from the point of ionization to the channeltron were calculated as mentioned in section 2.3 by simulating the pathways of the ions starting from various ionization points. The following formula was derived by interpolation:

$$t_{ion} = \sqrt{\frac{m_{pr}}{m_{Na}}}(657.88 + 0.99z^2 + 0.01z^4 + 17.20y + 0.20yz^2 + 2.57y^2 + 0.02y^2z^2) \cdot 10^{-9} s, \tag{2.19}$$

where y is the vertical distance from the center of the aperture (in the direction in which the detector can be rotated, see Figure 2.1) and z is the horizontal distance (in the direction

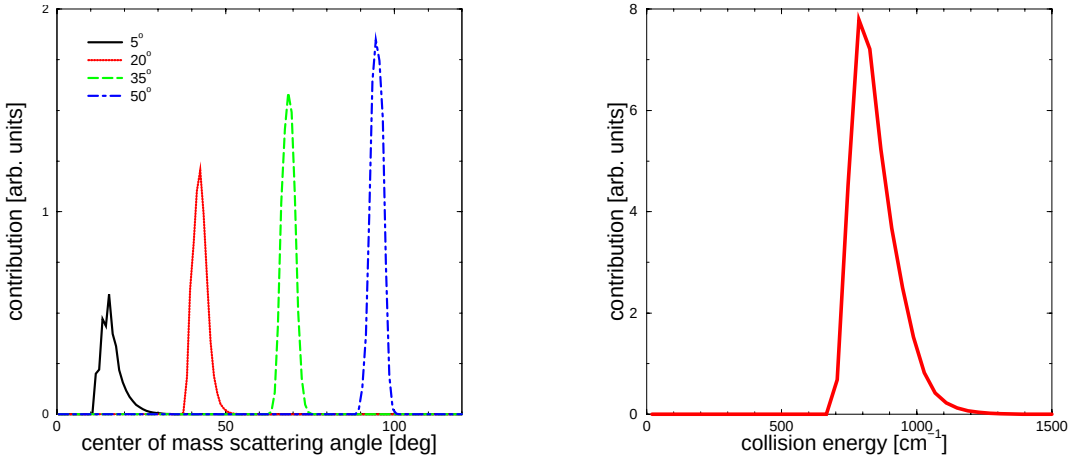


Figure 2.25: Left: Resolution of center-of-mass scattering angle. Shown are the contributions of center-of-mass scattering angles to a measured laboratory scattering angle, examplarily for a detuning of 480 cm^{-1} and a velocity of the scattered K of 1075 m/s. Laboratory scattering angle from left to right: 5°, 20°, 35°, 50°. Right: Contribution of collision energies to differential cross section for a detuning of 480 cm^{-1} and a velocity of the scattered K atoms of 1075 m/s. Sum over all scattering angles.

of the laser beams). The time of flight scales with the square root of the mass of the projectile m_{pr} and was calculated for Na.

The resolution of the center of mass scattering angles is plotted on the left side of Figure 2.25 for the KAr measurements presented in subsection 3.1.1. The center of mass angle contribution to four selected laboratory scattering angles is shown for a detuning of 480 cm^{-1} and a velocity of the scattered K atoms of 1075 m/s. The center of mass scattering angle is roughly twice the laboratory scattering angle while the full width at half maximum of the apparatus function is about 5° in the center-of-mass frame. The opening angle of the aperture of the detector is 2.6° in the laboratory frame, so the angular resolution is determined mainly by the detector aperture in this case. An additional contribution to the angular resolution is the elastic scattering by target gas. It is not accounted for in the calculation of the apparatus function, but as estimated from measurements as seen in Figure 2.9, it is only in the order of 0.1° which is usually small compared to the resolution of the detector aperture.

The corresponding contribution of collision energies to the sum over all measured scattering angles is shown on the right side of Figure 2.25. The collision energy is centered around 820 cm^{-1} with a full width at half maximum of 160 cm^{-1}.

Chapter 3

Results and discussion

3.1 KAr

3.1.1 Differential cross sections

Differential cross sections of KAr optical collisions were measured for the detunings of $220\,\mathrm{cm}^{-1}$, $480\,\mathrm{cm}^{-1}$, $640\,\mathrm{cm}^{-1}$, and $720\,\mathrm{cm}^{-1}$ and for a variety of velocities of the scattered potassium. The detected state was $K(4p_{3/2})$, background signals were subtracted as described in section 2.7. After discarding the measurements for which the fraction of the background signal exceeded 25%, 67 sets of data were kept, resulting in a total of 2274 data points. In the left column of Figure 3.1, selected results of similar collision energies for each of the detunings are shown. Differential cross sections for different velocities of the scattered potassium are presented in Figure 3.2 for a detuning of $480\,\mathrm{cm}^{-1}$. The graphs in Figure 3.2 have the same scale, and the different signal intensities reflect primarily the velocity distribution of the particle beams. The complete experimental data can be found in Appendix D. All measurements show pronounced interference patterns. The oscillation period varies between 8° and more than 40°, increasing with the detuning and decreasing with the velocity. The first maximum is a rainbow structure (see page 15). The position of the rainbow scattering angle depends on the detuning and on the velocity. While the oscillations in Figure 3.1 (a) are rather uniform, deviations from a regular interference pattern are seen for example in Figure 3.2 (c) as a broad third maximum and in Figure 3.1 (c) as a dip in the first maximum.

The interference patterns can be qualitatively understood on the basis of the corresponding deflection functions which are given next to the experimental results. It is useful to keep in mind that the center-of-mass scattering angle is roughly twice the laboratory scattering angle (see page 49) and that for all measurements presented here the scattering angle is equal to the deflection angle (refer to page 12). Note that in principle a range of deflection functions contribute to the measurements according to the resolution of the collision energy of about $160\,\mathrm{cm}^{-1}$ (see Figure 2.25). They were calculated from the quantum chemical potentials that are shown in Figure 3.3. A prominent feature is the shoulder of the $B\Sigma$ potential curve around 7 a.u. It results in a maximum in the potential difference

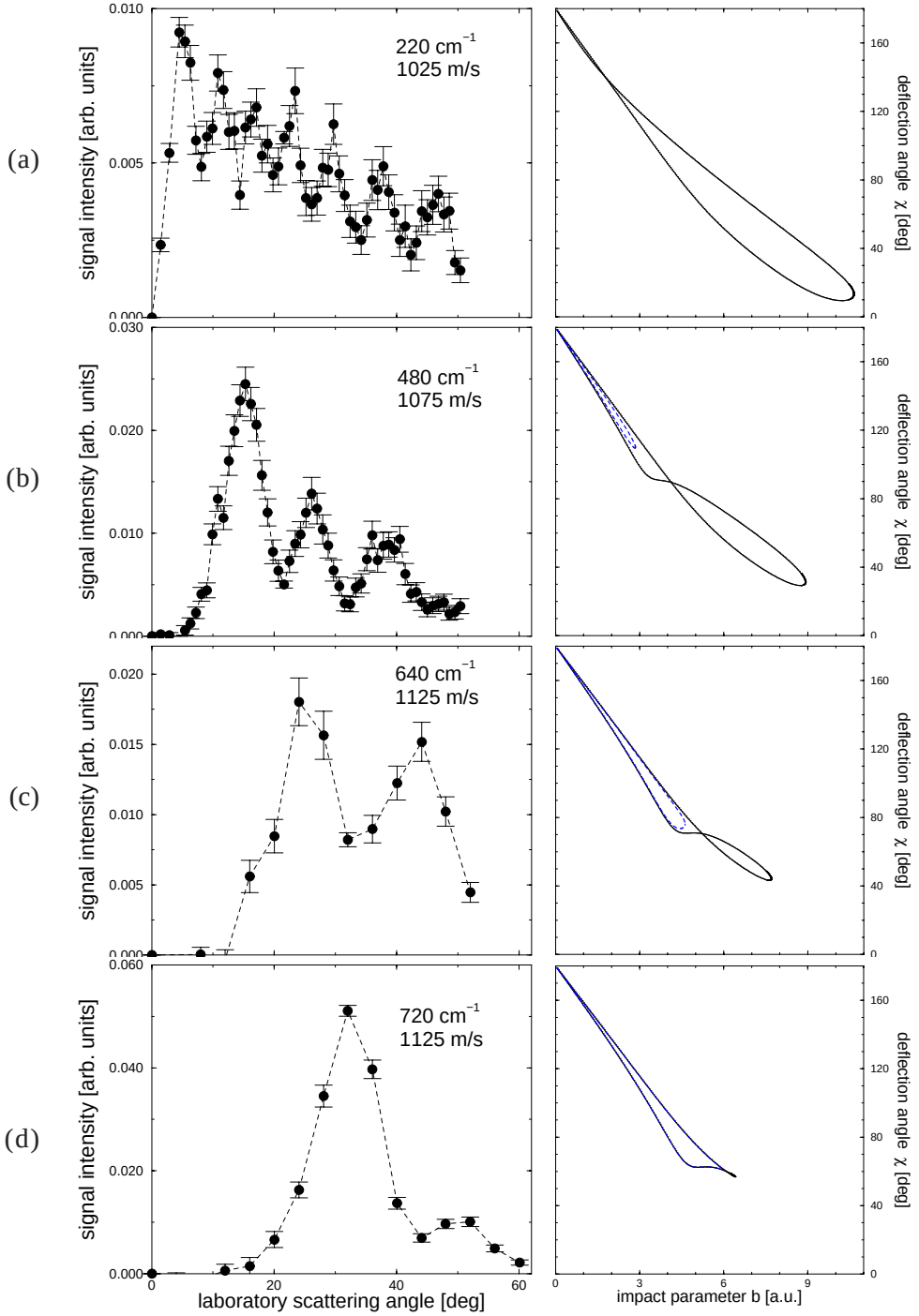


Figure 3.1: Left column: Differential cross sections for different detunings, multiplied by the sine of the laboratory scattering angle, the lines connect the data points to guide the eye. The detuning and the velocity of the scattered K atom is indicated in the graphs. Collision energies are around 800 cm^{-1}. Right column: Corresponding deflection functions for the inner (dashed) and outer (solid) Condon radii for a collision energy of 800 cm^{-1}.

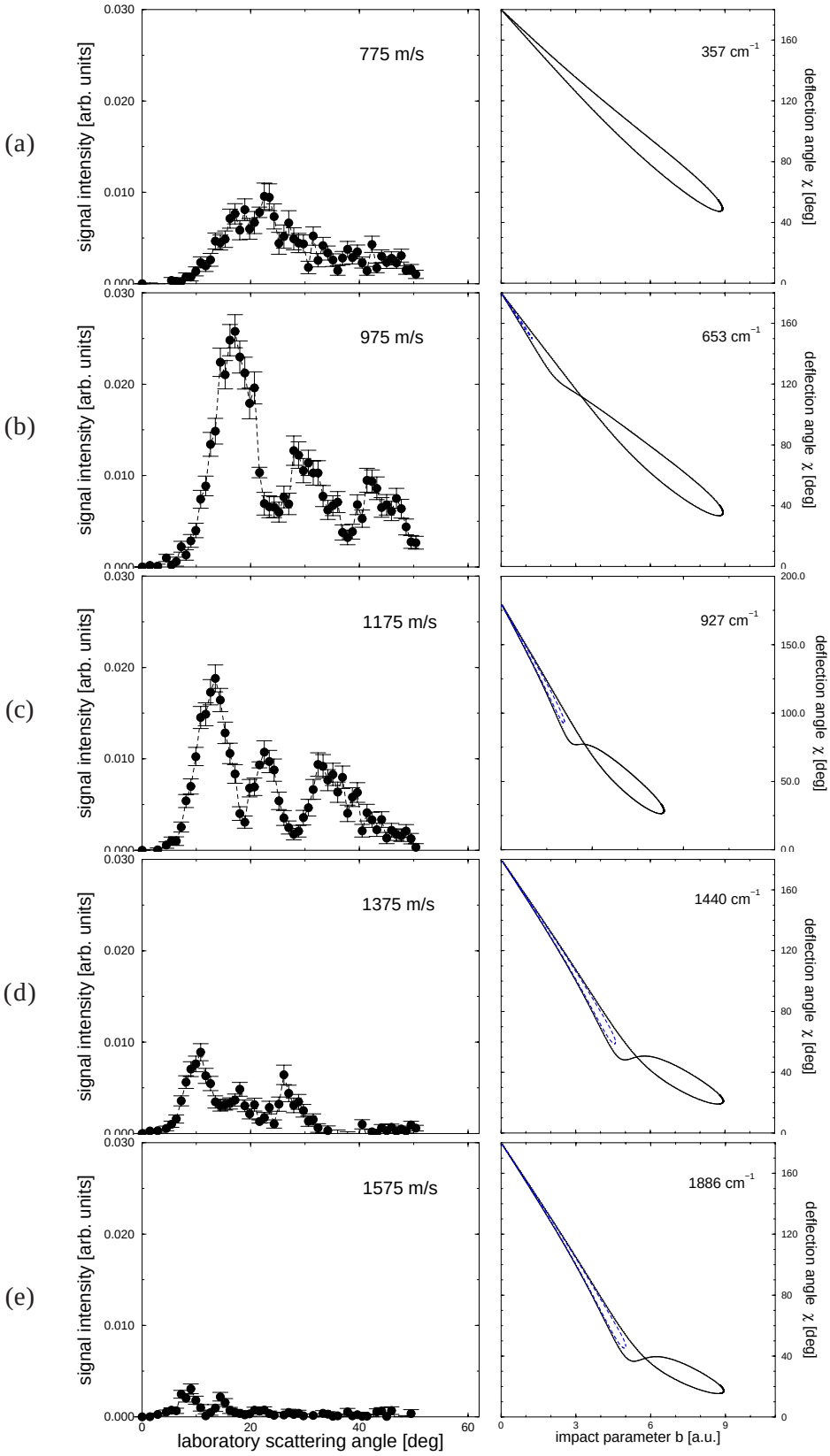


Figure 3.2: Left column: Differential cross sections for different velocities at a detuning of 480 cm^{-1}, multiplied by the sine of the laboratory scattering angle. The velocity of the scattered K atoms is given in the box, the lines connect the data points to guide the eye. Right column: Corresponding deflection functions for the inner (dashed) and outer (solid) Condon radii with the collision energy given in the box.

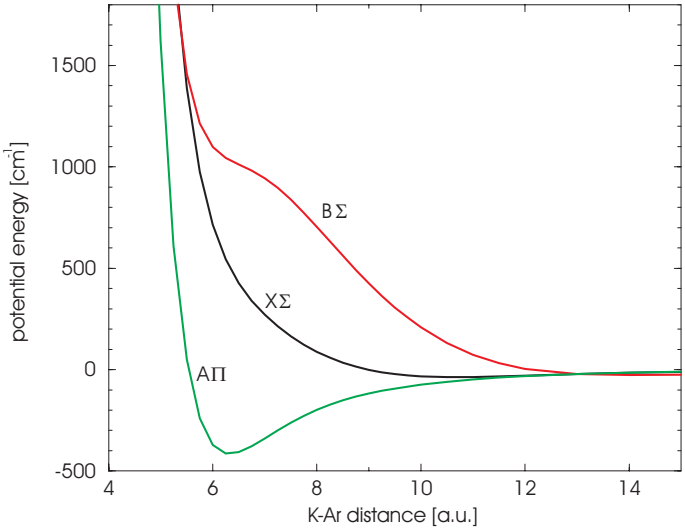
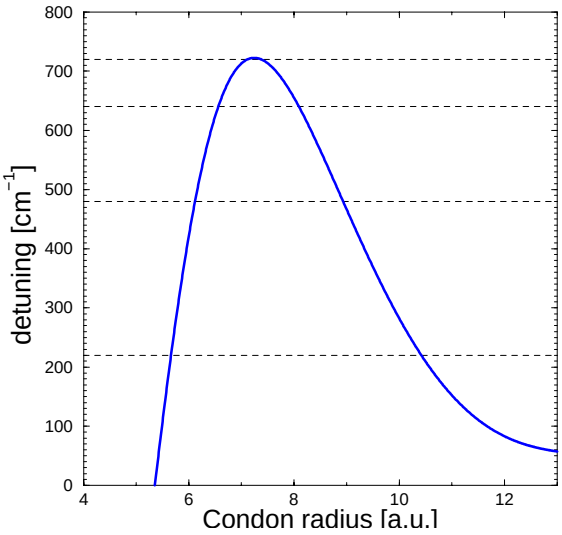


Figure 3.3: *Ab initio* calculated potentials for KAr [Czu02]. Spin-orbit interaction is not included and all curves are shifted to zero asymptotes.



detuning [cm^{-1}]	$r_{c,1}[a.u.]$	$r_{c,2}[a.u.]$
220	5.7	10.4
480	6.1	8.9
640	6.6	8.1
720	7.1	7.4

Figure 3.4: Detuning as a function of the Condon radius r_c [Czu02]. The detunings that were used are indicated by a dashed line. The corresponding Condon radii are listed on the right.

so that classically only detunings below 722 cm^{-1} are accessible. Figure 3.4 shows the detuning as a function of the Condon radius which is basically the difference of the BΣ and the XΣ curve including the spin-orbit interaction. The Condon radii for the four detunings are listed to the right of the graph. Below the maximum detuning, two Condon radii exist of which the distance increases for smaller detunings. In Figure 3.1 and Figure 3.2, the deflection function for the inner Condon radius is indicated by a dashed line while a solid line corresponds to the one of the outer Condon radius. The inner Condon radius contributes to the signal only at large scattering angles, in most cases larger than the ones measured. For the other cases, the experimental results show no effect that can be directly assigned to the inner Condon radius. Therefore, the contribution of the deflection functions of the inner Condon radius is neglected for the present qualitative discussion. The increase of the oscillation period in Figure 3.1 can be assigned to the decreasing distance of the branches of the deflection function while in Figure 3.2 it is due to a larger deBroglie wave number (refer to Equation 1.15). For all detunings, the deflection functions for the outer Condon radius cross, which is also a direct consequence of the shoulder in the BΣ potential: While for larger distances the BΣ potential is more repulsive than the XΣ, the situation reverses as the slope decreases at the shoulder of the BΣ curve. As explained in section 1.2, a crossing of the deflection functions leads to less regular structures in the interference pattern and indeed, the deviations of the measurements from regular oscillations are located around the scattering angles of the crossings.

3.1.2 Determination of XΣ and BΣ potentials

The differential cross sections of subsection 3.1.1 were used in a fitting procedure to determine the XΣ and BΣ potentials. Trial potentials were generated by systematically varying fitting parameters of model potentials. The variation is done by the software package MINUIT[1]. Since there is not only one unique system of potentials which reproduces the experimental results in this nonlinear fit, a good choice of the starting parameters (i.e. the initial potential system) and the model potentials together with the fitting parameters are essential ingredients for the quality of the outcome of the fit.

K-Ar potential curves were determined by several groups, both by experimental and by theoretical means (Figure 3.5). Zimmermann and Braune derived the attractive[2] parts of the XΣ, BΣ and AΠ state by analyzing line spectra connecting these states with accuracies ranging from $\pm 1\,cm^{-1}$ to $\pm 10\,cm^{-1}$ [Brau02]. By measuring bound-free spectra they also determined the repulsive part of the XΣ potential curve up to energies of $1000\,cm^{-1}$ with an accuracy of $\pm 10\,cm^{-1}$. For the attractive parts of the potentials, quantum chemical calculations by Jungen [Jun02] and Czuchaj and coworkers [Czu02] agree with the results from Zimmermann typically within $20\,cm^{-1}$. For the repulsive part of the XΣ state, the calculations by Jungen coincide almost perfectly with the experimental data while the results from Czuchaj underestimate the repulsion with a maximum deviation of about

[1] MINUIT, Function Minimization and Error Analyses, Release 89.12j, CERN, Geneva

[2] As attractive are denoted the parts of the potentials below the asympote. Those above are denoted as repulsive.

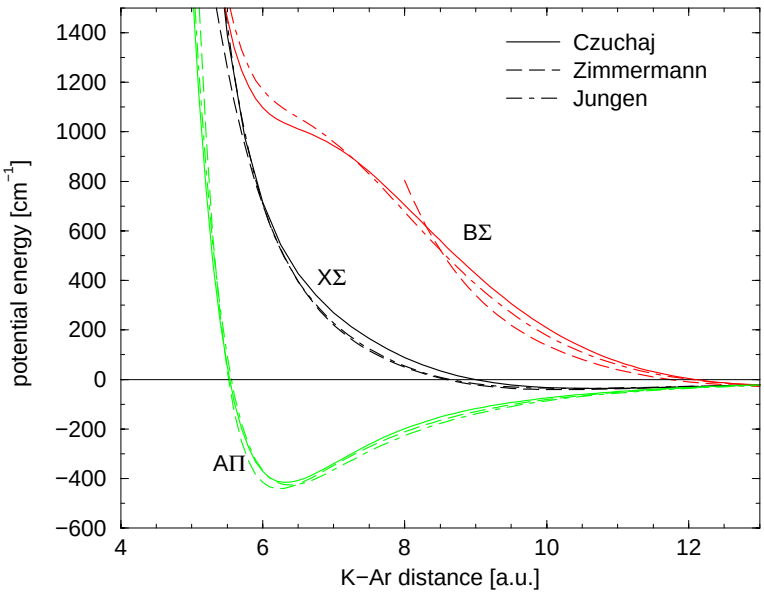


Figure 3.5: Potentials for the KAr system. Quantum chemical calculations by Czuchaj [Czu02] and Jungen [Jun02] and experimental results by Zimmermann and Braune [Brau02]

45 cm^{-1}at a K-Ar distance of 8 a.u. Furthermore, there exist older potentials by Pascale and Vandeplanque [Pas74] and Düren and coworkers [Dür82].

As the initial potential system, the data from Zimmermann and Braune were used for all but the repulsive part of the BΣ state for which the data from Czuchaj were taken for distances from 7 a.u. on inwards. The smallest internuclear distances on the BΣ state that were accessible by the measurements of Zimmermann and Braune are 12.1 a.u. From 12.1. a.u. to 7. a.u., an interpolation by two polynomial functions was made. The thus constructed BΣ curve is shown in Figure 3.6 together with the corresponding data from Czuchaj and Zimmermann and Braune. Calculated differential cross sections from the initial potential system are shown in Figure 3.7 in comparison to the experimental results for selected data sets. While the measured structures for the two large detunings are reproduced rather well, the agreement is poor for the two small ones for which the difference between the oscillation maxima is smaller in the theoretical data. Starting from the initial potential system, different model potentials were realized. Up to nine corrections at chosen sampling points were interpolated by splines and added to the initial set of potentials where the fitting parameters were the magnitude of the corrections. In another model, the position of one sampling point together with the magnitude of the correction was fitted. Alternatively, polynomials were added to the initial set of potentials with the fitting parameters being the coefficients and the position. The number of fitting parameters is currently limited to a total number of nine by computation time. The potentials were only changed for distances smaller than 12 a.u. for the BΣ potentials and smaller than 8.6 a.u. for the XΣ potential as to keep the results of Zimmermann und Braune for the attractive parts.

From every generated trial potential system, differential cross sections are obtained by quantum scattering calculations. The theoretical results are tranfsormed into laboratory

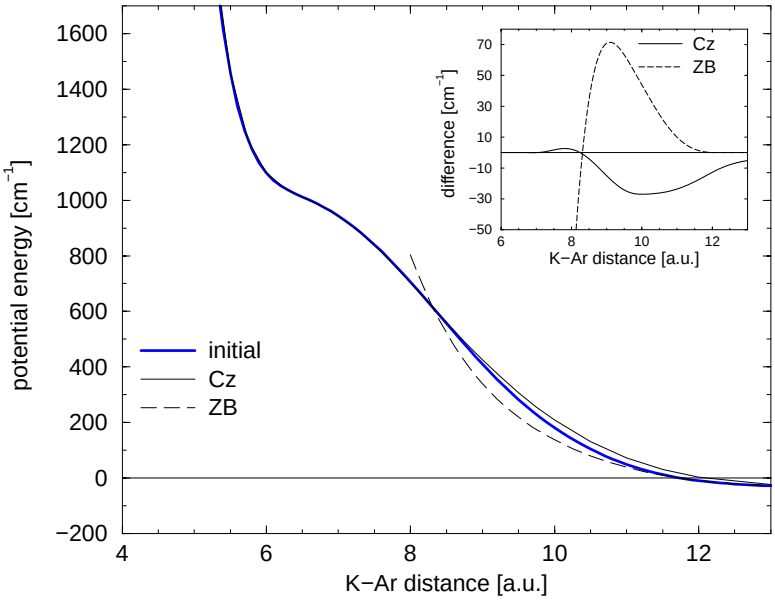


Figure 3.6: BΣ state of the initial potential system in comparison with the Czuchaj (Cz) and Zimmermann and Braune (ZB) potentials. In the inset, the difference between the initial potential and each of the two others is plotted.

coordinates and convoluted with the apparatus function as described in section 2.9. The quantity

$$\chi^2 = \sum_i p_i \frac{(y_{\mathrm{ex},i} - y_{\mathrm{th},i})^2}{\Delta y_i^2} \tag{3.1}$$

is minimized by varying the fitting parameters. $y_{\mathrm{ex},i}$ are the experimental data points with errors Δy_i and $y_{\mathrm{th},i}$ the theoretical values. p_i are weights that can be assigned to certain sets of data. Usually, they were taken 1 for the detunings of 220 cm^{-1}, and 480 cm^{-1}, and 2 for the other two detunings in order to compensate for the different number of data points in the measurements. Due to the weighting factors, a χ^2 around 2700 is expected for a perfect fit.

The best set of potentials as shown in Figure 3.8 was found by successively applying fits using different model functions and fitting parameters, and taking the result, sometimes smoothed by hand, as the starting point for the next fit. The numerical values of the potentials are listed in Appendix D. Comparing the calculations from the new potentials with the experimental results in Figure 3.9, an almost perfect agreement is found. Graphs for all experimental results are shown in the Appendix D. χ^2 is 4547 which is still a factor of 1.7 higher than the value of a perfect fit which means that the average difference between measured and calculated points is 1.3 times the experimental error margin. This indicates either an insufficient model or underestimated error bars of the experimental values. The error bars are indeed too small because they include only the statistical and not the systematic errors and hence, the value of χ^2 is not a measure for the goodness of

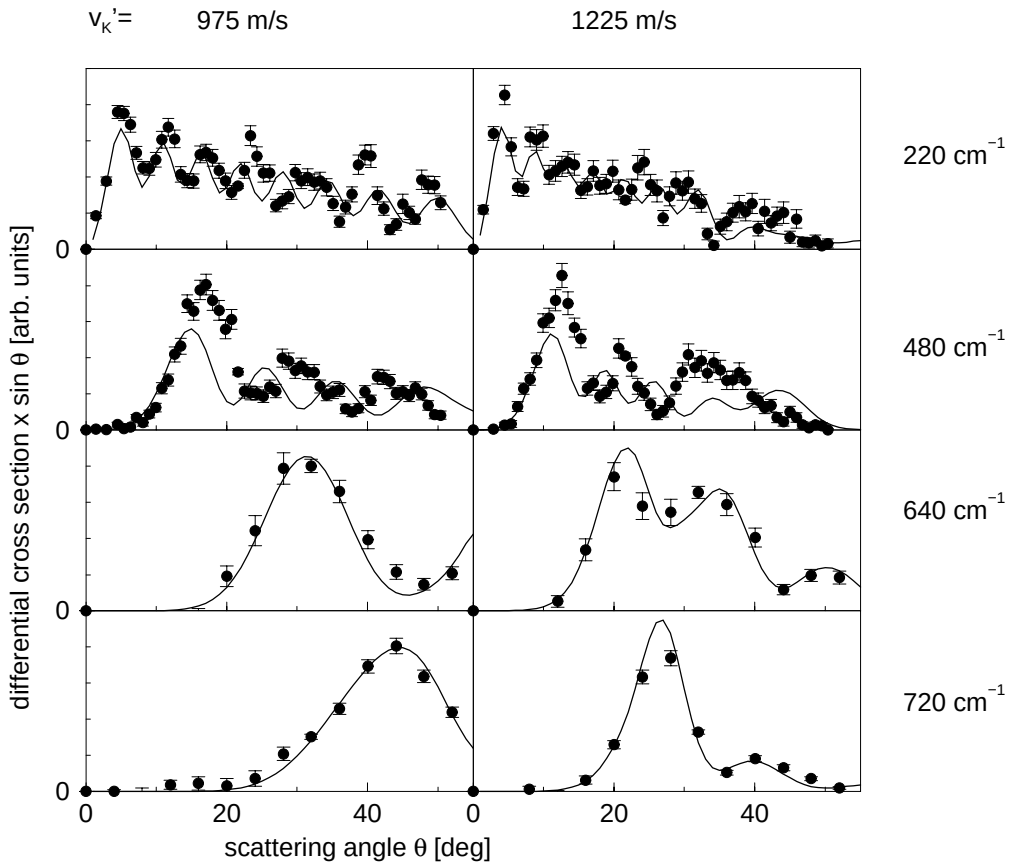


Figure 3.7: Representative experimental results in comparison with calculations from the initial set of potentials. Each column corresponds to the velocity of the scattered potassium that is given above, the detuning is given on the right of each row.

the fit. The deviation of the result of the modified fit to the fit with the realistic parameters was taken as the corresponding error of the potentials.

The statistical error is calculated by the use of constant χ^2-boundaries as confidence limits [Pre86]. Errors in the quantities that are used for the convolution of the theoretical cross sections (see chapter 2) have been considered by modifying the corresponding quantities by one standard deviation before entering them into the convolution procedure of the fit. The model potential for the error analysis was realized by 3 corrections to the X potential and 4 to the B state at fixed sampling points. Considered were inaccuracies in the determination of the velocity of the scattered potassium atom, the velocity distribution of both particle beams, the relative angle of the beams and the scattering angle, and the direction of the polarization. Additionally, a hypothetical variation of the detection efficiency with the scattering angle was assumed. Adding all contributing errors, the error margin of the potentials is found to increase from $2.0\,\mathrm{cm}^{-1}$ at 8.0 a.u. to $9.5\,\mathrm{cm}^{-1}$ at 6.0 a.u. on the X potentials and from $2.6\,\mathrm{cm}^{-1}$ at 9.5 a.u. to $13.9\,\mathrm{cm}^{-1}$ at 5.5 a.u. on the B potential. A change of the model potentials did not significantly reduce χ^2 and resulted in changes of the potentials below $1\,\mathrm{cm}^{-1}$ for interatomic distances larger than 6.0 a.u. for the X and 5.5 a.u. for the B potential. Hence, in this region the new set of po-

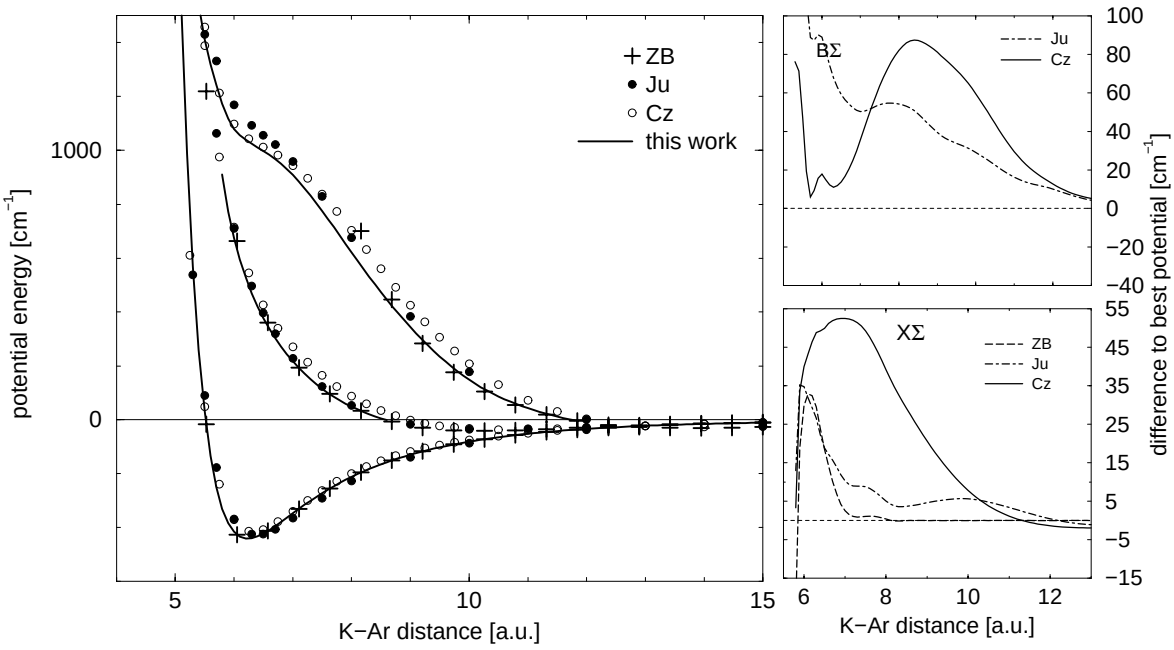


Figure 3.8: Left: Potentials as determined in this work in comparison with results from Zimmermann and Braune (ZB), Czuchaj (Cz) and Jungen (Ju). The dashed line indicates the initial potential system. Right: Differences to the new set of potentials for the XΣ and the BΣ state.

tentials is believed to be realistic. The values that are found for smaller distances depend considerably on the model potential and are therefore not given here.

In the graphs of Figure 3.8, the new potentials are compared to the previously introduced results. The calculations of Czuchaj and Jungen overestimate the repulsion of the BΣ curve with the deviation being as large as 90cm^{-1}. The same is true for the Czuchaj data of the XΣ state for which the difference is only in the order of 50 cm^{-1}. The X-state data of Jungen are found to agree with the present result within less than 10 cm^{-1} with an exception around 6 a.u. where the difference increases to 30 cm^{-1}. The deviation from the experimental Zimmermann and Braune data are as small as 3 cm^{-1} for values larger than 7 a.u., while for smaller distances the difference increases to 30 cm^{-1}. Considering the increasing error margin, this is still a reasonable agreement. When calculating the Condon radii with the new potentials they are shifted by up to 0.3 a.u. inwards with respect to the results from Czuchaj while the maximum accessible detuning of 730 cm^{-1} is almost the same compared to 722 cm^{-1} for the Czuchaj potentials. It is notable that in contrast to previous determinations of potentials with differential cross sections of optical collisions, both potential curves can be determined [Gro97a, Gro00]. The achieved accuracy is common for a potential determination based on the analysis of line spectra. However, it was not achieved so far on the basis of scattering data. A confirmation by an independent approach is therefore highly desirable.

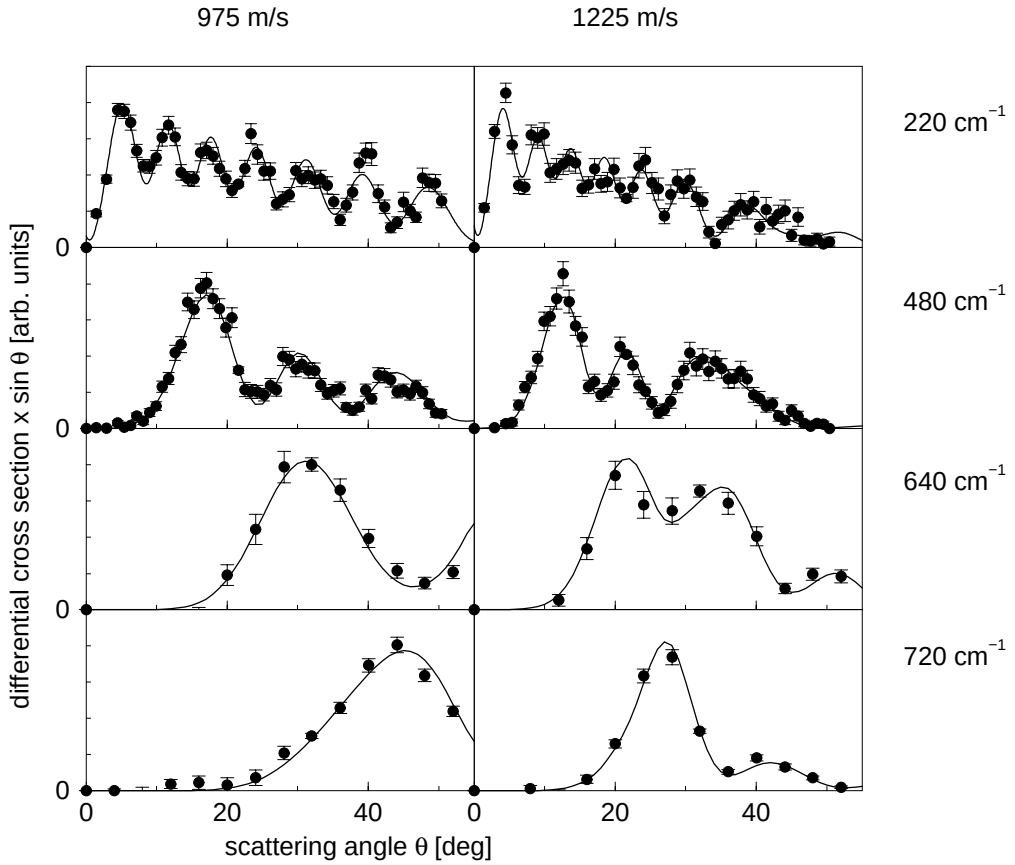
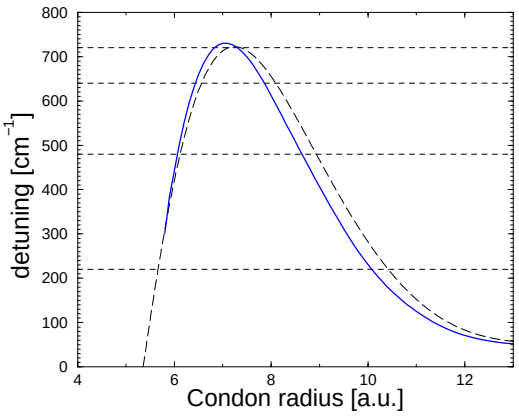


Figure 3.9: Representative experimental results in comparison with calculations from the new potential. Each column corresponds to the velocity of the scattered potassium that is given above, the detuning is given at the right of each row.



detuning [cm^{-1}]	$r_{c,1}[a.u.]$	$r_{c,2}[a.u.]$
220	not known	10.1
480	6.1	8.6
640	6.4	7.9
720	6.8	7.3

Figure 3.10: Detuning as a function of the Condon radius r_c for the best potentials (thick line) and for the Czuchaj results (dashed line). The detunings that were used for the experiments are indicated by a dashed line. The corresponding Condon radii for the new potentials are listed on the right.

3.1.3 Nonadiabatic transitions

With a positive detuning of the excitation laser, the $B\Sigma_{1/2}$ state is excited during the collision. In the output channel of the collision, nonadiabatic transitions from $B\Sigma_{1/2}$ to $K(4p_{1/2})$ can occur. The relative population of the fine-structure states is measured by scanning the detection lasers over lines that correspond to transitions from each of the fine-structure levels into the same Rydberg states as illustrated in Figure 3.11. The integrated signal is proportional to the population of the corresponding fine-structure level. Relative populations were determined for detunings of 480 cm^{-1} at a scattering angle of 18° and for 640 cm^{-1} at 24° and 36°. The results are shown in Figure 3.12, presented as a function of the kinetic energy after the collision. To keep the experimental procedure simple, the yield of the two levels is compared not for the same relative kinetic energy but for the same velocity of the scattered potassium atoms. The same velocities, however, correspond to slightly different relative kinetic energies as illustrated in Figure 3.13. For a velocity of 1225 m/s, the difference is 30 cm^{-1} while the resolution is 120 cm^{-1}. The energy that is precisely assigned to a data point corresponds to the kinetic energy of a $K(4p_{1/2})$ atom after the collison. The relative population decreases for low relative kinetic energies and reaches the characteristic value of 1/3 for higher energies for all measurements.

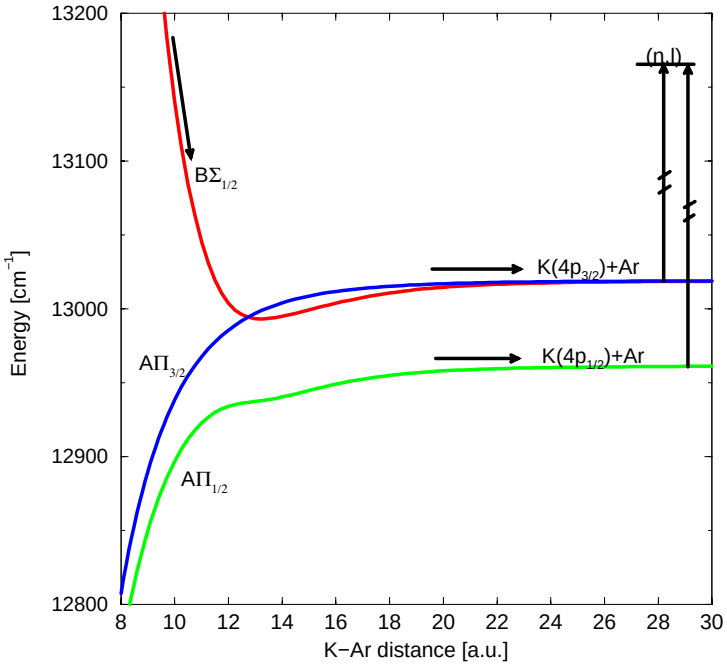


Figure 3.11: Principle of nonadiabatic transition transition measurement.

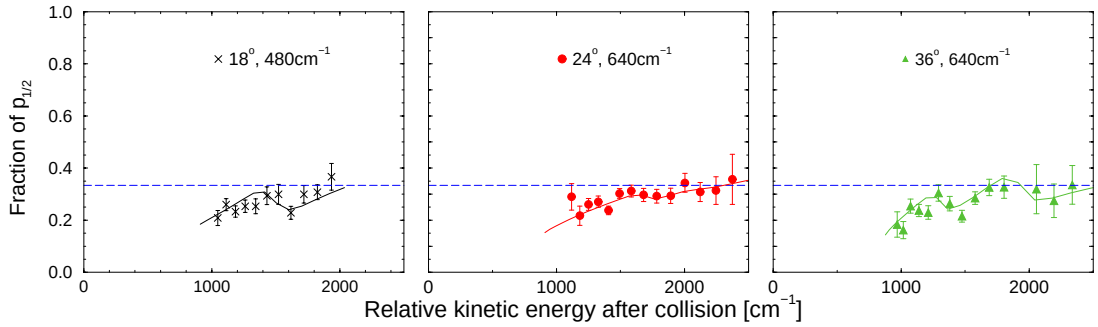


Figure 3.12: Symbols: Measured relative population of the K($4p_{1/2}$) state as a function of the relative kinetic energy for a detected K($4p_{1/2}$) atom. The laboratory scattering angle and the detuning is given in the graphs. Line: Quantum scattering calculations with potentials from this work.

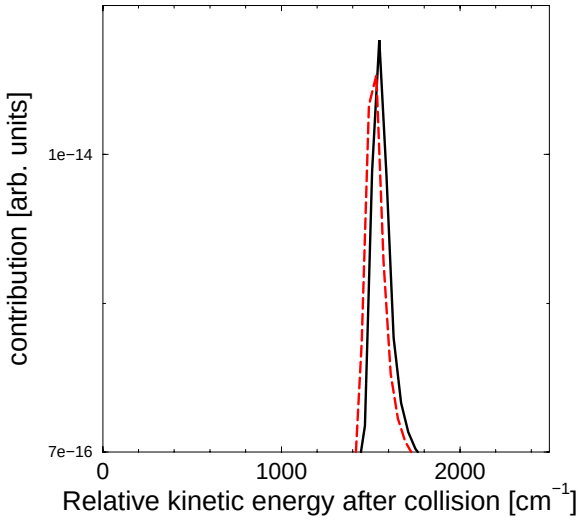


Figure 3.13: Comparison of contribution of kinetic energies after collision for a measured velocity of 1225 m / s. solid line: detected state is K($4p_{1/2}$), dashed line: detected state is K($4p_{3/2}$).

For a correct determination of the relative population it is essential to probe the two fine-structure states with the same sensitivity. Since the detection transitions are chosen such that the same Rydberg state is excited, the optical transition probabilities and the lifetime of the Rydberg atoms is the same. The measurements are done with the polarization of the detection laser changed alternatingly about 90° in order to exclude errors due to polarization effects. The efficiency of the laser dye depends on the wavelength, so that the laser intensity is different for each of the detected states. As a correction, the dependency of the signal on the detection laser intensity is determined with a measurement comparable to the one shown in Figure 2.21. During the actual experiment, the laser intensity is monitored by the photodiodes for both detection transitions and the signal is corrected for the different intensities. The only remaining considerable systematic error is a possible incorrect treatment of the background so that 50% of the subtracted background

signal was included into the error bars of the signal. The contribution is small, however, compared to the statistical uncertainties of the data, the systematic error lies in the order of 3% of the measured relative population.

The relative population was calculated from the new potentials of subsection 3.1.2. The agreement between theory and experiment is very good, see Figure 3.12. As the transition probability is governed mainly by the outer parts of the potentials, this confirms the results of Zimmermann and coworkers. For collisions of Na with Ar and Kr, it was found that the influence of an avoided crossing of the $A\Pi_{1/2}$ and the $B\Sigma_{1/2}$ curve leads to a population of up to 80% of the $Na(3p_{1/2})$ state for low energies [Gro99b]. The reason is a diabatic passage of the crossing which is located at smaller interatomic distances followed by an adiabatic passage of the outer coupling region. Although such a crossing is present also in the KAr potential curves at a distance of about 13 a.u., the relative population does not exceed 1/3. The coupling at the avoided crossing is given by the spin-orbit interaction. It is about a factor 3 higher for K than for Na, and supports thus an adiabatic passage of the crossing. The oscillations in the measurements at scattering angles of 18° and 36° are caused by the interferences that are also seen in the differential cross sections and are determined by the inner part of the potentials.

3.2 NaN_2, NaO_2: Nonadiabatic transitions

The fine-structure branching ratio in the output channel of Na-molecule collisions was measured for the molecules N_2 and O_2. The results are shown in Figure 3.14, for a detuning of 240 cm^{-1} and laboratory scattering angles of 18.9° for NaN_2 and 19.9° for NaO_2. The only difference of the experimental method to the one described for the KAr measurements in subsection 3.1.3 is the use of the molecular target beam source. In contrast to previous experiments with molecular targets, the velocity distribution and the rotational temperature of the molecular beam was thus well defined (see section 2.5). Although the velocity distribution of the molecular target beam is thermal, the resolution of the collision energy is comparable to the energy resolution in the KAr measurements: It is 10%, whereas it was about 8% for KAr. For both targets, the relative population of the $Na(3p_{1/2})$ state lies around 1/3 and shows no significant dependence on the collision energy. For NaO_2, it can be speculated that the values rise above 1/3 for energies around 800 cm^{-1}. However, the error bars are too large for a definite statement.

Calculated values for NaN_2 are shown as a line in Figure 3.14. Because of the weak dependence of the relative population on the collision energy in the observed energy interval, the theoretical data were not convoluted with the apparatus function. The mean values of the experimental and theoretical data agree within less than 5% which is within the error margin of the experimental data. It shall be noted that all possible systematic errors were corrected or included into the error bars (see subsection 3.1.3). Thus, the theory is found to be in very good agreement with the measurements. A comparison of the O_2 measurements to calculated values would be highly desirable but cannot be

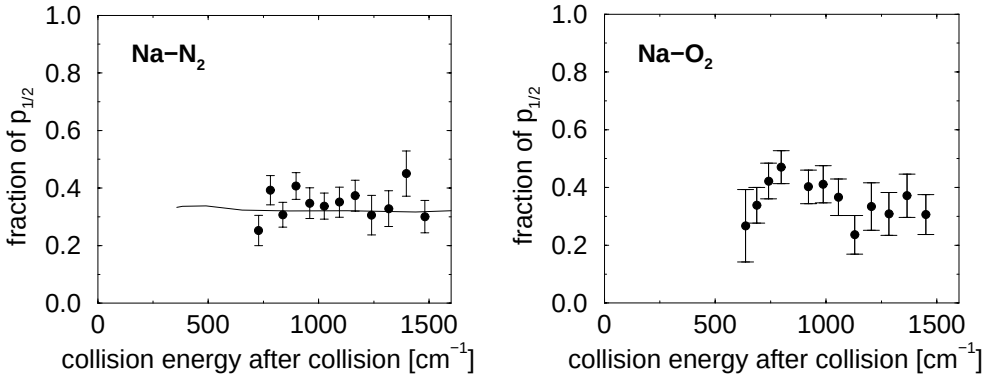


Figure 3.14: Relative population of the $Na(3p_{1(2)})$ fine-structure state as a function of the relative kinetic energy after the collision of the $Na(3p_{1/2})$ collision product. Left: NaN_2 in comparison with calculation. Right: NaO_2.

presented to date since no energy surfaces of NaO_2 are available. An interpretation of the results is not as straightforward as in the case of atom-atom collisions. Apart from the interatomic distance, the potential energy depends also on the relative orientation of the molecule with respect to the Na-molecule axis so that not only potential curves but potential surfaces have to be considered and calculations have to average over a large number of different trajectories. The calculations for NaN_2 show that the relative population of the fine-structure levels shows a significant dependence on the actual trajectory of the system in the potential surface. The value of 1/3 that is observed in the experiments can therefore not be assigned to a diabatic passage of the system through the outer coupling region of the potential surfaces as it was in the atom-atom case. It is rather an average over different values from many trajectories. Surprisingly, the calculations predict a dependence of the relative population on the rotational temperature of the target beam [Reb03]. For a lower rotational temperature, the values would rise above 1/3. It would therefore be interesting to repeat the measurements with a supersonic N_2 beam for which the rotational temperature would be lower. A supersonic beam could be produced using a seeded beam technique in which, however, the comparably high density of the carrier gas presents a problem. A distinction of collisions with a target molecule from collisions with a carrier gas atom could be possible if the carrier gas is much lighter than the target molecule. Then, larger scattering angles can only be reached by collisions with the heavier molecule.

3.3 CaAr: Optical collisions near a forbidden atomic transition

The spectral line shape in the far wing of a collisionally broadened allowed atomic transition is primarily governed by the shift of the atomic resonances in the presence of a perturber [All82]. In the case of a weak or forbidden atomic transition, the interaction with a collider can result in an enhancement of the line [Say80]. We performed experiments near the dipole forbidden $Ca(4s^2)^1S \rightarrow Ca(4s4d)^1D$ atomic line for which the transition dipole moments show a strong dependence on the CaAr distance.

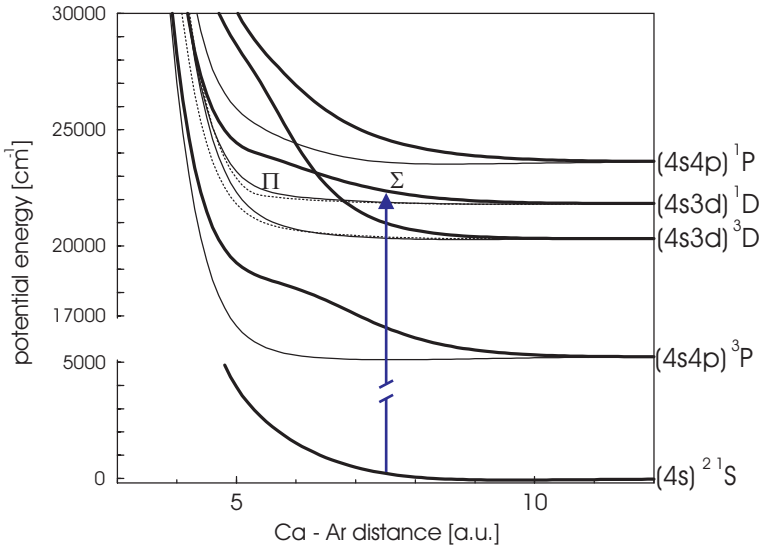
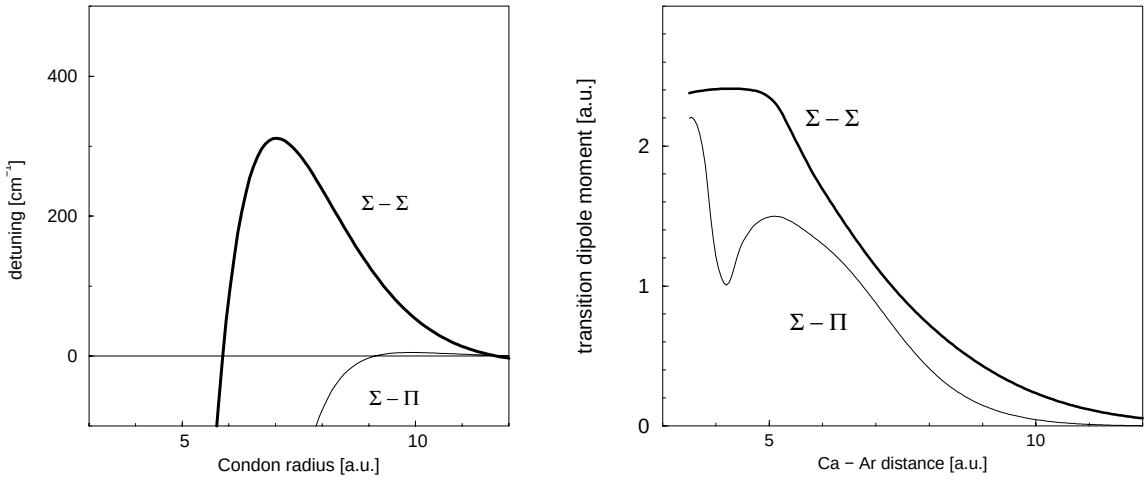


Figure 3.15: Potential curves of CaAr [Czu03]. The arrow indicates the transition used in the here presented experiments.

In gas cell experiments with rare gas perturbers, a blue satellite band was detected near the $Ca(4s^2)^1S \rightarrow Ca(4s4d)^1D$ atomic line [Cou88, Gon94]. Other experiments with calcium and rare gases studied the influence of collisions on another dipole forbidden transition [Kle86], an intercombination line [Cra93] and a transition that is allowed in the atomic case [Sat95]. Various bound states of the CaAr molecule were the subject of spectroscopic measurements [Leu99, Kau97b, Kau97a, Leu97]. The experiments initiated calculations of the electronic structure [Czu89, Czu91, Spi02, Kir00] and of collisional effects [Dev86, Dev97, Cou87, Bic00].

Recent quantum chemical potentials [Czu03] of the ground state and the first four sets of states corresponding to a single excitation of Ca are shown in Figure 3.15. For the experiments, a positive detuning from the $Ca(4s^2)^1S \rightarrow Ca(4s4d)^1D$ resonance was used, the corresponding potential difference is shown in Figure 3.16(a). For detunings larger than $10\,cm^{-1}$, only the Σ curve is reached for which the difference, similar as in the case of KAr, goes through a maximum leading to two possible Condon radii. However, with the present collision energies, the inner Condon radius is only accessible for detunings close to the maximum of $310\,cm^{-1}$. The corresponding transition dipole moments (Figure 3.16(b)) decrease to zero for large Ca-Ar distances illustrating the dipole forbidden atomic transition. For small interatomic distances, they reach values of a strong optical transition.

Measured differential cross sections for a detuning of $303\,cm^{-1}$ are shown in Figure 3.17 for four different velocities of the scattered Ca. Due to the use of a high argon pressure, the collision energy has an estimated uncertainty of about $100\,cm^{-1}$ (see section 2.5). The signal intensity shows a slow variation with the scattering angle, so that only the first maximum is observed. For higher velocities, a shoulder can be seen before the minimum is reached.



(a) (b)

Figure 3.16: (a) Condon radius of the $\Sigma - \Sigma$ transition indicated by the arrow in Figure 3.15 as a function of the CaAr distance. The Condon radius of the $\Sigma - \Pi$ transition is plotted to show that it is not accessible with positive detuning. (b) Corresponding transition dipole moments as a function of the interatomic distance [Czu03]

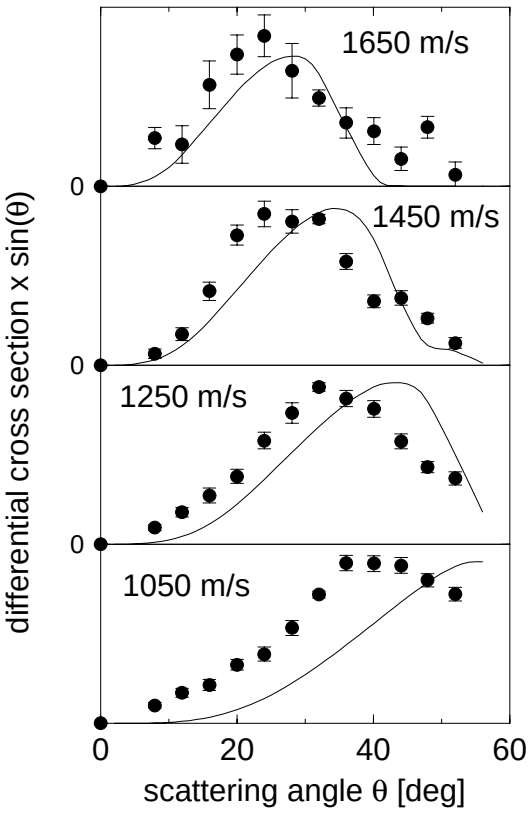


Figure 3.17: Differential cross sections. Detuning is $303\,\mathrm{cm}^{-1}$. The velocity of the scattered Ca is indicated in each graph. The lines are theoretical results.

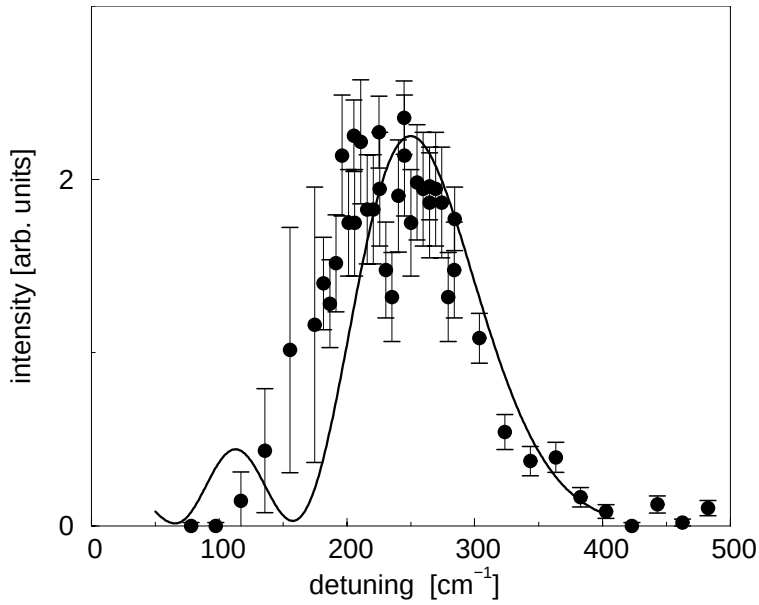


Figure 3.18: Signal dependence on the detuning. Registered were Ca^1D atoms with a velocity of 1050 m / s to 1150 m / s, laboratory scattering angle was 28.8°. Circles: Experimental results. Line: Theoretical values.

The detuning of 303 cm^{-1} is close to the maximum in the potential difference curve. Hence, the situation is comparable to the KAr measurements for a detuning of 720 cm^{-1} and the structures of the differential cross sections are similar. However, the separation of the two branches of the deflection functions is smaller leading to a slower change of the phase difference with the scattering angle and thus to a comparably slow variation of the signal intensity. The line in Figure 3.17 shows the theoretical results. The calculations are based on the potentials in Figure 3.15 and include the ground state and the Σ and Π excited state. The agreement is good for higher velocities. For example, the shoulder at high scattering angles for a velocity after the collision of 1450 m / s is seen both in theory and experiment, even though shifted by about 10°. The uncertainty in the collision energy might be the reason for the remaining disagreement.

Fixing the laboratory scattering angle at 28.8°, the yield of Ca^1D collision products was measured as a function of the detuning of the excitation laser in the velocity interval from 1050 m / s to 1150 m / s, see Figure 3.18. Increasing the detuning, the signal goes from zero through a maximum at 235 cm^{-1} and vanishes for large detunings.

For detunings above 310 cm^{-1}, resonant transitions are not possible due to the maximum in the potential difference curve. The peak is a rainbow structure from the maximum in the difference potential. This is why it occurs below the maximum potential difference of 310 cm^{-1}. When the detuning goes toward zero, the Condon radius is shifted towards larger values where the transition dipole moments become small. A comparison with the calculations (the line in Figure 3.18) shows a very good agreement, the position of the peak is reproduced within 15 cm^{-1}. However, the second peak around 100 cm^{-1} in the theoretical data is not confirmed by the experimental results. It is tempting to assign the peak to interference effects from the two Condon radii, but at detunings around 100 cm^{-1}

the inner one does not contribute to the signal. The second peak is rather an interference structure from two trajectories for the outer Condon radius. Thus, the abscence of the small peak in the experimental results reflects the disagreement of experiment and theory in the differential cross sections. The position of the peak confirms the results of Gondal and coworkers who detected a maximum at 230 cm^{-1} [Gon94].

It is desirable to reproduce the measurements under conditions for which the velocity of the argon beam is well defined. For this, the calcium beam source has still to be improved in order to suppress the described “dark” signal. The containment around the source seems to be a promising approach, a detector without meshes could be an alternative solution.

The study of a two-electron system opens the possibility for the observation of spin-changing collisions. With a negative detuning, the Π state converging to the atomic ^{1}D state would be excited. At the avoided crossing with the Σ curve converging to the ^{3}D state, transitions can occur which could be studied by detecting the ^{3}D collision products. Comparable experiments were performed in gas cells in which the system was prepared in the ^{1}P state and the yield of the three fine-structure levels of the ^{3}D was probed [Spi02]. Spin-changing collisions were also studied for higher lying states [Kha96]. However, none of the experiments provided an energy resolved analysis that is possible in a differential optical collisions experiment. Another interesting capability of the method comes from the fact that the detuning determines if the excitation takes place inside or outside the avoided crossing. If the excitation takes place outside of the avoided crossing, only atoms that are excited during the incoming part of the collision can make a transition to the ^{3}D state. For the transition occuring in the outgoing part of the collision, the crossing is not passed. In a differential optical collisions experiment, the molecular axis at the moment of transition and with it the direction of the transition dipole moment is fixed in space. Thus, by turning the polarization perpendicular to the corresponding transition dipole moment, one of the two trajectories could be selectively suppressed and the final state of the collision could be manipulated by the polarization.

Bose-Einstein condensation in a microtrap

Chapter 4

Theoretical description

4.1 BEC phase-transition

For a trapped gas of noninteracting bosons, the mean occupation number N_i of each single particle state of energy ε_i is given by the Bose-Einstein distribution

$$N_i = \frac{1}{e^{(\varepsilon_i - \mu)/k_B T} - 1} \tag{4.1}$$

with μ the chemical potential, k_B the Boltzmann constant and T the temperature of the gas where the total number of particles is $N = \int n(\varepsilon) d\varepsilon$. The BEC phase-transition is characterized by the start of a massive population of the ground state ε_0 of the trapping potential. It occurs at a temperature for which the matter waves of the particles start to overlap [Ket99]. For an ideal gas of particle density n this is the case when the interparticle separation $1/n^3$, is comparable to the thermal deBroglie wavelength $\lambda_T = h/\sqrt{2\pi m k_B T}$ with m the mass of the particle. The critical temperature T_C of the phase transition for many particles in a large box potential is reached when the phase-space density $n\lambda \mathrm{T}^3 = 2.612$ [Cor99]. A further decrease in temperature results in a rapidly increasing population of the ground state given by

$$\frac{N_0}{N} = 1 - \left(\frac{T}{T_C}\right)^3. \tag{4.2}$$

For a harmonic trap with the frequencies ω_x, ω_y, and ω_z, the critical temperature is given by

$$k_B T_C \approx \bar{h}\bar{\omega} \left(\frac{N}{1.202}\right)^{1/3} \tag{4.3}$$

with $\bar{\omega} = (\omega_x \omega_y \omega_z)^{1/3}$ the geometric average of the trap frequencies.

Although Equation 4.3 does not take into account the interactions between the particles and applies only for a very large total number of particles, the critical temperature calculated from Equation 4.3 has proven to be close to the experimentally observed values [Ens96]. Typical experimental parameters result in a critical temperature between nK and μK so that in order to initiate a Bose-Einstein condensation, efficient cooling techniques have to be applied.

4.2 Collisions at low energies

Collisions at low energies can be described by only one parameter, the scattering length a, as opposed to thermal collisions for which the details of the interatomic potentials have to be known. In a quantum-mechanical treatment of cold collisions, the wavefunction can be expanded in the basis of spherical harmonics, which are eigenfunction to the angular momentum operator, so-called partial waves. In the limit of small energies and densities, only the partial wave with angular momentum $l = 0$ contributes to the differential cross section . For larger l the centrifugal barrier dominates over the potential energy. This is why the scattering process is referred to as s-wave scattering. An s-wave scattering process is independent of the scattering angle, comparable to the scattering from a solid sphere. In good approximation, the exact interatomic potential can be replaced by the pseudo potential

$$V(\mathbf{r}) = \frac{4\pi\hbar^2}{m} a\delta(\mathbf{r}) \left(\frac{\partial}{\partial r} r\right) \tag{4.4}$$

where $\mathbf{r}$ is the relative position vector of the two particles [Cast01]. The sign of a determines whether the interaction of the particles is attractive or repulsive. With the pseudopotential, the total cross section σ is calculated to be [Ket96]

$$\sigma = \frac{8\pi a^2}{1 + k^2 a^2}. \tag{4.5}$$

Although a depends very sensitively on the underlying potentials, two collision systems with the same scattering length have got the same collision properties when they are cooled down. The theoretical determination of a is difficult because a small error in the interatomic potentials can result in severe errors in the scattering length. Thus, a is commonly determined experimentally.

4.3 Wavefunction and density distribution

For a mean distance of the particles larger than the scattering length and a large number of particles, the interaction energy is independent of the exact coordinates of the other

particles (mean field approximation), and the wavefunction ψ of the ground-state particles can be described by a product state of N_0 single-particle wavefunctions. ψ fulfills the time-independent nonlinear Gross-Pitajevskii equation

$$\left(-\frac{\hbar}{2m}\nabla^2 + V_{\text{ext}}(\mathbf{r}) + \frac{4\pi\hbar^2 a}{m}|\psi(\mathbf{r})|^2\right)\psi(\mathbf{r}) = \mu\psi(\mathbf{r}) \tag{4.6}$$

which is derived from the Schrödinger equation by including the interaction between the particles by the pseudo-potential given by Equation 4.4. $V_{\text{ext}}(\mathbf{r})$ is the external trapping potential. The time evolution of ψ is given by $\psi(\mathbf{r},\mathbf{t}) = \mathbf{e}^{-\mathbf{i}\mu\mathbf{t}/\hbar}\psi(\mathbf{r})$.

$|\psi|^2$ is the density distribution of the condensate. In the Thomas Fermi regime, where the interaction energy of the atoms dominates over the kinetic energy, the first term in Equation 4.6 is negligible and the density distribution $n(\mathbf{r})$ is easily seen to be

$$n(\mathbf{r}) = \frac{m}{4\pi\hbar^2 a}[\mu - V_{\text{ext}}(\mathbf{r})]. \tag{4.7}$$

The density distribution reflects directly the inverted shape of the trapping potential. In comparison, the density distribution of a thermal cloud n_{th} at temperatures $T \gg T_{\text{C}}$ is given by the classical Boltzmann-distribution [Dal99]:

$$n_{\text{th}}(\mathbf{r}) \propto e^{-\frac{V_{\text{ext}}(\mathbf{r})}{k_{\text{B}}T}}. \tag{4.8}$$

4.4 Magnetic trapping

A trap is essential to hold the atoms in place when cooling and later on studying them. Traps can be realized by magnetic fields or far-off resonant laser beams. In the present work, a magnetic trap is used. Magnetic traps rely on the Zeeman shift ΔE that is introduced into the energy levels of an atom in the presence of a magnetic field $\mathbf{B}$. It is given by

$$\Delta E(B, m_{\text{F}}) = g_{\text{F}}\mu_B m_{\text{F}} B \tag{4.9}$$

where g_F is the Landé g-factor, μ_B is the Bohr magneton and m_{F} is the projection of the angular momentum F onto the axis given by $\mathbf{B}$. Depending on the sign of $g_{\text{F}}m_{\text{F}}$, the potential energy of the atom is at minimum either at the minimum or the maximum of the magnetic field. Since Maxwell's equation do not allow a maximum of a magnetic field in free space [Ket92], in a magnetic trap only so-called low-field seekers can be trapped.

To guarantee that the spin follows the direction of the field so that m_F is constant, adiabacity has to be maintained implying that the change in the direction θ of the magnetic field must be slow compared to the Larmor frequency ω_{L}:

$$\frac{d\theta}{dt} \ll \omega_{\mathrm{L}} \propto |B|. \tag{4.10}$$

Adiabacity cannot be maintained around a zero minimum of the magnetic field so that atoms near the center of the trap are lost through spin flips. To avoid the so-called Majorana spin flips, a trap with a nonzero minimum can be used.

4.5 Laser cooling

Magnetic traps for neutral atoms have depths of the order of mK which is too shallow to hold atoms of room-temperature energy. The customary technique to load a magnetic trap is to pre-cool atoms with optical and magneto-optical techniques in which the cooling is established by the interaction of atoms with a light field.

The Doppler cooling relies on the radiation pressure on the atoms created by the light of a laser beam that is detuned to the red of the atomic resonance by $\delta = \omega_{\mathrm{L}} - \omega_{\mathrm{A}}$ (ω_{L}: frequency of light, ω_{A}: frequency of atomic transition). Atoms that move in the opposite direction of the beam are more likely to absorb photons than atoms that move in the same direction of the beam since the Doppler shift moves the frequency of the light closer to the atomic resonance. The photonic recoil as experienced by the absorbing atom has always the direction of the corresponding laser beam whereas the following spontaneous emission is isotropic. An average over many cycles of absorption and spontaneous emission results in a directed net momentum-transfer to the atom. The temporal derivative is the radiation pressure

$$\mathbf{F}_{\mathrm{rp}} = \hbar\mathbf{k}\,\frac{\Gamma}{2}\,\frac{s_0}{1+s_0+(\frac{2(\delta-\mathbf{kv})}{\Gamma})^2} \tag{4.11}$$

which is the effective force acting on the atoms. $\frac{1}{\Gamma} = \tau$ is the lifetime of the excited state, $\hbar\mathbf{k}$ is the momentum of the photon, $\mathbf{v}$ the velocity of the atom and $s_0 = \frac{2\Omega^2}{\Gamma^2}$ the resonant saturation parameter with Ω the Rabi frequency. If there are two counterpropagating beams of the same frequency, intensity and polarization, the net force onto the atoms is the friction-like force

$$\mathbf{F} = -\alpha_{\mathrm{D}}\mathbf{v} \tag{4.12}$$

for small velocities ($kv \ll \Gamma$) and laser intensities ($s_0 \ll 1$) with

$$\alpha_{\mathrm{D}} = -8\hbar k^2 \frac{s_0\frac{\delta}{\Gamma}}{(1+(\frac{2\delta}{\Gamma})^2)^2} \tag{4.13}$$

being at maximum for a detuning of $\delta_{max} = -\frac{\Gamma}{2\sqrt{3}}$. The force is opposed to the velocity of the atoms which leads to cooling. The atoms continuosly gain and lose the momentum of the photons and a steady state will be reached that can be compared to the Brownian motion of a particle. The so-called Doppler limit is the minimum temperature T_D that can be reached by Doppler cooling with a detuning of half the natural linewidth of the transition:

$$T_D = \frac{\hbar\Gamma}{2k_B} \tag{4.14}$$

which is 143 µK in the case of ^{87}Rb. As experimentally observed in 1988 [Let88], there is another velocity dependent force present which was later named the Sisyphus effect: Two coherent counterpropagating laser beams of orthogonal circular polarization create a light field with a position-dependent polarization. For an atom with a suitable hyperfine structure, this results in a position-dependent light-shift of the corresponding sublevels. Optical pumping occurs from the energetically higher Zeeman sublevel to the energetically lower one. This leads to a situation in which an atom climbs a potential energy hill more often than it goes down, the rise in potential energy being compensated by the atom's kinetic energy. This process eventually cools down the atom to temperatures given by the maximum light shift $U_0 = \frac{\hbar\Omega^2}{4\delta}$ for large detunings with Ω the Rabi frequency, so Sisyphus cooling could lead to arbitrarily low temperatures in theory. Nevertheless, the temperature T_{rec} of the recoil limit, corresponding to the recoil energy of the atom after absorbing a photon,

$$T_{rec} = \frac{\hbar^2 k^2}{2mk_B} \tag{4.15}$$

sets a limit to Sisyphus cooling. $\hbar k$ is the momentum of the photon. T_{rec} is 180 nK for ^{87}Rb, and experimentally achievable temperatures lie in the order of a few T_{rec} [Coh98].

4.6 Magneto-optical trap

The radiation pressure of the light can additionally be made position sensitive by applying a spatially dependent magnetic field **B** as suggested by Dalibard in 1986 [Coh98]. It requires a trapping transition that includes at least one state with a nonzero total angular momentum F. The principle will be shown for a one-dimensional configuration in which the magnetic field is $\mathbf{B} = Bz\mathbf{e_z}$. For simplicity, an atomic F=0→F'=1 transition is considered. Two red-shifted lasers of opposite circular polarization counterpropagate in the z-direction as shown in Figure 4.1. Thus, the absorption of a photon from the laser counterpropagating to the displacement of the atom is more probable than of the other one because the transition that is selected by the polarization of the lasers is shifted into resonance by the Zeeman shift (Figure 4.1). The momentum transfer results in a restoring force toward the point of zero magnetic field.

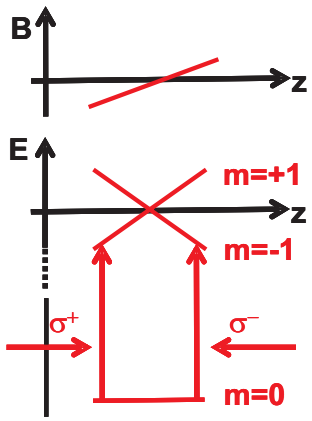


Figure 4.1: Principle of a magneto-optical trap. A linear magnetic field results in a position dependent splitting of the magnetic sublevels. Red detuned laser beams of circular polarization yield a force toward the zero of the magnetic field.

The combination of Doppler and Zeeman effect results in a net force onto the atom which is both velocity and position dependent, and the equation of motion of an atom is the same as the one of a damped harmonic oscillator. The scheme can be extended to three dimensions by using a quadrupole magnetic field and six laser beams from each direction, and a so called magneto-optical trap (MOT) was first realized in 1987 [Raa87].

4.7 Evaporative cooling

For a decrease in temperature below the recoil limit, the technique of evaporative cooling can be employed. Evaporation is commonly known as the conversion of the liquid to the gaseous state. In a more general sense, it can be defined as the situation in which energetic particles, as present in the tail of a Maxwell-Boltzmann distribution, leave a system with a finite binding energy. A mere removing of particles above a certain energy limit from the energy distribution does not increase phase space density and the temperature remains unchanged. For cooling, the remaining particles in the trap have to rethermalize by elastic collisions. When the timescale of rethermalization is larger than the timescale of evaporation, the system can be considered to be in a quasi-thermal equilibrium with the energy distribution given by a truncated Maxwell-Boltzmann distribution of corresponding temperature. Despite the drawback of decreasing the number of particles, evaporative cooling has become the key technique to cool a trapped atom-cloud below the critical temperature. A good overview about the concepts of evaporative cooling can be found in [Ket96].

Experimentally, evaporative cooling of spinpolarized atoms which are held in a magnetic trap with the potential $U_t(\mathbf{r})$ is realized by inducing a transition to an untrapped spin state with the potential $U_u(\mathbf{r})$ by an rf-magnetic field of frequency ω_{rf} (Figure 4.2). The trapped and the untrapped spin states are coupled where $U_t(\mathbf{r}) - U_u(\mathbf{r}) = \hbar\omega_{rf}$. The trap is thus effectively reduced to a height $\Delta U_{eff} = \hbar(\omega_{rf} - \omega_0)$ where $\omega_0 = U_t(0) - U_u(0)$. Atoms

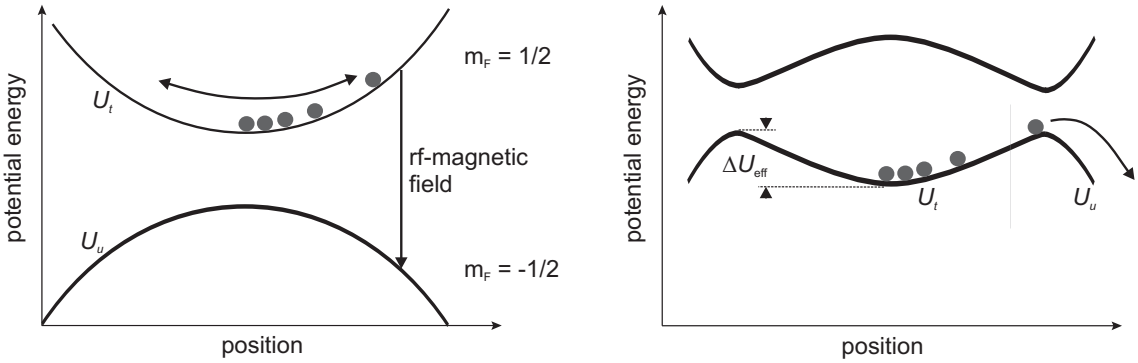


Figure 4.2: Principle of forced evaporative cooling. The figure on the left shows a trapped and an untrapped spin state with potential energies U_t and U_u. A coupling introduced in the right figure by an rf-magnetic field leads to transitions from the trapped to the untrapped state effectively reducing the trap depth to U_{eff}.

of energy $E > U_{eff}$ are lost from the trap. In reality, there are usually more than one trapped and untrapped state, but the scheme can be readily expanded to that situation. $\Delta U_{eff} = \eta k_B T$ is usually given in dependence of the temperature of the trapped particles by the truncation parameter $\eta > 1$. The efficiency α of evaporative cooling is given by

$$\alpha = \frac{d \ln T}{d \ln N} = \frac{\eta + \kappa}{\delta + \frac{3}{2}} - 1 \tag{4.16}$$

with κ of the order of one and δ given by the shape of the potential $U \propto r^{d/\delta}$ of dimension d [Coh96]. α characterizes how much more than the average energy is taken from the system by evaporating one atom. The higher the efficiency the less atoms are necessary to be lost for a certain decrease in temperature. In principle, α can be set to arbitrarily high values by increasing η, but in reality it is limited by the finite lifetime of the atoms as is described in the following.

The timescale τ_{evap} of the cooling process, given by the evaporation rate $1/\tau_{evap}$ at which particles are produced by elastic collisions with an energy larger than $\eta k_B T$, increases with α. To estimate τ_{evap}, an untruncated Maxwell-Boltzmann distribution is considered. For η much larger than 1, almost every collision involving a particle of energy larger than $\eta k_B T$ will remove the particle from the high-energy tail. In equilibrium, this rate is the same as the rate at which high-energy particles are produced. The rate $\dot{N}$ of evaporated particles can thus be expressed by

$$\dot{N} = -\frac{1}{\tau_{evap}} N \quad \text{with} \quad \frac{1}{\tau_{evap}} = n_0 \sigma \bar{v} \eta e^{-\eta}. \tag{4.17}$$

n_0 is the peak density, σ the total elastic cross section and $\bar{v}$ the average velocity. If U_{eff} is kept constant (simple evaporative cooling), η increases with decreasing temperature and the rate of collisions leading to evaporation decreases (Equation 4.17) slowing down the

cooling process. To avoid this, η is usually kept approximately constant (forced evaporative cooling).

The time constant τ_{el} for rethermalization is given by the rate of elastic collisions:

$$\frac{1}{\tau_{\mathrm{el}}} = n_0 \sigma \sqrt{2} \bar{v}. \tag{4.18}$$

The ratio $\lambda = \tau_{\mathrm{evap}}/\tau_{\mathrm{el}}$ is given by

$$\lambda = \sqrt{2}\frac{e^{\eta}}{\eta}. \tag{4.19}$$

η should be chosen such that λ is large compared to 1 to ensure rethermalization during the cooling process.

In the dynamical process of evaporation, n_0 and $\bar{v}$ vary in time due to the loss of particles and the decrease in temperature. Furthermore, there are losses from the trap due to collisions with the background gas, inelastic collisions or three-body collisions in the trap. The resulting trapping time Γ is determined experimentally by measuring the number of atoms in the trap as a function of time. For constant η, the time evolution of the evaporation rate is given by [Ket96]

$$\frac{d}{dt}\ln(1/\tau_{\mathrm{evap}}) = \frac{1}{\tau_{\mathrm{el}}}\left(\frac{\alpha(\delta-\frac{1}{2})-1}{\lambda} - \frac{1}{R}\right), \tag{4.20}$$

where $R = \Gamma/\tau_{\mathrm{el}}$ is the number of elastic collisions per trapping time. An increasing collision rate (run-away evaporation) is achieved when

$$R > \frac{\lambda}{\alpha(\delta-\frac{1}{2})-1} = \sqrt{2}e^{\eta}\frac{1}{\eta(\frac{\eta-2}{3})-1} \tag{4.21}$$

which sets an upper limit to η. Since η determines the efficiency, R should be as large as possible. R can be increased either by decreasing the background pressure or by increasing the density of atoms in the trap which is achieved by a higher atom number or a more confining trap geometry.

The dynamics of the system during the evaporative cooling process can be calculated to find the time evolution of $\omega_{\mathrm{rf}}(t)$ for which the desired temperature is reached with a minimum loss of atoms [Sac97]. However, since the calculations always involve some approximations, the process is optimized empirically by realizing a decreasing ramp $\omega_{\mathrm{rf}}(t)$ in several linear steps with different slopes, optimizing each slope for a large elastic collision rate.

Chapter 5

Experimental realization

5.1 Overview of the set-up

The design of the experiment is shown in Figure 5.1. A microchip is placed in the center of a cube-shaped high-vacuum chamber that is evacuated by an ion pump and a getter pump to pressures of some 10^{-10} mbar. The microchip is used to create magnetic fields by currents passing through its wires and, coated with a gold layer, serves as a mirror. Above the chip, the atom source, the so-called dispenser, is placed. It is a wire coated with ^{87}Rb. When running a current through the dispenser and thus heating it, ^{87}Rb atoms are released into the vaccum chamber. Laser beams enter the chamber from four directions, as indicated by the arrows in Figure 5.1. Two beams counterpropagate parallel to the chip surface, two beams are reflected under 90° from the surface of the chip. They overlap above the central wires of the chip. The lasers cool and trap the ^{87}Rb atoms, transfer

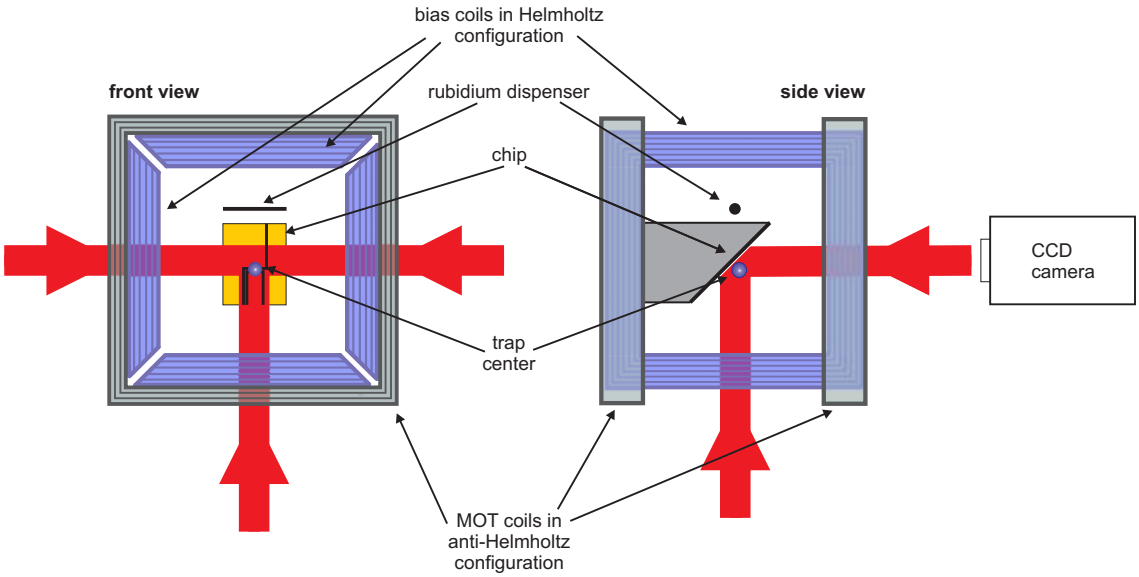


Figure 5.1: Design of the experiment.

them into suitable states and image the atoms. A charge coupled device (CCD) camera is the other main element of the imaging system.

There are three kinds of traps in the experiment: The light field for the two MOTs are created by the trapping lasers and their reflections from the chip. Such a type of MOT is often denoted as a mirror-MOT. The external MOT, for which the magnetic field is created by a pair of coils in anti-Helmholtz configuration, collects rubidium atoms from the background gas. The u-MOT is established by a current running through a u-shaped wire on the chip in combination with a magnetic bias-field made by two pairs of coils in Helmholtz configuration outside the vacuum chamber. It is used to transfer the atoms into the third trap, a magnetic trap which is created by a current through a z-shaped wire on the chip in combination with a magnetic bias field. In the magnetic trap, a BEC is achieved by forced evaporative cooling for which the rf magnetic field is created by yet another wire on the chip. Three pairs of coils (not shown in Figure 5.1) in Helmholtz configuration are employed to cancel the residual magnetic field at the position of the chip. With the different traps, the cloud of atoms can be placed at heights from 100 µm to 3 mm over the surface of the chip.

5.2 Production of the microchip

A picture of a microchip is shown in Figure 5.2 together with the layout of the wires. Shown are the u-wire, the z-wire and the wire that is used to create the rf-field for the evaporative cooling with the dimensions given in the drawing. The production of the microchip is sketched in Figure 5.3. The basis of the microchip is a 0.25 mm silicon wafer with an area of 16 mmx28 mm. The upper 100 nm of the silicon are oxidized to achieve an insulating layer. A 100 nm layer of titanium is deposited for a better adhesion of a following 100 nm layer of gold which is the basis for the wires. A layer of photoresist (PMMA) is applied onto the chip and spread by spinning. The PMMA is irradiated by UV-light through a glass mask on which the layout of the wires is applied by electron lithography. The development of the photoresist leads to trenches in which the gold wires are grown by electroplating. The maximum height of the wires depends on the thickness of the photoresist and was 6 µm in the present case. The photoresist is chemically taken off and the gold and titanium layers are removed by chemical etching so that the wires are electrically isolated. The production technique allows for a minimum width of the wires of 6-8 µm, a maximum height of 6 µm and a minimum separation of 2 µm. In order not to damage the wires by heating, the maximum current is 2 A in the z-wire and 4 A in the u-wire.

A 100 nm layer of titanium is applied to support the final 100 nm layer of gold which serves as a mirror for the laser beams. The surface must be sufficiently flat on a large scale so that a good reflection is possible. Defects on the surface with a wavelength that is comparable to the wavelength of the light can be the cause of diffuse scattering of the lasers. Therefore, the surface has to be as smooth as possible on a horizontal scale given

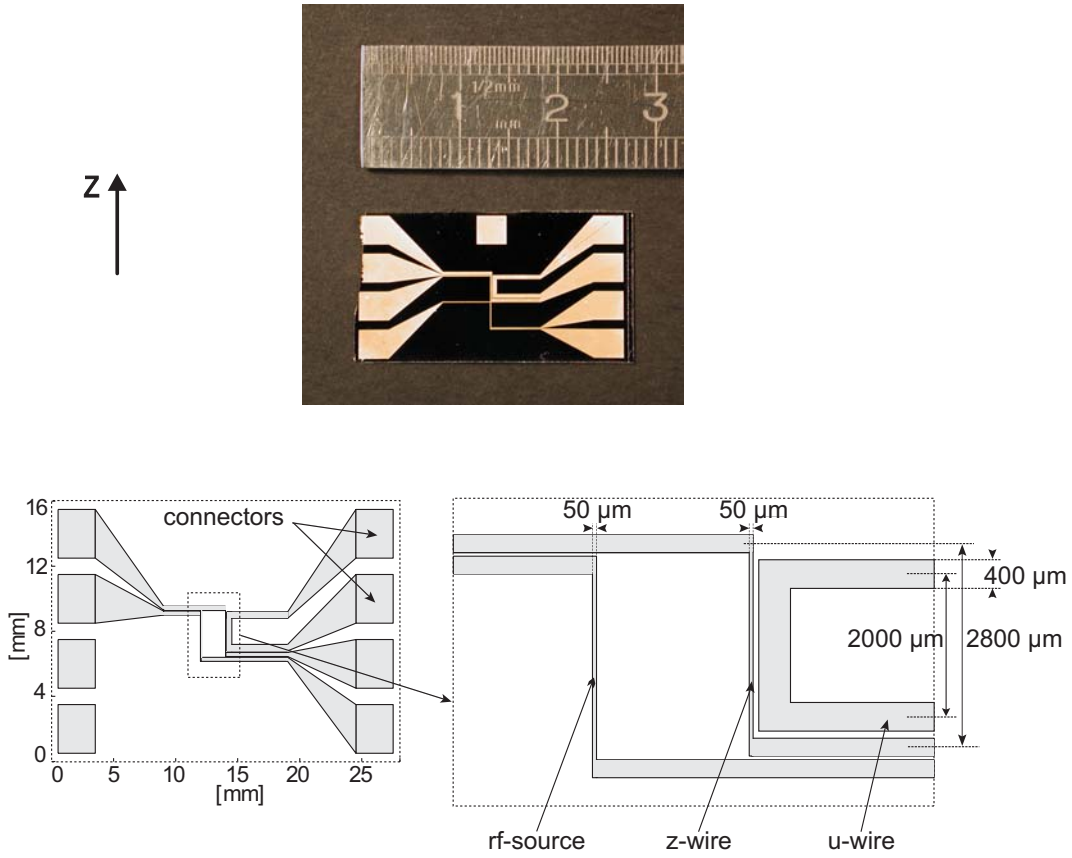


Figure 5.2: Layout of the microchip. Top: Photo of a microchip with an older design of the wires. Below: Schematic drawing of the present layout of the wires.

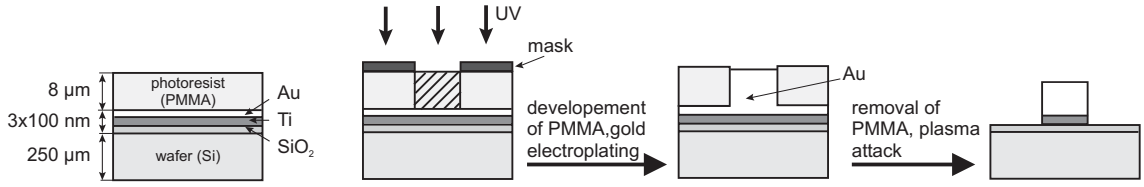


Figure 5.3: Production of the wires on the microchip. The silicon wafer is coated with layers of SiO_2, Ti, Au and PMMA. The PMMA is irradiated through a mask. After developing the mask, gold is electroplated onto the chip. After removing the photoresist the wires are insulated by chemical etching.

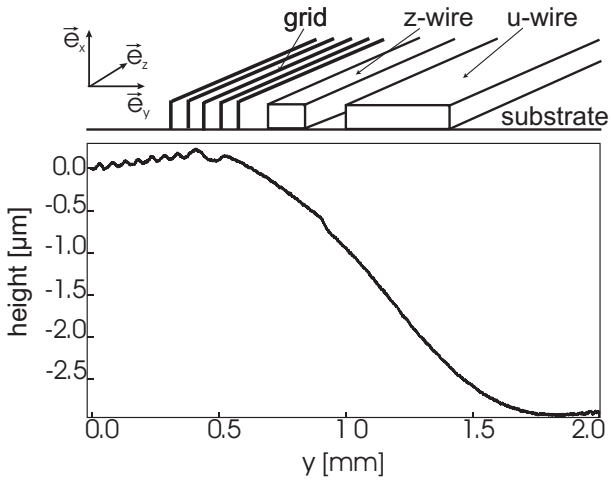


Figure 5.4: Height profile of the surface of the chip after applying a layer of BCB. Shown is a scan over a grid of wires (that is not used in the experiment), the z and the u-wire.

by the wavelength of the light. A smoothing was achieved before applying the titanium layer by covering the surface with a layer of BCB (benzocyclobutene), spinning the chip, and curing the BCB by heating. The process was repeated successively seven times. The height profile that was achieved can be seen in Figure 5.4. The drastic steps of the wires are smoothed out. Nevertheless, the surface still shows the structure of the wires on a vertical scale of 0.1 µm and a smooth step of 3 µm over a length of 2 mm. However, the surface is flat enough to serve as a mirror, the improvement of the surface with the BCB resulted in a larger number of atoms that were collected in the MOT.

5.3 Magnetic fields of the microwires

The magnetic fields of the wires are treated in two steps. First, the field from a current I in the central part of each of the wires in combination with a magnetic bias field $\mathbf{B}_{\text{bias}}$ is calculated. The central wire is modeled by an infinitely long wire. It runs in z-direction, as indicated in Figure 5.5, whereas the magnetic bias field is parallel to the chip surface in x-direction. The resulting magnetic field is

$$\mathbf{B} = \frac{\mu_0 I}{2\pi\,(x^2+y^2)} \begin{pmatrix} -y \\ x \\ 0 \end{pmatrix} + \begin{pmatrix} B_{\text{bias}} \\ 0 \\ 0 \end{pmatrix} \tag{5.1}$$

It is zero at the height $y = \frac{\mu_0 I}{2\pi B_{\text{bias}}} =: h$ and $x = 0$ on a line parallel to the wire at $x = 0$. Around this point the field can be approximated as

$$\mathbf{B}\,(x \ll h, h+\Delta, 0) = \frac{\mu_0 I}{2\pi h^2} \begin{pmatrix} \Delta \\ x \\ 0 \end{pmatrix} \tag{5.2}$$

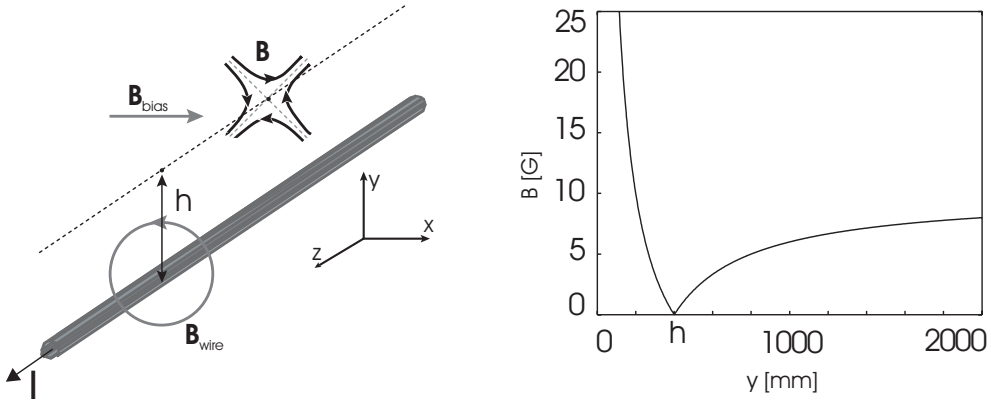


Figure 5.5: Magnetic field created by a current in an infinitely long wire and bias field. On the dotted line parallel to the wire in the left figure, the magnetic field vanishes. In the right figure, the magnetic field in y-direction and x=z=0 is given for a current of 2 A and a bias field of 10 G.

which is a two-dimensional quadrupole field in the (x,y)-plane. The principal axis $\hat{x}= x+y$ and $\hat{y}= y-x$ coincide with the laser beams.

By adding two side-wires, a u-wire is formed, as illustrated in Figure 5.6. The resulting magnetic field as used in the experiment is shown in Figure 5.6. The current is 2 A and the bias field (in x-direction) is 4.2 G. For the calculation, the finite length of the wires is taken into account but they are still assumed to be infinitely thin. The z-components of the magnetic field from the side wires cancel in the center of the central wire, so that the zero minimum of the magnetic field is maintained at $z = 0$ but shifted towards $x = 313\,\mu$m. The height is $y = 665\,\mu$m. In the vicinity of the minimum, the field can be approximated by a three-dimensional quadrupolar field, and in combination with the laser beams, the u-MOT is realized.

With the z-wire, the longitudinal components of the magnetic fields from the the side wires do not cancel, so that a trap with a non-zero minimum is produced. For a current of 2 A in the wire and a magnetic field of 8 G in x-direction, the resulting field is shown in Figure 5.7. The depth of the trap is given by B_{bias}. The magnetic field in a region around the minimum, which is located directly above the wire, can be approximated by a harmonic potential, hence an Ioffe-Pritchard type trap is created. The radial confinement is given mainly by the central wire whereas the longitudinal confinement is created by the side wires. The curvature of the trap, which determines the trap frequencies, as well as the height of the minimum above the wire and the minimum of the magnetic field can be controlled by the current and the external bias field. Calculated values for the parameters that are used in an experimental sequence are listed in Table 5.1. A more detailed treatment of the magnetic fields can be found in [Aus03].

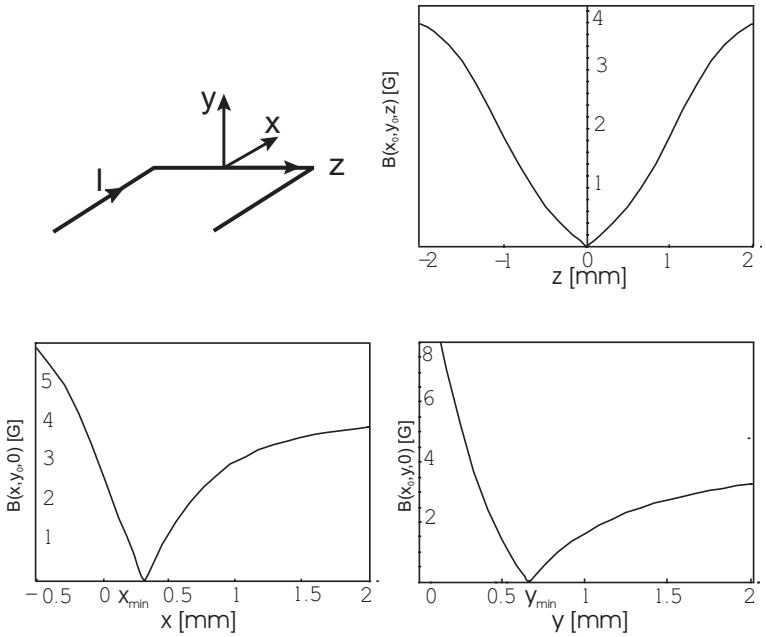


Figure 5.6: Magnetic fields created by the u-wire with a current of 2 A in the wire and an external magnetic field of 4.2 G in x-direction. The three graphs show the absolute value of the magnetic field in the three directions in space. Around the minimum, the field can be approximated by a linear function.

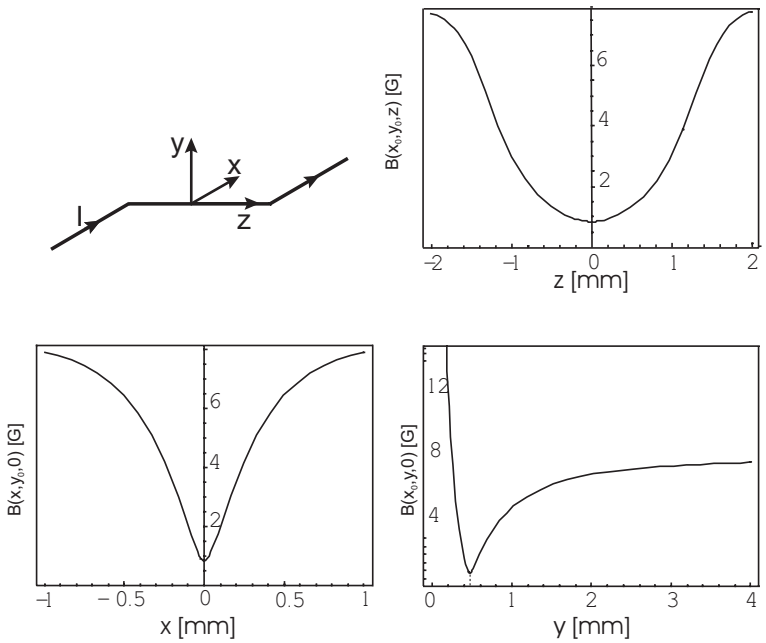


Figure 5.7: Magnetic fields created by the z-wire with a current of 2 A in the wire and an external magnetic field of 8 G in x-direction. The three graphs show the absolute value of the magnetic field in the three directions in space. Near the minimum, the field can be approximated by a parabola.

I[A]	B_{bias}	$h[\mu\text{m}]$	B_{min}	B_{r}'' [G / cm^{-2}]	B_{l}'' [G / cm^{-2}]
2	8	474	0.85	$4.2{\cdot}10^4$	166
2	15	262	0.50	$7.0{\cdot}10^5$	131
2	40	100	0.20	$8.2{\cdot}10^7$	57

Table 5.1: Parameters for the magnetic fields of the z-wire that are used in the experimental sequence. I: current through z-wire, h: height of minimum of field above wire, B_{min}: value of minimum of magnetic field, B_{r}'': radial curvature of field near minimum, B_{l}'': longitudinal curvature of field near minimum.

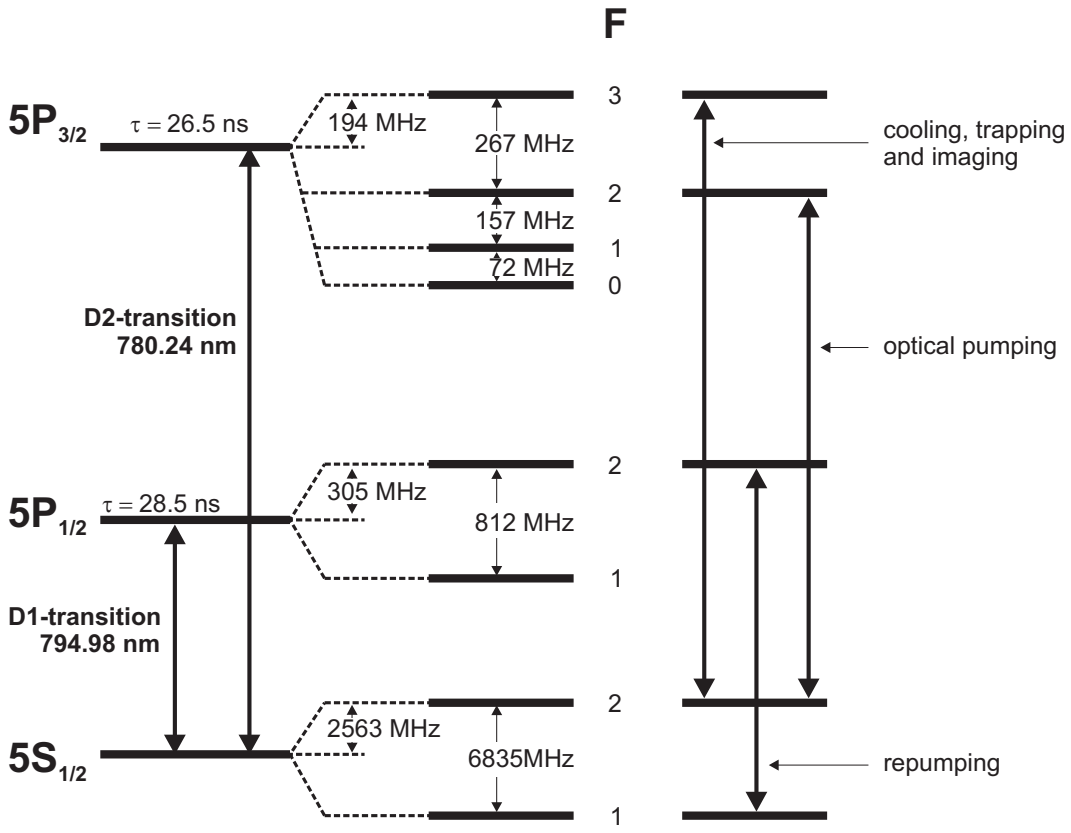


Figure 5.8: Optical transitions of ^{87}Rb. Given is the wavelength of the D1 and the D2 transition and the lifetime τ of the excited level and the energy of the corresponding hyperfine structure levels [Ari77]. On the right, the transitions are indicated that are used for cooling and trapping the atoms as well as imaging them.

5.4 Laser system

In order to achieve a closed cooling cycle, several laser frequencies are needed, as shown in Figure 5.8. The $5S_{1/2}$(F=2) $\rightarrow$ $5P_{3/2}$(F=3) transition is used for cooling and trapping from which the cooling and trapping beam is 14 MHz detuned to the red. The trapping laser beams are detuned by -16 MHz from the F=2 $\rightarrow$ F'=3 D2-transition. Thus, ^{87}Rb atoms are trapped in the F=2 sublevel of the $5S_{1/2}$ state. The transition is also used for imaging the atoms, the imaging beam is detuned by 0-20 MHz to the red. A repumping beam closes the cooling cycle. It is resonant to the $5S_{1/2}$(F=1) $\rightarrow$ $5P_{1/2}$(F=2) transition and pumps atoms from the untrapped $5S_{1/2}$(F=1) state into the trapped $5S_{1/2}$(F=2) state in which they do not interact with the repumping beam anymore. A third transition, $5S_{1/2}$(F=2) $\rightarrow$ $5P_{3/2}$(F=2), is used for reonantly pumping the atoms into the $5S_{1/2}$(F=2,m_F = 2) sublevel before transferring them into the magnetic trap.

The repumping beam comes from a free running Hitachi diode laser which is frequency stabilized to the F = 1 $\rightarrow$ F'=2 D1-transition by saturation spectroscopy. The other beams are produced by two Sanyo diode lasers. One of those, combined with a grating to form an external cavity, is locked to the crossover F$\rightarrow$(F' = 2 / F' = 3) of the D2-transition. It serves as a master laser to inject the second laser, after the frequency is shifted by double passing an acousto-optical modulator (AOM). In the course of an experiment, the frequency is set to the desired value by this AOM. The frequency stabilization scheme has a locking period of about one day and the linewidth of the lasers is around 1-2 MHz.

5.5 Imaging system

The density of the atom cloud is measured with a charge coupled device (CCD) camera by shining the imaging beam on the atoms and determining the fraction of light that is absorbed (absoption imaging). The imaging beam is passed from below through the cloud, reflected by the chip and imaged in x-direction by the camera (see Figure 5.9). By two lenses in a f/2f/f configuration, the cloud of cold atoms is imaged one-to-one onto the CCD chip of the camera. The achieved resolution is limited to $(9\,\mu m)^2$ by the size of pixels. For imaging a condensate having dimensions around 50 µm, the imaging system is extended with a third lens of the same focal length to realize an enlargement of three, thus increasing the resolution to $(3\,\mu m)^2$.

The fraction of transmitted intensity I_{trans} of the initial intensity I_{in} is measured by dividing the data obtained with a cloud by the data obtained without a cloud. It is connected to the density n by the relation

$$\frac{I_{trans}}{I_{in}}(y,z) = e^{-\sigma(\delta)\int n(x,y,z)dx}. \tag{5.3}$$

$\ln \frac{I_{trans}}{I_{in}}(y,z)$ is the optical density of the cloud in x-direction which is proportional to the column density $\int n(x,y,z)dx$. The absolute cross section of absorption σ is independent

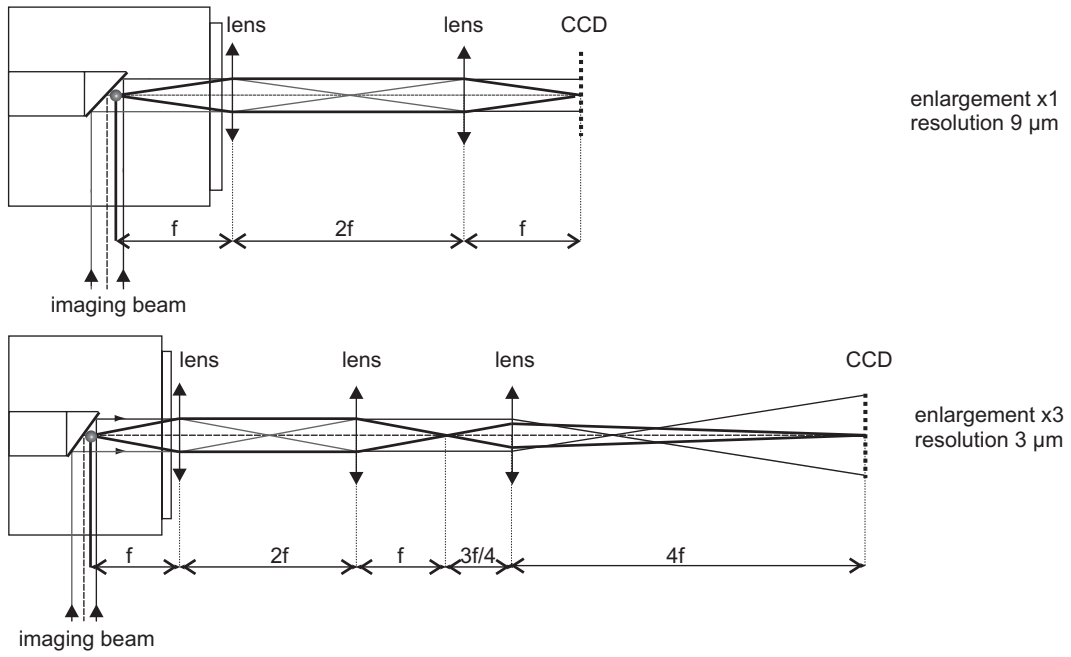


Figure 5.9: Principle of the imaging system.

of I for intensities that are small compared to the saturation intensity $I_{\mathrm{sat}} = \frac{\pi hc\Gamma}{3\lambda^3}$. I_{sat} is $1.7\,\mathrm{mW/cm^2}$ for the ^{87}Rb D2-transition and $\sigma(\delta)$ is then given by

$$\sigma(\delta) = \frac{\frac{3\lambda^2}{2\pi}}{1+\frac{4\delta^2}{\Gamma^2}}. \tag{5.4}$$

In the absence of a magnetic field, the imaging laser is tuned to resonance with the $\mathrm{F}=2 \rightarrow \mathrm{F}'=3$ D2-transition. The cloud is then imaged twice: once from the imaging beam directly and once after being reflected from the surface of the chip (Figure 5.10). Not only allows this a determination of the height of the cloud above the chip but it also projects the cloud onto two perpendicular planes, thus imaging the cloud in a three-dimensional way.

For some images, a magnetic field parallel to the surface of the chip is present. Thus, the imaging beam can be brought into resonance with only one of the Zeeman sublevels, of which the $\mathrm{F}=2, m_{\mathrm{F}}=2 \rightarrow \mathrm{F}'=3, m_{\mathrm{F}}=3$ D2-transition was used. Since the axis of the beam is not the quantization (z-) axis of the atomic spin, the polarization of the laser can be decomposed into σ^+, σ^- and π. Assuming that the imaging beam has a polarization of σ^- with respect to the y-axis that is indicated in Figure 5.10. For the direct imaging beam, the fraction of σ^+ light with respect to the quantization axis of the atomic spin is much larger (73%) than the fraction of σ^- (2%) polarized light leading to an effective cross section of the transition of $0.73{\cdot}\sigma(0)$ [Aus03]. When reflected, the direction of the circular polarized light is reversed, so that the effective cross section is $0.02{\cdot}\sigma(0)$. Thus, the image of the reflected beam is very weak compared to the direct beam. However,

when changing the initial polarization to σ^- with respect to the y-axis, the cloud will be measured by the reflected beam and a superposition of both images still yields the three-dimensional information about the cloud as described above.

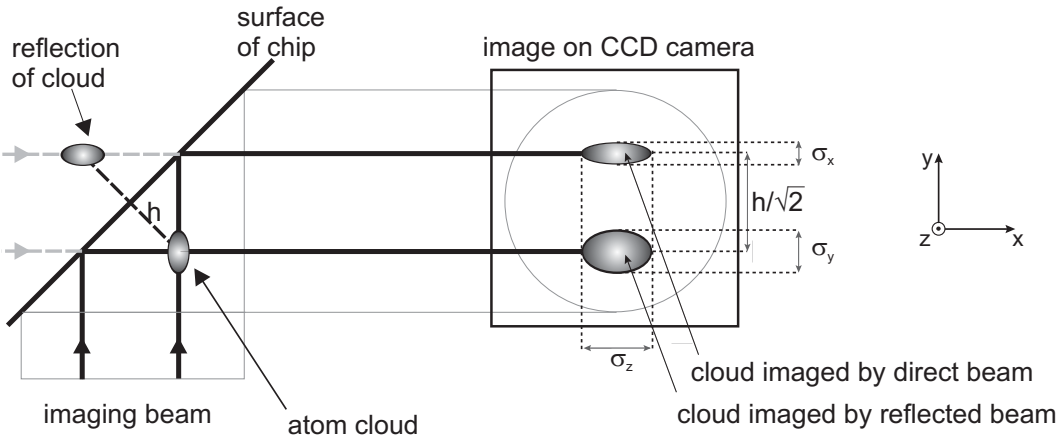


Figure 5.10: Principle of the imaging system. The density of the cloud is determined by measuring the fraction of light that is absorbed by the cloud. Due to the double imaging from the direct and the reflected imaging beam, the cloud is imaged in a 3-dimensional way. σ_i indicates the widths that can be measured.

The temperature of the cloud is measured by determining its size as a function of the time of free expansion. The width $\sigma(t)$ of the cloud after a time of flight t is given by

$$\sigma(t)^2 = \sigma(0)^2 + \frac{k_B T}{m} t^2 \tag{5.5}$$

By fitting a linear function to the measured values $\sigma_i^2(t_i)$, the temperature and the initial size of the cloud can be determined.

Chapter 6

Results and discussion

6.1 The way to a ^{87}Rb BEC on a microchip

This section is a brief summary of the experimental steps to a BEC. A detailed study of the performance of the traps and the determination of the experimental parameters can be found in [Aus03].

External MOT

For the collection of rubidium atoms from the background gas, the external MOT is used because the capture region of the external MOT is larger than the one of the u-MOT, limited mainly by the overlap of the laser beams. The external MOT coils are operated with a current of 8 A to create a magnetic field gradient of 30 G/cm. An experimental sequence begins with a 2.6 s current pulse of 8 A through the dispenser during which rubidium atoms are released into the vacuum chamber. From the start of the pulse, the external MOT is loaded in 10 s with atoms from the background gas. The times are a compromise between a short loading time of the MOT and a long lifetime of the atoms in the magnetic trap later on. The number of thus collected atoms is of the order of $3 \cdot 10^7$.

u-MOT

In a next step, the atoms are adiabatically transfered into the u-MOT which serves to transfer the atoms from the external MOT into the magnetic z-trap. A direct transfer would be more difficult for two reasons: In this set-up, the magnetic fields of the MOT have to be turned off very rapidly while the magnetic field of the magnetic trap is switched on since the nonzero minimum of the magnetic field of the MOT cannot be transfered adiabatically into the zero minimum of the magnetic trap. Because of the inductance of the external MOT coils, it is much easier to turn off the current in the u-shaped wire than in the MOT coils. A second reason for the u-MOT is that the MOT and the magnetic trap have to overlap spatially very well to avoid heating of the atoms during the transfer. Such an alignment is more difficult to achieve with external coils in comparison to the configuration with the chip where the alignment is quasi automatical. The transfer is done by rapidly ramping up the current in the u-wire to 4 A, after 3 ms

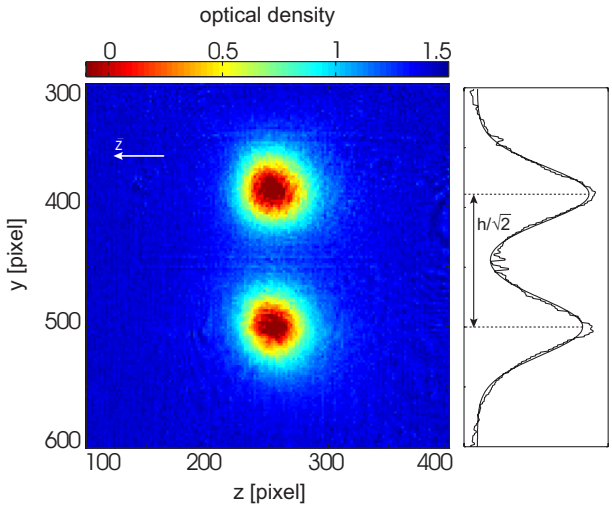


Figure 6.1: Left: Absorption image of cloud in u-MOT after transfer from the external MOT with the scale for the optical density given above the picture. The upper image is the reflection of the cloud. Right: Vertical profile of the density and a fit of two Gaussian functions. The image is taken after 3 ms of free expansion.

followed by ramping down the current in the MOT coils and ramping up the bias field to a value of 4.2 G. The sequence and values of the currents were optimized to obtain a maximum number of atoms in the magnetic trap. Thus, $2.5{\cdot}10^7$ atoms with a temperature of 140 μK are transfered into the u-MOT. It is localized 1.3 mm above the surface of the chip. An image of the cloud can be seen in Figure 6.1.

Preparation of transfer into magnetic trap

To overlap the cloud in the u-MOT with the magnetic trap, the cloud is compressed and moved closer to the surface 10 ms after the transfer. The current in the u-wire is ramped down to 2 A which brings a cloud of $2.2{\cdot}10^7$ atoms to a distance of 727 μm to the surface, the temperature of 140 μK remaining unchanged.

Since the magnetic trap created by the z-wire is not very deep (200-300 μK), the temperature of the cloud has to be decreased (< 50 μK) before the transfer to avoid major losses of atoms. This is achieved by ramping down all magnetic fields to zero and detuning the lasers by -80 MHz from the F=2→ F'=3 D2-transition during 7 ms, achieving a so-called molasses in which the atoms are cooled for 1.7 ms by Sisyphus cooling down to 40μK.

At this stage, the atoms are unpolarized, but only the fraction in the $m_F = 2$ state will be trapped in the magnetic trap (although the $m_F = 1$ state is principally a trapping state as well, the depth of the magnetic potential, being only half as deep as for the $m_F = 2$ state, is not sufficient to trap a significant number of atoms). The $m_F = 2$ fraction is increased by optical pumping: By establishing a quantization axis by a magnetic field of 7.5 G in z-direction, the degeneracy of the magnetic sublevels is lifted. By turning on the σ^+ polarized optical pumping beam, also incident in z-direction, tuned to the F=2→F'=2 D2 transition, the atoms are successively pumped during 50 μs into the $m_F = 2$ sublevel in which they do not interact with the laser field anymore.

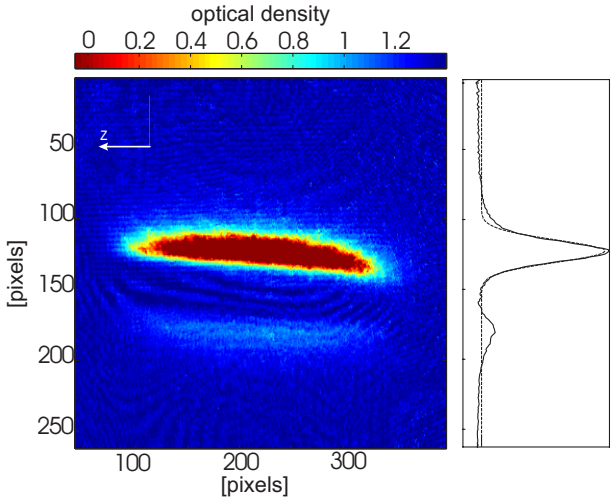


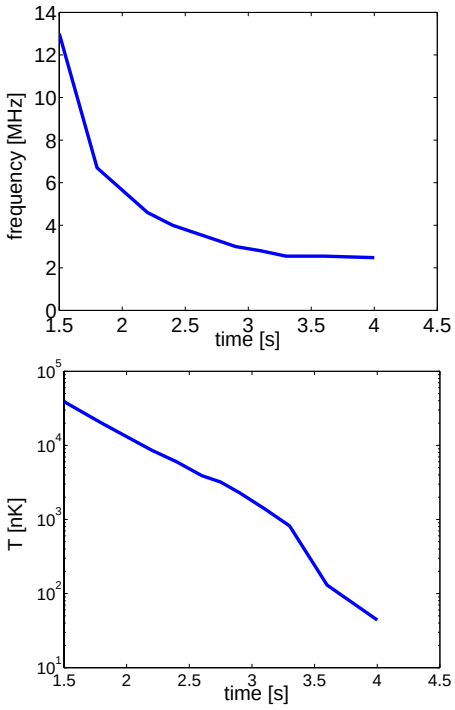
Figure 6.2: Absorption image of atoms in magnetic trap after 500 ms trapping time and 0.1 ms of free expansion. The bias field has not been switched off for imaging the atoms, so the cloud is imaged mainly by the direct imaging beam and only very faintly by the reflected imaging beam. The temperature of the cloud is 39 μK, $3.6{\cdot}10^6$ atoms are in the cloud.

Magnetic trap

0.6 ms after turning off the laser beams by an AOM and a mechanical shutter and changing the magnetic bias-field from zero to 8 G, the current in the z-wire is set to 2 A to establish the magnetic trap. Figure 6.2 shows a picture of the atoms that have been transferred into the magnetic trap. It is taken after 0.1 ms of free expansion of the cloud. Since it takes 3 ms to switch off the current in the external bias coils, the images of the atoms in the magnetic trap are always taken in the presence of the magnetic bias field resulting in only one image of the cloud, as described in section 5.5. There are $3.6{\cdot}10^6$ atoms in the cloud with a temperature of 39 μK and a density of $3{\cdot}10^{11}$ atoms / cm^3. The phase-space density is still seven orders of magnitude lower than needed for a phase transition.

Evaporative cooling and BEC

In order to increase the density and thus the rate of elastic collisions for a quicker evaporative cooling, the trap is compressed by increasing the external magnetic bias field to 40 G in 300 ms. Taking the trap parameters from Table 5.1 and assuming an adiabatic compression of the trap, the temperature is increased by a factor of 10 to 414 μK and the density to $1.0{\cdot}10^{13}$ atoms / cm^3. Thus, the elastic collision rate at the beginning of the forced evaporative cooling is in the order of 1000 s^{-1} as compared to a collision rate of a few 10 s^{-1} in the uncompressed trap. In the compressed trap, the minimum of the magnetic field is 0.2 G compared to 0.8 G in the uncompressed trap. Due to rf noise at 2 MHz that is present in the experiment, the lifetime of the atoms in the compressed trap would be significantly reduced by induced spin flips. An additional bias field in z-direction of 3.9 G is applied to displace the potential difference from the rf-component. This leads to a lifetime of the atoms in the compressed trap of about 10 s which is limited by the background pressure. Thus, the rate of losses is four orders of magnitude smaller than



no.	ν_{final} [MHz]	duration [ms]	T [μK]
1	13	1500	39
2	6.7	300	20
3	4.6	400	8.6
4	4	200	6.0
5	3.6	200	3.9
6	3.3	150	3.2
7	3	150	2.3
8	2.8	200	1.4
9	2.55	200	0.820
10	2.55	300	0.130
11	2.48	400	0.044

Figure 6.3: Evolution of the rf-frequency and of the temperature of the atoms during forced evaporative cooling. Given is the duration of each segment for which the frequency is decreased linearly to the final value ν_{final} together with the temperature T of the cloud at the end of the segment.

the elastic collision rate, so an important requirement for evaporative cooling is fulfilled.

Evaporative cooling is introduced by an oscillating current in the rf-source wire on the chip. The current is generated by a digital synthesizer which is amplified before passing through the wire. During the evaporation, the frequency is ramped down. If the ramping is too quick, the cloud does not rethermalize sufficiently while a slow ramping leads to atom losses due to the finite lifetime of the atoms in the trap. 11 segments of linear ramps have thus been determined, listed in Figure 6.1 together with the measured temperatures of the cloud. The parameters are plotted in Figure 6.1 Note that during the segment 10 the frequency is kept constant. During this time, the trap is decompressed by lowering the external bias field to 15 G to avoid severe losses by three-body collisions in the cloud due to the increasing density. At the end of the rf-ramp, a condensate is obtained.

Images of the cloud containing a Bose-Einstein condensate achieved with the above described parameters are shown in Figure 6.5 after different times of flight. A typical signature of a condensate is the bimodal distribution of the density: the density distribution of the condensate reflects the inverse form of the potential (see Equation 4.7), in this case a parabola, as seen in Figure 6.4[1] while the density of the thermal cloud is given by the Boltzmann law (Equation 4.8) which is a broad Gaussian. From the thermal part, the tem-

[1]The difference of the equation given in Figure 6.4 from a parabola comes from the fact that a column density is measured [Ket99].

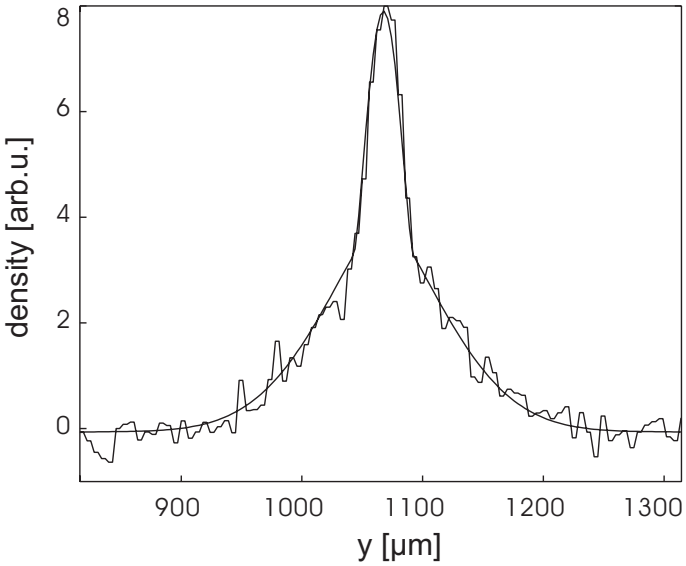


Figure 6.4: Density distribution. The density distribution has contributions from the Gaussian distribution of the thermal cloud and the parabolic distribution of the condensed fraction: The line is a fit of the function $n(y) = c_{\text{offset}} + c_{\text{th}} e^{-\frac{y^2}{\sigma_{\text{th}}^2}} + c_{\text{BEC}} \left(1 - \frac{y^2}{r_z^2}\right)^{3/2}$ to the experimental data.

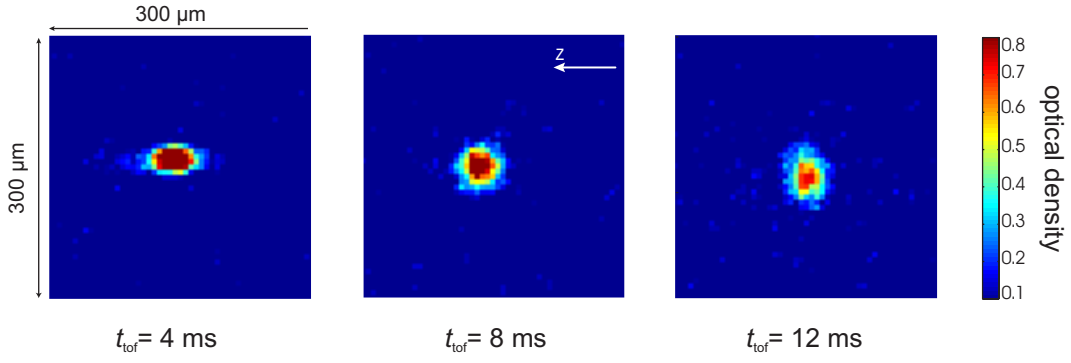


Figure 6.5: Absorption image of BEC after different times of flight t_{tof} as given below the pictures. The scale for the optical density is given on the right. The ellipticity, the ratio of the radial to the longitudinal size, increases from 0.50 over 0.99 to 1.46 (from left to right).

perature can be determined. The determination of the critical temperature as the onset of the bimodal distribution in combination with the trap frequencies was used to calibrate the measurement of the number of atoms. The number of condensed atoms is $1.5 \cdot 10^3$ atoms, corresponding to a fraction of 7.5%. A second signature of BEC is the time evolution of the aspect ratio, the ratio of the radial and longitudinal size of the cloud, refer to Figure 6.5. The density of the condensate is so large that the interaction energy dominates over the kinetic energy. The condensate does thus expand more quickly the larger the confinement of the trap is in the corresponding direction. In contrast, for a sufficiently thin thermal gas for which the interactions can be neglected, the initial velocity dominates over the interaction and the cloud will become eventually spherical independent of the initial shape.

In total, a BEC is achieved within 15 s which is a factor of 10 faster than in experiments that use macroscopic coils instead of a microchip. However, the resulting number of atoms in the BEC in the order of 10^3 is considerably lower by about a factor of 1000 [Lye02].

6.2 Roughness of the magnetic potential

In various experiments where atoms were held in magnetic traps formed by microstructures, a fragmentation of the atomic cloud was reported when the atoms were brought close to the wires [Lea03, Lea02, Kra02, For02, Jon03]. The reason for this is given either in inhomogenities in the conducting wires [Kra02] or in geometric deformation of the wire [Lea02] both leading to spatial dependent deviations of the current flow from the nominal path of the conductor and thus to a roughness of the magnetic field along the wire. It is interesting to note that in a configuration with a macroscopic copper wire with a diameter of 1.27 mm the phenomenon of fragmentation was not observed [Gus01].

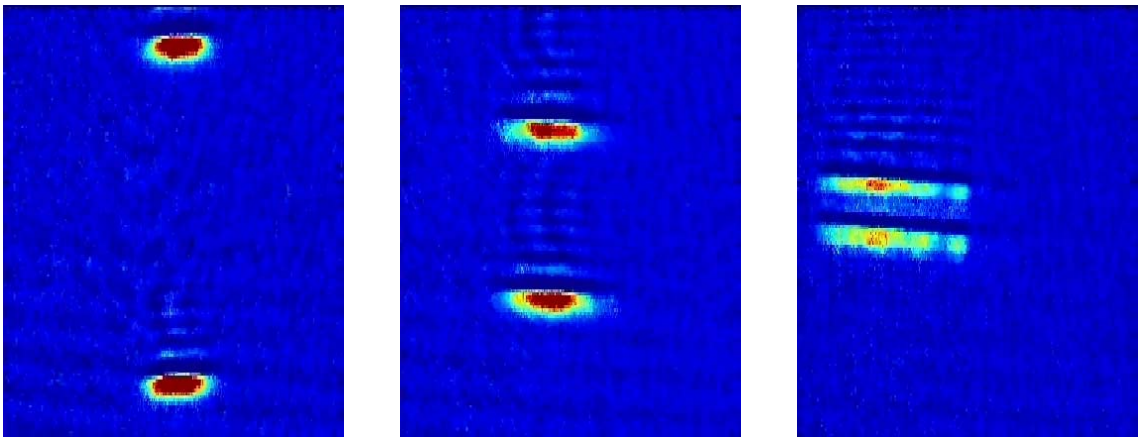


Figure 6.6: Absorption images of cloud at different heights above the wire. The height above the surface decreases from approximately 500 µm on the left to 50 µm on the right.

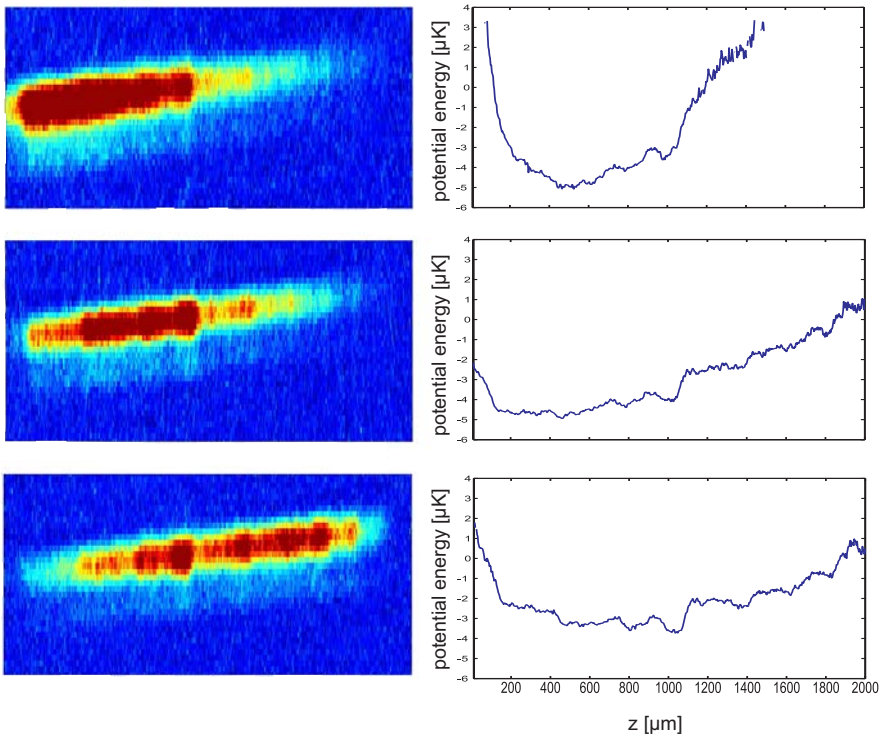


Figure 6.7: Left: Absorption image of cloud, shifted along the central wire by a magnetic field gradient in z-direction. Right: longitudinal potential $V(z)$ as calculated from the density distribution.

The density distributions of thermal clouds in the magnetic trap were measured for different heights of the clouds above the wire. As can be seen in Figure 6.6 in which the height decreases from 500 μm to 50 μm, the cloud is fragmented into several parts at small distances. In order to explore the wire in a larger range in longitudinal direction than the magnetic trap would allow at the chosen temperature, gradients $V_{\mathrm{grad}}(z)$ of up to 7 G/cm were applied in longitudinal direction to shift the cloud along the central wire as seen in Figure 6.7. Temperatures of the cloud of 0.5-2 μK were prepared by chosing the final value of the rf-ramp. Since the temperatures are well above T_{C}, the density n of the cloud depends on the magnetic trapping potential in the following way:

$$n = n_0 e^{-\frac{V(x,y,z)}{k_{\mathrm{B}}T}} \tag{6.1}$$

where n_0 is the peak density. $V(x,y,z)$ was checked to be separable into

$$V(x,y,z) = V(x,y) + V(z) \tag{6.2}$$

by measuring the radial size of the cloud at various positions z over the wire. At thermal equilibrium of the cloud, the transverse size is proportional to the curvature of the harmonic transverse potential $V(x,y)$. A maximum change in size of 13% was observed

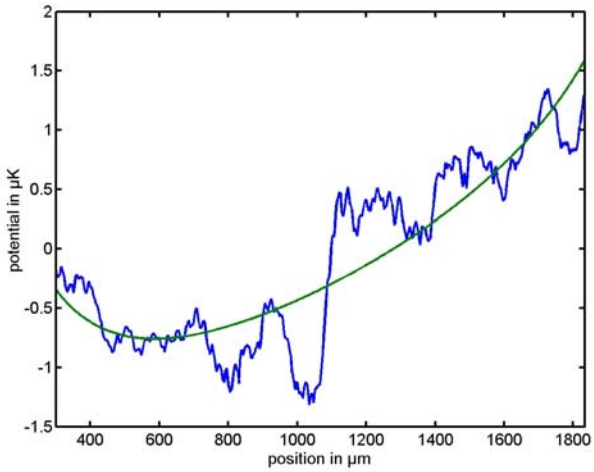


Figure 6.8: Measured potential $V_{\mathrm{trap}}(z)+V_{\mathrm{rough}}(z)$ in comparison with the fitted harmonic potential. The difference of the two curves give the roughness potential.

which is small enough to keep the assumption of separability. Thus, $V(z)$ can be extracted directly from

$$n(z) = n_0 \int dx \int dy \;\; e^{-\frac{V(x,y,z)}{k_{\mathrm{B}}T}} = \bar{n}_0 e^{-\frac{(V(z)}{k_{\mathrm{B}}T}}, \tag{6.3}$$

as shown in the right column of Figure 6.7. $V(z) = V_{\mathrm{trap}}(z)+V_{\mathrm{grad}}(z)+V_{\mathrm{rough}}(z)$ is the sum of the z-dependent component of the nominal trapping potential $V_{\mathrm{trap}}(z)$, the potential of the additionally applied gradient $V_{\mathrm{grad}}(z)$ and the potential $V_{\mathrm{rough}}(z)$ that causes the roughness of the potential, denoted as roughness potential. $V_{\mathrm{grad,i}}(z)$ were determined for each applied gradient by fitting a linear function to the corresponding measured $V_i(z)$ minimizing the differences between the different $(V_{\mathrm{trap}}(z)+V_{\mathrm{rough}}(z))_i$ in chosen overlapping regions. The fitted gradients were found to be in reasonable agreement with the expected ones. $V_{\mathrm{trap}}(z)+V_{\mathrm{rough}}(z)$ was obtained over a distance of 1500 µm by subtracting $V_{\mathrm{grad},i}(z)$ from $V_i(z)$ and averaging the results in the overlapping regions, as shown in Figure 6.8.

The trapping potential $V_{\mathrm{trap}}(z)$ of the z-wire and the bias field was found by modeling the z-wire by two infinitely long arms of finite width not taking into account the finite height of the wires. The height of the trap center above the wire and the length of the central wire were left as free parameters in a fit to the measured data. From the images, only the height above the chip surface could be obtained whereas the exact thickness of the BCB and gold layer over the wire was not known at this time. The thickness was measured later on and the experimental value of 12 µm was found to be in good agreement with the fitted value of 13 µm. The length of the central wire was left as a fitting parameter because when the measured length was taken, the fit was not very good. A physical reason might be found in curvatures of the current flow at the corners of the z. However, the fitted length was found to agree with the measured length within 4%. In Figure 6.8, the line indicates the determined $V_{\mathrm{trap}}(z)$. $V_{\mathrm{rough}}(z)$ is obtained by subtracting $V_{\mathrm{trap}}(z)$ from $V(z)$. The result,

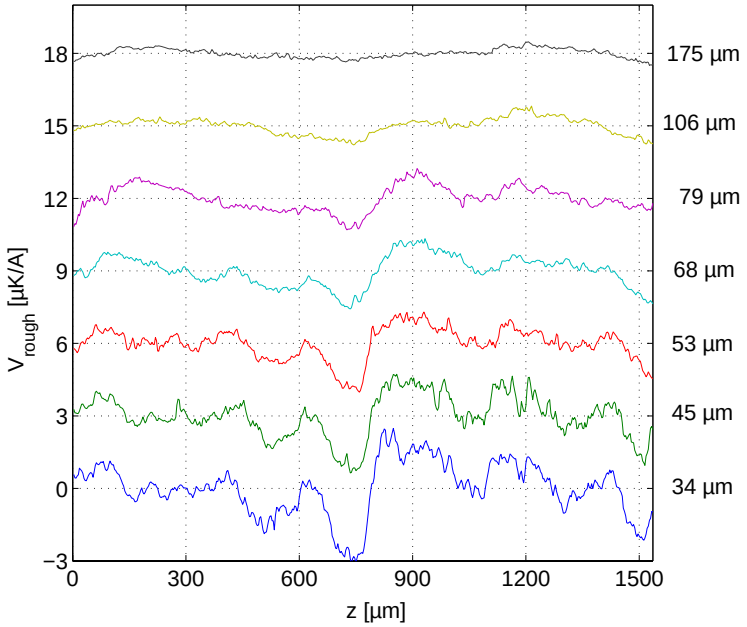


Figure 6.9: Roughness potential $V_{\text{rough}}(z)$ for different heights of the cloud above the wire. Each curve is shifted successively about 3 µK / A to the top for better visibility.

normalized to the current in the z-wire, is shown in Figure 6.9 for seven different heights of the cloud. The amplitude of $V_{\text{rough}}(z)$ clearly decreases with increasing distance from the wire. As opposed to the observation of other groups [Jon03], no obvious periodicity is seen. $V_{\text{rough}}(z)$ was checked to be both independent of the temperature of the cloud in the given range and to be linear with the current in the z-wire. Furthermore, it is stable in time. The temperatures of the clouds were chosen to be about three times larger than $V_{\text{rough}}(z)$.

A spectral analysis of $V_{\text{rough}}(z)$ was performed by calculating the power spectral density PSD_{V}. The power spectral density $PSD_f(k)$ of a function $f(z)$ that is given in an interval L is defined by

$$PSD_f(k) = \frac{1}{\pi L}\langle | \int dz\, f(z) e^{ikz} |^2 \rangle. \tag{6.4}$$

The normalization factors are chosen such that $\int_0^\infty PSD_f(k)dk$ is the square of the rms (root mean square) roughness given by $\frac{1}{L}\int f^{\,2}(z)dz$. The calculation was done with the pwelch method. The potential was devided into three segments with an overlap of 50% which were windowed with Hamming windows. The results for seven distances from the wire are shown in Figure 6.10 as a function of the wavenumber $k = 2\pi/\lambda$. Indeed, no periodicity is observed. Instead, the power spectral density PSD_{V} is distributed over a broad range of k with the maximum of the distribution shifted to smaller wavenumbers with increasing distance from the wire. The rms roughness decreases with the distance, as expected from Figure 6.9. Errors may have been introduced at small k by the fit of the length of the wire in the determination of $V_{\text{trap}}(z)$. The errors are not estimated here, but

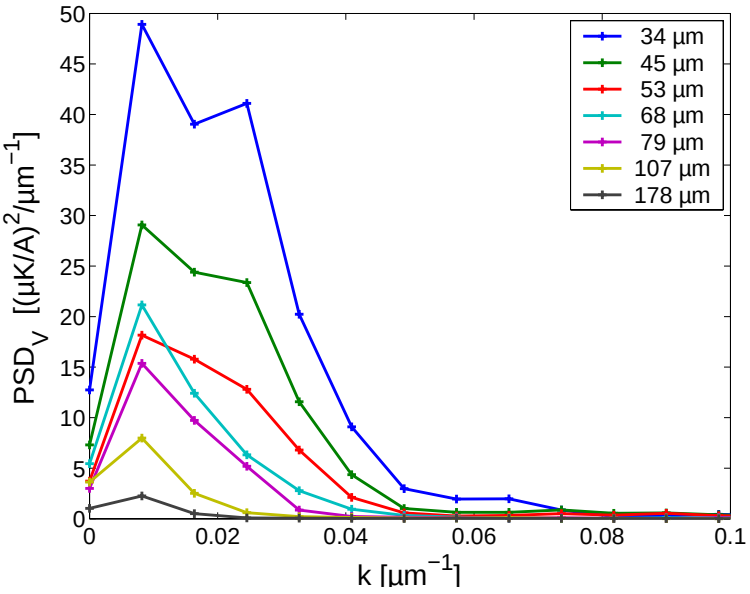


Figure 6.10: Power spectral density of measured roughness potential for heights above the wire as given in the graph.

it shall be noted that in any case possible errors would lead only to an underestimation of the power spectral density for small wavenumbers.

For a study of the origin of the roughness of the magnetic potential, the wire that was used for the measurements is characterized. The reflecting gold layer and the layer of BCB were removed by plasma etching to gain access to the wire. Figure 6.11 shows two images that were taken with an electron microscope. Clearly visible, the surface of the wire is quite rough. However, in the left picture it can be seen that the roughness in the direction perpendicular to the chip surface is negligible compared to the roughness in the two other directions. Images with different magnification were taken with the electron microscope from directly above the wire, like the one shown on the right in Figure 6.11, to quantify the roughness of the border of the wire. The border was determined from the greyscale pictures by chosing a threshold value of intensity and determining the position at which it was reached. The function of the position of the border $f_{\mathrm{wire}}(z)$ that was found in Figure 6.11 is drawn into the electron microscopy picture as a white line. From $f_{\mathrm{wire}}(z)$, a constant gradient and the mean value were subtracted. The result is shown in the left graph of Figure 6.12. The amplitude of $f_{\mathrm{wire}}(z)$ is typically 0.2 µm. The power spectral density $PSD_{\mathrm{wire}}(k)$ of $f_{\mathrm{wire}}(z)$ can be seen in the right graph of Figure 6.12. The calculation was done in the same way as described for PSD_{V}. Shown are two curves: The curve expanding to smaller wavenumbers is calculated from the average over two pictures with a scale of 5 µm per 469 pixel, like the ones shown in Figure 6.11, the other one is averaged over two pictures with a scale of 20 µm per 469 pixels, each picture of 1600 pixels length. The surface of the wire can be assumed to be correlated on a small scale but uncorrelated on a large scale. The power spectral density shows the thus expected course: a plateau for large wavelengths, as expected for white noise, and a drop with decreasing wavelength. Only wavelengths with wavenumbers of 0.1 μm^{-1} and less are of interest

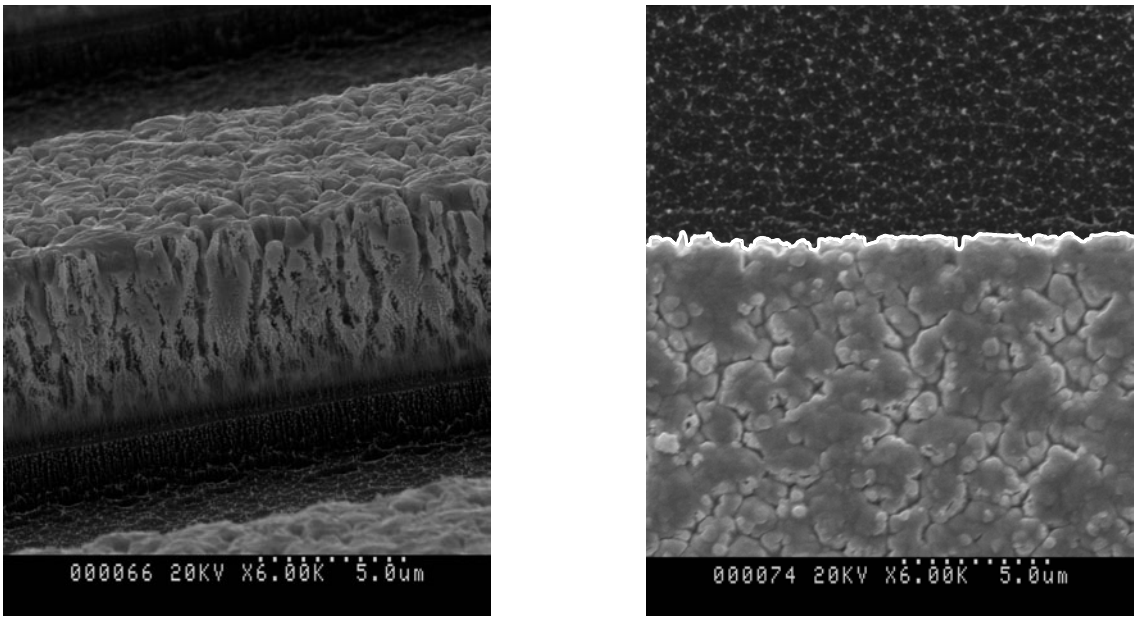


Figure 6.11: Electron-microscope picture of the central z-wire. The scale is given in the picture. Right: View is perpendicular with respect to the chip surface. The white line in the right picture indicates the extracted edge of the wire

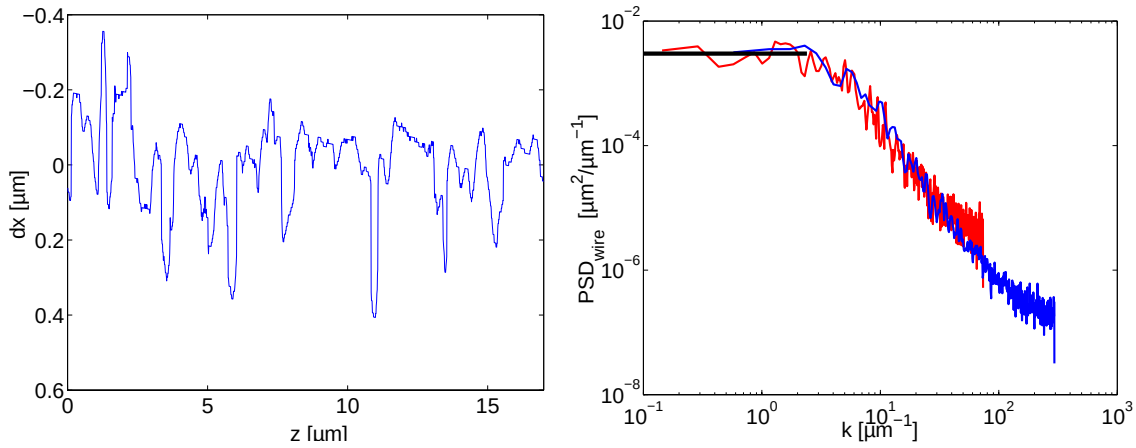


Figure 6.12: Left: Extracted line of Figure 6.11 after subtracting a constant gradient and the mean value. Right: Power spectral density of the edge of the wire. Shown are the average over two pictures of 68 µm, length, and the average over four pictures of 17 µm length. The thick line is an averarage over wavenumbers smaller than 3 μm^{-1}.

for the experiment (see Figure 6.10) which is the region of white noise of the wire. Thus, the values on the plateau in Figure 6.12 are averaged to get the (wavenumber independent) magnitude of the power spectral density of the white noise of large wavelengths. Points that correspond to wavenumbers smaller than $3\,\mu m^{-1}$ were averaged, resulting in a power spectral density of $0.003\,\mu m^2/\mu m^{-1}$.

Following the method of Lukin and coworkers [Wan03], from the power spectral density of the border of the wire $PSD_{wire}(k)$, the power spectral density of the magnetic potential that is caused by the border $PSD_{V,w}(k)$ can be calculated by

$$PSD_{V,w}(k) = \left(\mu_B \frac{\mu_0 I}{2\pi d}\right)^2 \frac{(kd)^4}{d^2} |K_1(kd) D(kW_0, kd)|^2 PSD_{wire}(k). \tag{6.5}$$

The term $\mu_B \frac{\mu_0 I}{2\pi d}$ is hereby the potential created by the nominal current in the wire. K_1 is the modified Bessel function of the second kind of order 1 and the function D is defined by

$$D(x,y) = \frac{2\sinh(x/2)}{x\sinh(x)K_1(y)} \sum_{n=0}^{\infty} \frac{(-1)^n}{n!(2y)^n} K_{n+1}(y)[\gamma(2n+1, x/2) - \gamma(2n+1, -x/2)] \tag{6.6}$$

where $\gamma(n,x)$ is the incomplete Gamma function. In the following, the sum is calculated with an upper limit of 20 for which $D(x,y)$ has converged for the considered x and y. To derive Equation 6.5, the height of the trap above the wire is assumed to be large compared to the height of the wire which is only the case for the larger distances that were measured. Contributions to the roughness potential from the roughness of the height of the wire are assumed to be small compared to the contributions from the roughness of the border and are neglected. $f_{wire}(z)$ is assumed to be small compared to the width of the wire and the slope of $f_{wire}(z)$ is much smaller than one which both is well fullfilled.

The power spectral density of the magnetic potential calculated with Equation 6.5 is shown in Figure 6.13 for the heights above the wire for which the measurements were done. The qualitative appearance is the same as for the measured potential.

The two sets of results are presented together in Figure 6.14 each box corresponds to a different height above the wire as indicated in the box. Obviously, the calculations from the border of the wire fail to explain the measured roughness potential: for small wavenumbers, the observed values are about a factor of 10 larger than the calculated ones. Furthermore, the calculated values decrease faster with the height than the measured ones. As mentioned above, the experimental values might be underestimated for large wavelengths which would lead to an even larger disagreement. The assumption of Lukin that the height above the wire shall be large compared to the height of the wire itself is not fullfilled in all cases. Surprisingly, the experimental and calculated results agree better for small heights of the cloud above the wire. For the calculations, only the fluctuations of the border were considered. The surface of the wire was characterized

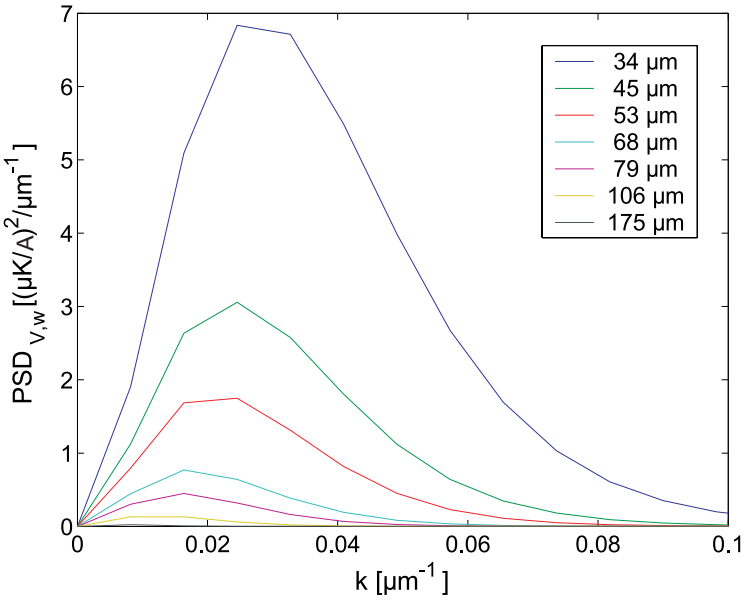


Figure 6.13: Power spectral density of the roughness potential as calculated from the power spectral density of the border of the wire for different heights as given in the graph.

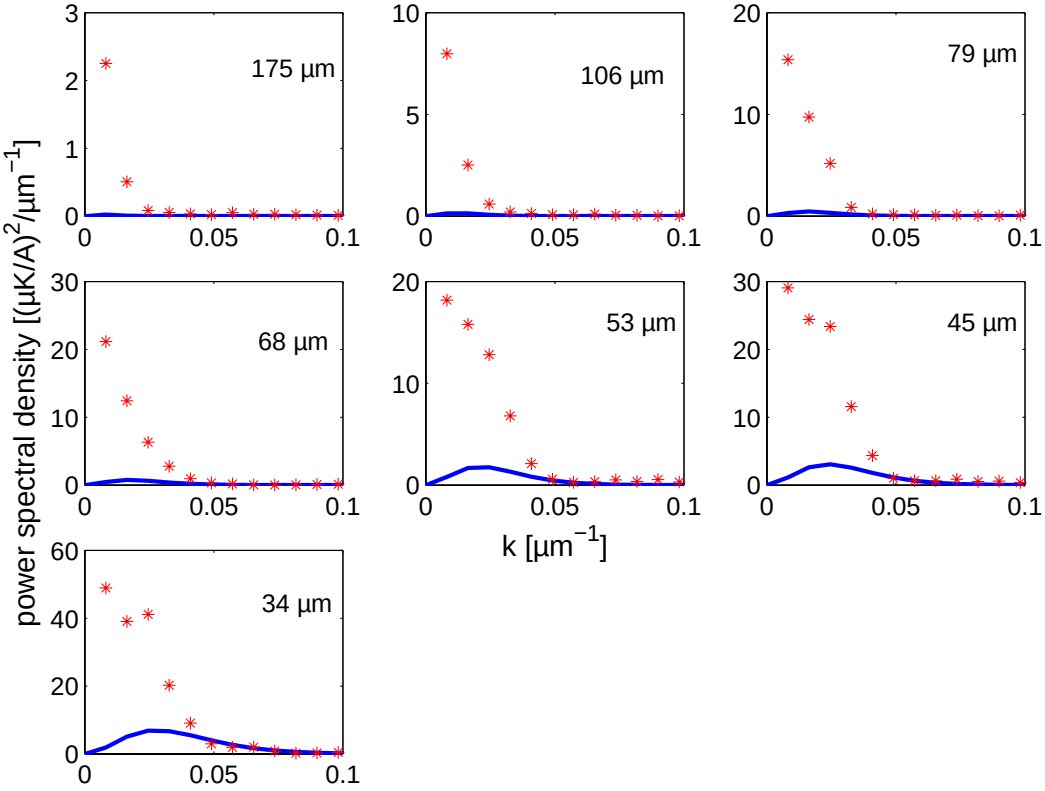


Figure 6.14: Power spectral density of measured roughness potential (symbols) in comparison with the one calculated from the roughness of the border of the wire (lines). The height above the wire is given in each box.

by an atomic force microscope and an independent calculation showed that the contribution of the surface to the roughness of the potential is indeed negligible compared to the one from the border [Bou03]. Concluding, most likely inhomogenities of the wire are the dominating reason for the fluctuations of the current causing the roughness potential. However, the results show that the roughness of the border of a wire that is used for a magnetic microtrap gives a lower limit for the roughness of the magnetic potential that can be expected.

Note added: After the work of this thesis was finished, the whole length of the wire was analyzed and unexpectedly it turned out that the assumption of white noise for small wavevektors was wrong. With the new data, the power spectral density increases considerably instead of remaining constant. With these results, the roughness potential as measured with the atoms could be reproduced by calculations from the wire profile [Est04]. Thus, for this microwire, the roughenss of the wire edge is really the dominating factor contributing to the roughness potential.

6.3 Prospects

Structures like beamsplitters or atomic wave guides can conveniently be realized and dynamically changed with the realization of magnetig traps by wires on a microchip. The principle has been demonstrated with thermal atoms [Den99, Cass00, Rei01]. However, the roughness of the magnetic field that was measured does not allow to coherently transport or split a BEC [Lea02]. In order to decrease the roughness, the chip was redesigned and is currently in production. The first layer of wires is lowered under the surface into chemically etched cuts of 15 μm depth. In these trenches, wires are produced with a similar technique as the old chip: optical lithography followed by electroplating. To fill the rest of the trenches, a layer of BCB is applied. The layer is cured by heating and then polished mechanically by spheres of AlO_2 with a diameter of 0.3 μm. This yields a flat surface on a large scale with scratches of 0.3 μm depth which are leveled by another 5 μm layer of BCB. By plasma etching, most of the BCB is removed again leaving a remaining roughness of 10 nm on a small scale and a curvature with an amplitude of 2 μm over 2 cm which is a large improvement in comparison to the old chip. After an earlier improvement of the optical quality, a larger number of atoms could be collected in the external MOT. If the number of atoms is still limited by the optical quality, the same effect should occur again. A larger number of atoms is desirable because it leads to shorter times for the evaporative cooling and a larger number of condensed atoms. Five wires of 500 nm width will be applied on the surface in a second layer. The design is such that one trap can be dynamically split into two. This opens the possiblilty of interference and tunneling experiments for which oscillation frequencies of 500 Hz are calculated. Wires of sub-μm dimensions cannot be produced by optical lithography. Instead, the photoresist is irradiated with an electron beam. After developing the photoresist, the small wires will be grown by evaporation to a height of 500 nm. Apparently, the gold does not stick to the surface of the BCB very well. The problem might be solved by switching to another resin. There are three reasons why the new chip is expected create a flatter trapping potential.

The production of the wires by evaporation instead of electroplating should lead to less impurities in the wire which are assumed presently to be the reason for the observed roughness of the potential. Furthermore, the amplitude of the current fluctuations is at least limited by the dimensions of the wires which will be decreased by a factor of 100. The border of the wires is expected to yield a roughness at least one order of magnitude less both in amplitude and in correlation length in comparison with the old chip. Furthermore, the realization of the magnetic field with five uncorrelated wires should decrease the resulting roughness approximately by a factor of $1/\sqrt{5}$. It is not possible to predict the roughness of the potential that the new chip will produce, however, it is expected to be much lower than the present one.

Summary

Optical collisions were studied in a crossed beams set-up. In contrast to optical collisions that are performed in gas cells, the observed collision event is well characterized. The method was established already for Na with atomic and molecular targets and was expanded to K and Ca collisions with argon.

The repulsive parts of the K-Ar XΣ and BΣ potential curves were derived from the interference pattern of differential cross sections of optical collisions. The accuracy is estimated to be 2-14 cm^{-1} depending on the interatomic distances larger than 6.0 a.u. on the XΣ and 5.5 a.u. on the BΣ curve. Such an accuracy is commonplace for potentials that are determined by the analysis of line spectra but was not achieved so far on the basis of scattering data. A confirmation by an independent approach would therefore be highly desirable. A comparison is possible at present for the repulsive branch of the XΣ state which was investigated on the basis bound-free spectra and gives a reasonable agreement. The repulsive branch of the BΣ potential has not been studied experimentally before. However, quantum chemical data reasonably agree with the present data. Deviations in the order of 50 cm^{-1} are within the expected accuracy of present day quantum chemical methods. By measuring the population ratio of the K fine-structure states after a collision event, the transition probability from BΣ to K($4p_{1/2}$) was probed which depends on details in the outer part of the BΣ and AΠ potentials. The good agreement of experiment and calculation confirms the spectrosopic results also in this region. An expansion of the method to binding parts of potential curves is possible and would complement the spectroscopic approach.

Nonadiabatic transitions in the outgoing channel of Na-molecule collisions were studied for the molecules N_2 and O_2. The results for N_2 are in very good agreement with theory. Calculations show a dependence on the rotational temperature of N_2. A comparison of theory to the O_2 data would be interesting. However, it is not possible at present due to the lack of potential curves. The expansion of the technique to other molecules as collision partners or other detunings is easily possible. Nonadiabatic transitions in the ingoing part of a collision can decide about the reactivity of the process. An understanding of the transition mechanisms might allow to manipulate chemical reactions.

The $^1S \rightarrow {}^1D$ transition that is probed in CaAr optical collisions is forbidden for the free Ca atom, but the excitation probability increases considerably in the presence of an Ar atom. The spectral dependence of the yield of excitated Ca atoms was measured, and the results are in good agreement with data from gas cell experiments. Fixing the detuning,

differential cross sections were obtained. The experimental results agree satisfactorily with *ab initio* calculations. The remaining disagreement is likely to a large part due to inaccuracies in the experimental determination of the collision energy. The expansion to an alkaline-earth+rare-gas system opens especially the opportunity to study spinchanging collisions.

Wires on a microchip were used to create the magnetic traps for obtaining a ^{87}Rb Bose-Einstein condensate. The roughness of the magnetic trap was characterized by measuring the spatial density distribution of a trapped thermal cloud of atoms for a range of distances to the wire. From the data available at the time of working on this thesis, it was found that the magnitude of the roughness cannot be explained by the roughness of the wire, so that inhomigenities inside the wire are believed to be the cause. However, the analysis of the complete wire edge revealed that fluctuations of the wire edge are indeed the dominating factor. A microchip is a promising approach to realize magnetic fields that act like beam splitters or wave guides for atoms. However, the roughness of the magnetic potential, that was observed also in many comparable experiments, currently prevents a coherent manipulation of a BEC. A new chip is being fabricated and is expected to produce a less rough magnetic potential.

Appendix

Appendix A

Derivation of the phase difference of two trajectories

Equation 1.15 for the phase difference will be derived. We start with the integral over the wavenumber in Equation 1.13, first only for the incoming part of the collision, which is the semiclassical phase $\phi(r)$:

$$\phi(r) = \int_R^r k(\mathbf{r})ds = \frac{m}{\hbar}\int_R^r |\dot{\mathbf{r}}|ds. \tag{A.1}$$

Since $\dot{\mathbf{r}}$ is always parallel to $\mathbf{ds}$, $|\dot{\mathbf{r}}|ds = \dot{\mathbf{r}}\mathbf{ds} = \dot{r}dr + r^2\dot{\varphi}d\varphi$ and thus

$$\begin{aligned}\phi(r) &= \frac{m}{\hbar}\int_R^r \dot{r}dr + \int_0^{\varphi(r)} \frac{mr^2\dot{\varphi}}{\hbar}d\varphi = \frac{m}{\hbar}\int_R^r \dot{r}dr + \frac{mvb}{\hbar}\int_0^{\varphi(r)} d\varphi \\ &= \frac{mv}{\hbar}\int_r^R \sqrt{1-\frac{V_1(r)}{E}-\frac{b^2}{r^2}}dr + kb\varphi(r)\end{aligned} \tag{A.2}$$

with $k = k(\infty) = mv/\hbar$. The phase $\phi(v,b)$ after the collision at R is calculated by integrating over the whole trajectory:

$$\phi(v,b) = \frac{mv}{\hbar}\int_{r_0}^R \left(\sqrt{1-\frac{V_1(r)}{E}-\frac{b^2}{r^2}} + \sqrt{1-\frac{V_2(r)}{E}-\frac{b^2}{r^2}}\right)dr + kb(\pi - \chi(v,b)) \tag{A.3}$$

The derivative with respect to b of the first addend in Equation A.3 is:

$$\frac{mv}{\hbar}\int_{r_0}^R \frac{-b}{r^2}\left(\frac{1}{\sqrt{1-\frac{V_1(r)}{E}-\frac{b^2}{r^2}}} + \frac{1}{\sqrt{1-\frac{V_2(r)}{E}-\frac{b^2}{r^2}}}\right) = k\left(\chi(v,b)-\pi\right) \tag{A.4}$$

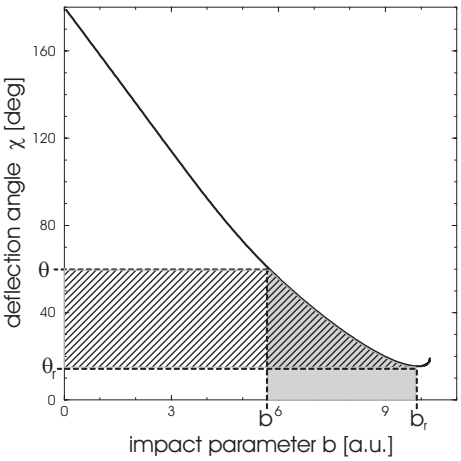


Figure A.1: Graphical illustration of Equation A.6 and Equation A.9. The shaded area is the integral in Equation A.9, the hatched area is the integral in Equation A.6. Apart from constant addends, each area is proportional to the phase of the corresponding trajectory.

Taking the antiderivative of the right part of Equation A.4 results in:

$$\frac{mv}{\hbar}\int_{r_0}^{R}\left(\sqrt{1-\frac{V_1(r)}{E}-\frac{b^2}{r^2}}+\sqrt{1-\frac{V_2(r)}{E}-\frac{b^2}{r^2}}\right)dr=-k\int_{b}^{b_r}\chi(b')db'-kb\pi+C \tag{A.5}$$

with the arbitrary integrating boundary chosen as b_r and an integration constant C. Inserting this into Equation A.3 results in the expression for the phase in Equation 1.14:

$$\phi(v,b)=-k\int_{b}^{b_r}\chi(b')db'-kb\chi+C. \tag{A.6}$$

The integral is the shaded area in Figure A.1. To derive the expression for the phase difference, the integral is transformed. For this, the deflection function is assumed to be invertible such that each scattering angle[1] θ can be assigned an impact parameter $b(\theta)$. If this is not the case (when there is more than one trajectory with different impact parameters leading to the same scattering angle as for example seen in Figure A.1 for impact parameters slightly larger than b_r), the integrals in the following considerations have to be broken down to regions where an inversion is possible. Substituting θ for b, the integral of Equation A.6 is:

$$k\int_{b}^{b_r}\chi(b')db'=k\cdot\left(\int_{\theta}^{\theta_r}b(\theta')d\theta'-b(\theta)\cdot\theta+b(\theta_r)\cdot\theta_r\right). \tag{A.8}$$

Inserting this into Equation A.6 results in

$$\phi(\theta)=-k\cdot\left(\int_{\theta}^{\theta_r}b(\theta')d\theta'+b(\theta_r)\cdot\theta_r+C'.\right) \tag{A.9}$$

[1]The experimentally accessible scattering angle θ is related to the deflection angle χ by

$$\theta=|(\chi+\pi)mod(2\pi)-\pi|. \tag{A.7}$$

It can be easily seen that apart from addends independent of θ, $\phi(\theta)$ is proportional to the hatched area in Figure A.1. As discussed in section 1.2, we turn to the case where two trajectories with different deflection functions contribute to the scattering angle θ. They have different impact parameters b_1 and b_2. The integration constant in Equation A.9 is the same for both trajectories for reasons of continuity at the largest possible impact parameter, so that the phase difference is given by

$$\begin{aligned}\Delta\phi(\theta) = &= k\left(2R+\int_{\theta}^{\theta_r} b_1(\theta')d\theta' + b(\theta_r)\cdot\theta_r\right) - \\ &\quad k\left(2R+\int_{\theta}^{\theta_r} b_2(\theta')d\theta' + b(\theta_r)\cdot\theta_r\right) \\ &= k\int_{\theta}^{\theta_r}\left(b_1(\theta')-b_2(\theta')\right)d\theta'. \end{aligned} \tag{A.10}$$

Appendix B

Conversion from optical collision laboratory to center of mass coordinates

Theoretical data are mostly calculated in the center of mass frame of the collision while experimental data are collected in a (rather arbitrary) laboratory frame. Therefore, a conversion from one set of coordinates to the other is necessary if theory and experiment shall be compared. A Newtondiagram (Figure B.1) illustrates this conversion. It displays the relevant vectors and angles that will be treated in this chapter. As a starting point, the projectile velocity $\vec{v}_{pr}$ and the target velocity $\vec{v}_t$ before the collision as well as the laboratory scattering angle shall be given as well as the masses of the particles. From these quantities, all other parameters in Figure B.1 can be deduced.

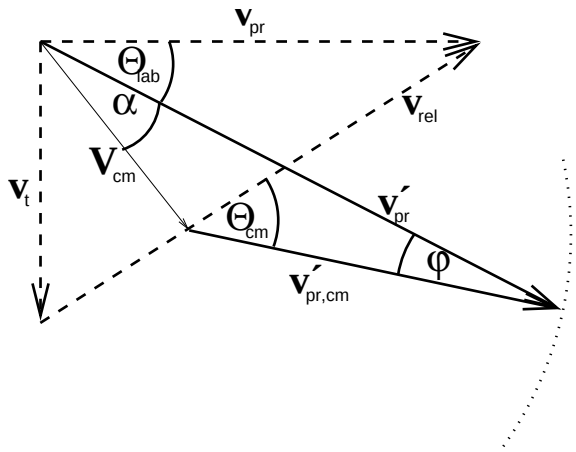


Figure B.1: Newtondiagram. Velocities before the collision (dashed): $\vec{v}_t$ (target), $\vec{v}_{pr}$ (projectile), and relative velocity $\vec{v}_{rel}$. $\vec{v}_{cm}$: center of mass velocity. Velocities after the collision (dashed): $\vec{v}'_{pr,cm}$ (projectile, center of mass coordinates), $\vec{v}'_{pr}$ (projectile). The dotted line inidicates a part of the Newtonsphere.

The relative velocity before the collision $\vec{v}_{rel}$ is defined by $\vec{v}_{pr}$ and $\vec{v}_t$:

$$\vec{v}_{rel} = \vec{v}_{pr} - \vec{v}_t. \tag{B.1}$$

The velocity of the center of mass

$$\vec{v}_{\mathrm{cm}} = \frac{m_{\mathrm{pr}}\vec{v}_{\mathrm{pr}} + m_{\mathrm{t}}\vec{v}_{\mathrm{t}}}{m_{\mathrm{pr}} + m_{\mathrm{t}}} \tag{B.2}$$

devides the relative velocity into the projectile and target velocity in the center of mass frame according to their mass ratio:

$$\vec{v}_{\mathrm{pr,cm}} = \frac{m_{\mathrm{t}}\vec{v}_{\mathrm{rel}}}{m_{\mathrm{pr}} + m_{\mathrm{t}}} \quad \text{und} \quad \vec{v}_{\mathrm{t,cm}} = -\frac{m_{\mathrm{pr}}\vec{v}_{\mathrm{rel}}}{m_{\mathrm{pr}} + m_{\mathrm{t}}}. \tag{B.3}$$

Following from the conservation of momentum, the center of mass velocity remains unchanged after the collision. If the collision is elastic, energy conversation demands an external addition of energy ΔE during the collision to be transformed into kinetic energy changing the length of the relative velocity about a corresponding value.

$$\frac{1}{2}m_{\mathrm{red}}\left(\vec{v}'_{\mathrm{rel}}\right)^2 = \frac{1}{2}m_{\mathrm{red}}\left(\vec{v}_{\mathrm{rel}}\right)^2 + \Delta E \qquad \Rightarrow \qquad \left|\vec{v}'_{\mathrm{rel}}\right| = \sqrt{\left(\vec{v}_{\mathrm{rel}}\right)^2 + \frac{2\Delta E}{m_{\mathrm{red}}}} \tag{B.4}$$

$m_{\mathrm{red}} = \frac{m_{\mathrm{pr}} \cdot m_{\mathrm{t}}}{m_{\mathrm{pr}} + m_{\mathrm{t}}}$ is the reduced mass of the system. Hence, the absolute values of the velocities of the scattered atoms in the center of mass frame are also known:

$$\left|\vec{v}'_{\mathrm{pr,cm}}\right| = \frac{m_{\mathrm{t}}\left|\vec{v}'_{\mathrm{rel}}\right|}{m_{\mathrm{pr}} + m_{\mathrm{t}}} \quad \text{and} \quad \left|\vec{v}'_{\mathrm{t,cm}}\right| = -\frac{m_{\mathrm{pr}}\left|\vec{v}'_{\mathrm{rel}}\right|}{m_{\mathrm{pr}} + m_{\mathrm{t}}}. \tag{B.5}$$

A selected direction $\vec{e}'_{\mathrm{pr}}$ in which the scattered projectile atoms are detected specifies a certain laboratory scattering angle θ_{lab} . The corresponding scattering angle in the center of mass frame θ_{cm} is found geometrically by intersecting $\vec{e}'_{\mathrm{pr}}$ with the Newtonsphere (a sphere around the end of the center of mass velocity of radius $|\vec{v}'_{\mathrm{pr,cm}}|$)[1]. For the calculation of the center of mass scattering angle, the angles α and φ as indicated in Figure B.1 are given by

$$\alpha = \arccos\left(\frac{\vec{e}'_{\mathrm{pr}} \cdot \vec{v}_{\mathrm{cm}}}{|\vec{v}_{\mathrm{cm}}|}\right) \tag{B.6}$$

$$\varphi = \arcsin\left(\frac{|\vec{v}_{\mathrm{cm}}| \cdot \sin\alpha}{|\vec{v}'_{\mathrm{pr,cm}}|}\right). \tag{B.7}$$

With this, the absolute value of the projectile velocity after the collision can be calculated:

$$\left|\vec{v}'_{\mathrm{pr}}\right| = \sqrt{\left|\vec{v}_{\mathrm{cm}}\right|^2 + \left|\vec{v}'_{\mathrm{pr,cm}}\right|^2 + \left|\vec{v}_{\mathrm{cm}}\right| \cdot \left|\vec{v}'_{\mathrm{pr,cm}}\right| \cdot \cos(\pi - \alpha - \varphi)}. \tag{B.8}$$

[1] In the case of the same target and projectile velocity before the collision with equal masses of target and projectile, simple geometric consideration show that the center of mass scattering angle is twice the laboratory scattering angle.

Finally, the center of mass scattering angle θ_{cm} is obtained:

$$\theta_{\mathrm{cm}} = \arccos\left(\frac{\left(\vec{v}'_{\mathrm{pr}} - \vec{v}_{\mathrm{cm}}\right)\vec{v}_{\mathrm{rel}}}{\left|\vec{v}'_{\mathrm{pr}} - \vec{v}_{\mathrm{cm}}\right|\left|\vec{v}_{\mathrm{rel}}\right|}\right). \tag{B.9}$$

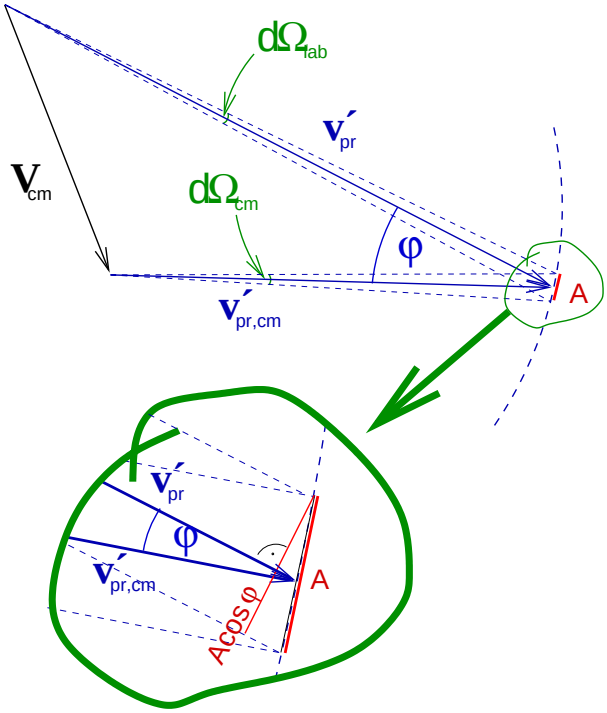


Figure B.2: Calculation of the Jakobi determinante. The two-dimensional surface of the Newton-sphere A is indicated by a onedimensional dashed circle.

The differential cross section in the laboratory frame can thus be transformed into the differential cross section in the center of mass frame:

$$\sigma_{lab}\left(\vec{v}_{\mathrm{pr}}, \vec{v}_{\mathrm{t}}, \theta_{\mathrm{lab}}\right) = \sigma_{cm}\left(\vec{v}_{\mathrm{rel}}, \vec{v}_{\mathrm{cm}}, \theta_{\mathrm{cm}}\right)\left|\frac{d\Omega_{cm}}{d\Omega_{lab}}\right|. \tag{B.10}$$

with the Jakobi determinant $\left|\frac{d\Omega_{cm}}{d\Omega_{lab}}\right|$ calculated by

$$d\Omega_{cm} = \frac{A}{r^2} = \frac{A}{\left(\vec{v}'_{\mathrm{pr,cm}}\right)^2} \qquad d\Omega_{lab} = \frac{A\cos\varphi}{\left(\vec{v}'_{\mathrm{pr}}\right)^2}$$

$$\Rightarrow \quad \left|\frac{d\Omega_{cm}}{d\Omega_{lab}}\right| = \frac{\left(\vec{v}'_{\mathrm{pr}}\right)^2}{\left(\vec{v}'_{\mathrm{pr,cm}}\right)^2\cos\varphi} \tag{B.11}$$

as it can easily be seen in Figure B.2.

Appendix C

Reference atomic transitions and conversion to SI units

system	reference transition	wavelength [nm]	energy [cm^{-1}]
K-Ar	$K(4s_{1/2}) \rightarrow K(4p_{1/2})$	770.109	12985.17
Ca-Ar	$Ca(4s^2)^1S \rightarrow Ca(4s3d)^1D$	457.674	21849.634
Na-molecule	$Na(3s_{1/2}) \rightarrow Na(3p_{1/2})$	589.755	16956.183

Table C.1: Atomic transitions that are used as reference transitions from which the detuning of the photon is given. Data are taken from [Bas75].

$1\,cm^{-1}$	$= 1.99 \cdot 10^{-23}$ J
1 MHz	$= 6.63 \cdot 10^{-34}$ J
1 eV	$= 1.60 \cdot 10^{-19}$ J
1 a.u. (length)	$= 5.29 \cdot 10^{-11}$ m
1 a.u. (mass)	$= 1.66 \cdot 10^{-27}$ kg
1 a.u. (transition dipole moment)	$= 8.48 \cdot 10^{-30}$ Asm

Table C.2: Conversion factors into SI units.

Appendix D

KAr differential cross sections and determined potentials

On the following pages, the data are presented that were used to determine the KAr potentials. The signal is multiplied by the sine of the laboratory scattering angle. Every box corresponds to a certain velocity of the scattered K atoms which is indicated at the side. The width of each velocity interval is 50 m/s. The data are given with error bars of one standard deviations including the statistical uncertainty. The lines are calculations from the potentials as determined in this work which are given at the end.

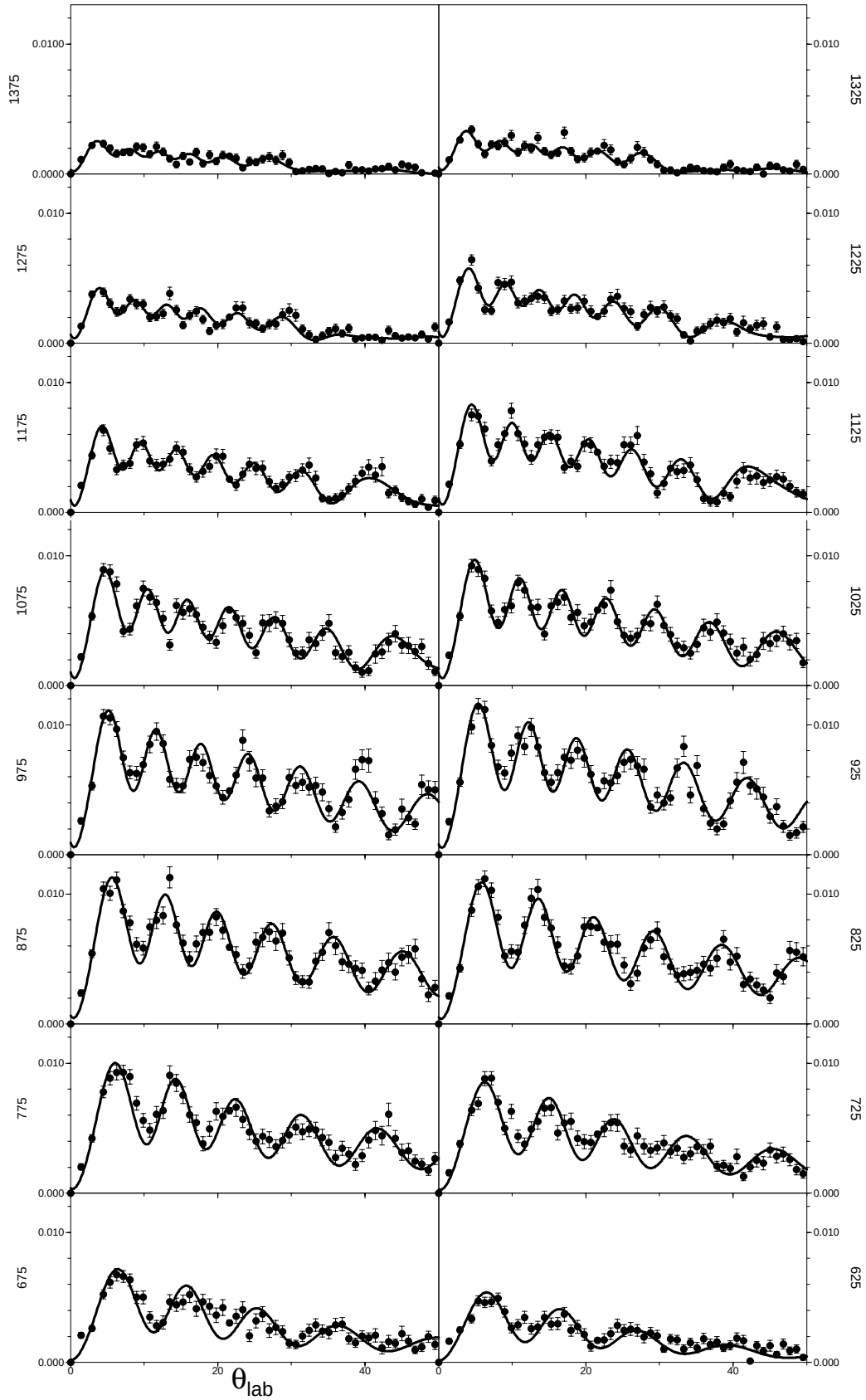


Figure D.1: Experimental differential cross sections (circles) in comparison with caluclations from the potentials of this work (lines). The velocity of the scattered potassium is given beside each box. Detuning: 220 cm^{-1}.

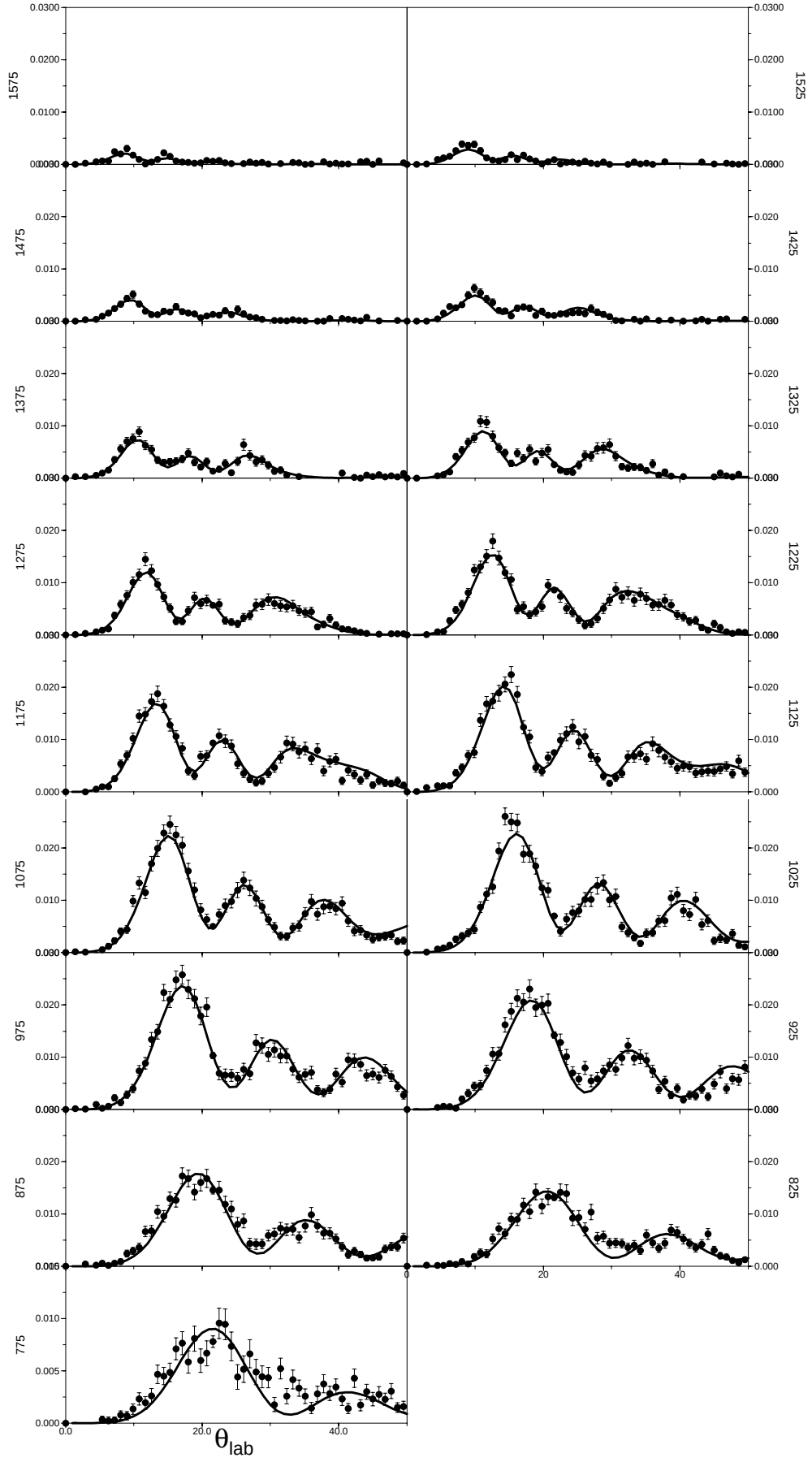


Figure D.2: Experimental differential cross sections (circles) in comparison with caluclations from the potentials of this work (lines). The velocity of the scattered potassium is given beside each box. Detuning: 480 cm^{-1}.

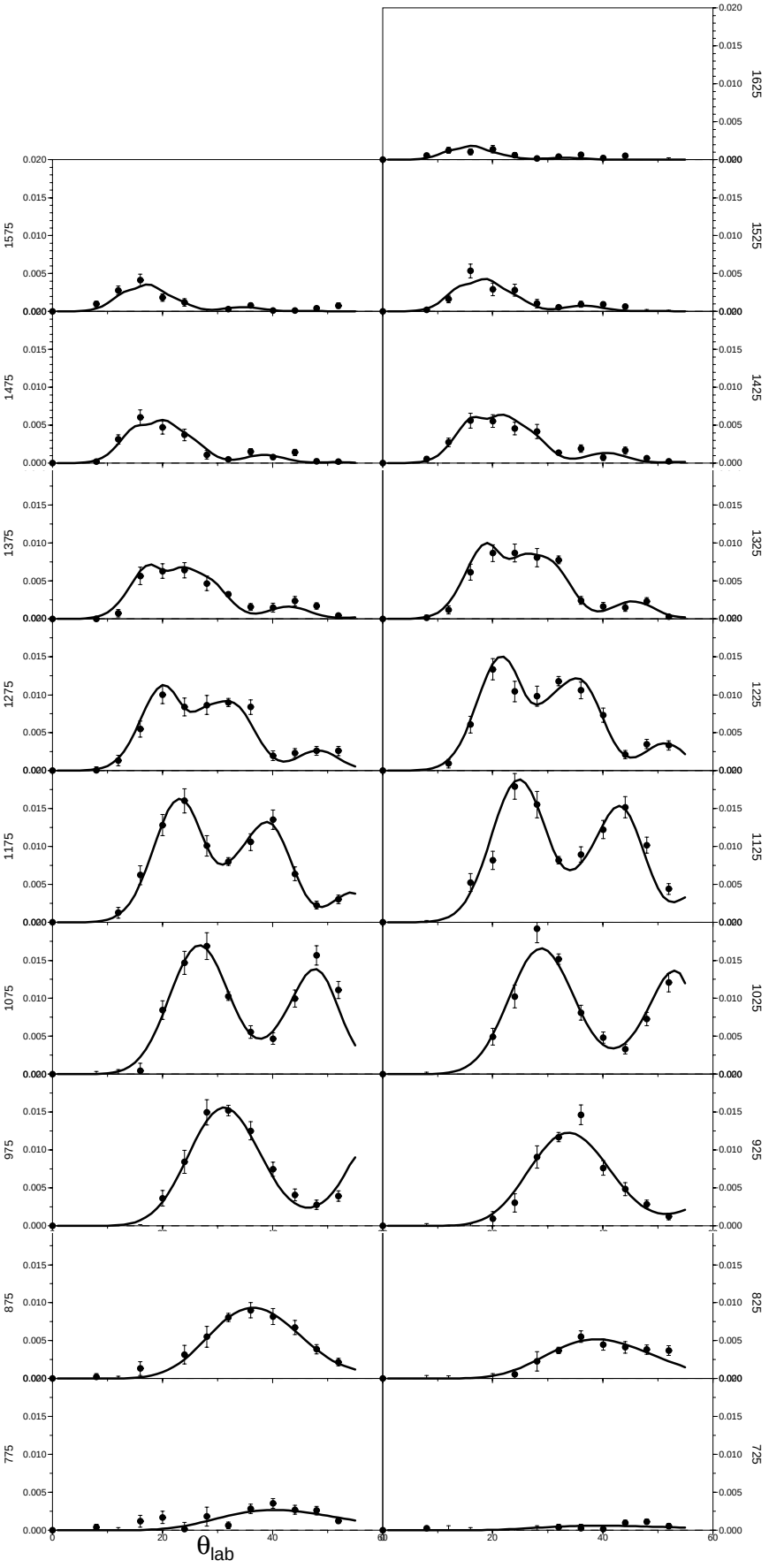


Figure D.3: Experimental differential cross sections (circles) in comparison with caluclations from the potentials of this work (lines). The velocity of the scattered potassium is given beside each box. Detuning: 640 cm^{-1}.

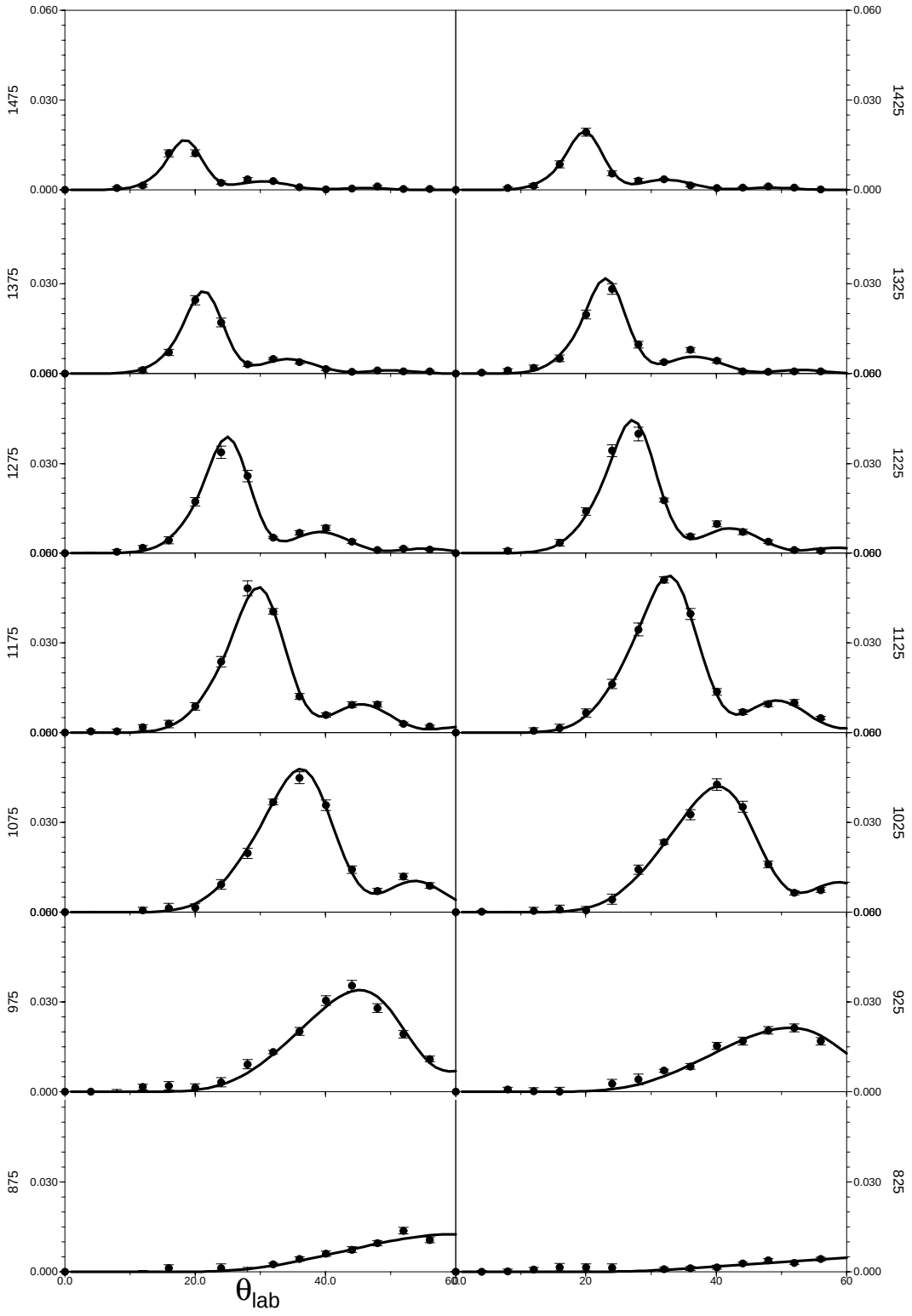


Figure D.4: Experimental differential cross sections (circles) in comparison with caluclations from the potentials of this work (lines). The velocity of the scattered potassium is given beside each box. Detuning: 720 cm^{-1}.

r [a.u.]	XΣ [cm^{-1}]	BΣ [cm^{-1}]	AΠ [cm^{-1}]
5.0			2286.7
5.2			988.5
5.4			259.2
5.6		1319.2	-133.4
5.8		1173.3	-330.2
6.0	675.2	1080.0	-415.6
6.2	527.6	1039.4	-440.1
6.4	420.4	1011.4	-432.7
6.6	338.0	983.4	-409.4
6.8	272.0	950.2	-379.2
7.0	217.7	908.6	-347.1
7.2	171.6	859.3	-315.6
7.4	132.4	804.2	-286.0
7.6	99.5	745.2	-258.7
7.8	71.9	683.8	-233.9
8.0	48.9	621.8	-211.6
8.2	29.4	560.7	-191.5
8.4	12.6	501.9	-173.4
8.6	-1.4	446.3	-157.7
8.8	-12.7	393.9	-142.6
9.0	-21.6	344.5	-129.4
9.4	-33.6	255.4	-106.9
9.8	-39.4	180.3	-88.7
10.2	-41.0	121.4	-73.7
10.6	-40.0	76.7	-61.5
11.0	-37.4	43.1	-51.5
11.5	-33.1	11.9	-41.5
12.0	-28.5	-9.1	-33.5
13.0	-20.1	-27.6	-22.3
14.0	-13.8	-30.1	-15.1
16.0	-6.9	-20.4	-7.4
18.0	-3.7	-11.0	-3.8
20.0	-2.1	-5.8	-2.1
22.0	-1.3	-3.2	-1.2
25.0	-.6	-1.5	-.6
28.0	-.3	-.7	-.3

Table D.1: Data of KAr potentials as determined in this work.

Appendix E

Physical properties of ^{87}Rb

mass	m = 1.44 10^{-25} kg
scattering length	a $\cong$ 5.7 nm
total differential cross section	$\sigma_{\text{tot}} = 8\pi a^2 = 7\ 10^{-16}\ \text{m}^2$
D_1 transition $^5S_{1/2} \leftarrow ^5P_{1/2}$	
wavelength	$\lambda_{D_1} = 794.76\ \text{nm}$
D_2 transition $^5S_{1/2} \leftarrow ^5P_{3/2}$	
wavelength	$\lambda_{D_2} = 780.02\,\text{nm}$
natural linewidth	$\frac{\Gamma}{2\pi} = 5.89\ 10^6\,\text{MHz}$
recoil velocity	$v_{\text{recoil}} = \frac{\hbar k}{m} = 6.02\,\text{mm}\,\text{s}^{-1}$

Bibliography

[All82] N. Allard and J. Kielkopf, *Effect of collisions on atomic spectral lines*, Rev. Mod. Phys. **54** (1982), 1103.

[All04] O. Allard, *private communication*, 2004.

[And95] M. Anderson, J. Ensher, M. Matthews, C. Wienman, and E. Cornell, *Observation of Bose-Einstein Condensation in a Dilute Atomic Vapor*, Science **269** (1995), 198.

[Ale02] M. H. Alexander, G. Capecchi, and H. Werner, *Theoretical Study of the Validity of the Born-Oppenheimer Approximation in the* Cl + H_2 *reaction*, Science **296** (2002),715.

[Ari77] E. Arimondo, M. Inguscio, and P. Violino, *Experimental determination of the hyperfine structure in the alkali atoms*, Rev. Mod. Phys. **49** (1977), 31.

[Aus03] C. Aussibal, *Réalisation d'un condensat de Bose-Einstein sur une microstructure*, Ph.D. thesis, Université Paris XI Orsay, 2003.

[Ban94] A. D. Bandrauk (ed.), *Molecules in Laser Fields*, Marcal Dekker Inc., New York, 1994.

[Bas75] S. Bashkin and J. O. Stoner, Jr., *Atomic Energy Levels and Grotrian Diagrams*, vol. 1, North-Holland Publishing Company, Amsterdam, 1975.

[Beh96] W. Behmenburg, A. Makonnen, A. Kaiser, F. Rebentrost, V. Staemmler, M. Jungen, G. Peach, A. Devdariani, S. Tserkovnyi, A. Zagrebin, and E. Czuchaj, *Optical transitions in excited alkali + rare-gas collision molecules and related interatomic potentials:* Li^* + He, J. Phys. B **29** (1996), 3891.

[Bic00] E. N. Bichutskaya, A. Z. Devdariani, and A. L. Zagrebin, *Quasi-Molecular Emission and Nonadiabatic transitions: II.* $Ca(4s4p\ ^1P, 4s3d\ ^1D) - He(1s^2, ^1S_0)$ *Quasi-Molecule*, Optics and Spectroscopy **88** (2000), 163.

[Bok96] F. Bokelmann and D. Zimmermann, *Determination of the* K-Ar *interaction potential in the* $X\Sigma$ *and* $A\Pi$ *state from laser spectroscopic data*, J. Chem. Phys. **104** (1996), 923.

[Bou03] I. Bouchoule, *private communication*, 2003.

[Bra94] U. Brackmann, *Lambdachrome® Laser Dyes. Data Sheets*, Lambda Physik GmbH, Göttingen, 1994.

[Brad95] C. C. Bradlay, C. A. Sackett, J. J. Tollet, and R. G. Hulet, *Evidence of Bose-Einstein condensation in an atomic gas with attractive interactions*, Phys. Rev. Lett. **75** (1995), 1687.

[Brau02] M. Braune, *Optisch-optische Doppelresonanzexperimente an Kalium-Argon und Bestimmung der adiabatischen Potentiale sowie der Spin-Bahn-Funktion im $B^2\Sigma$ -$A^2\Pi$- System*, Ph.D. thesis, Technische Universität Berlin, 2002.

[Bru91] R. Bruehl, J. Kapetanakis, and D. Zimmermann, *Determination of the* Na-Kr *interaction potential in the X-Sigma and A-Pi state by laser spectroscopy*, J. Chem. Phys. **94** (1991), 5865.

[Bur85] K. Burnett, *Collisional redistribution of radiation* , Phys. Rep. **118** (1985), 339.

[Cass00] D. Cassettari, B. Hessmo, R. Folman, T. Maier, and J. Schmiedmayer, *Beam Splitter for Guided Atoms*, Phys. Rev. Lett. **85** (2000), 5483.

[Cast01] Y. Castin, *Bose-Einstein condensates in atomic gases: simple theoretical results*, Coherent atomic matter waves (R. Kaiser, C. Westbrook, and F. Davis, eds.), EDP Sciences and Springer-Verlag, 2001.

[Chi74] M. S. Child, *Molecular Collision Theory*, Academic Press, London, 1974.

[Chi91] M. S. Child, *Semiclassical Mechanics with Molecular Applications*, International series of monographs on chemistry, Clarendon Press, Oxford, 1991.

[Coh92] C. Cohen-Tannoudji, J. Dupont-Roc, and G. Grynberg, *Atom-Photon Interactions*, John Wiley & Sons, Inc., New York, 1992.

[Coh96] C. N. Cohen-Tannoudji, *Cours de physique atomique et moleculaire*, College de France, 1996.

[Coh98] C. N. Cohen-Tannoudji, *Manipulating atoms with photons*, Rev. Mod. Phys. **70** (1998), 707.

[Cor99] E. A. Cornell, J. R. Ensher, and C. E. Wieman, *Experiments in dilute atomic Bose-Einstein condensation*, Proceedings of the International School of Physics “Enrico Fermi”, Course CXL, Bose-Einstein Condensation in Atomic Gases (M. Inguscio, S. Stringari, and C. E. Wieman, eds.), Societa Italiana di Fisica, 1999.

[Cou87] J. Coutts, S. K. Peck, and R. Stoner, *Effect of collisions on forbidden lines*, J. Appl. Phys. **62** (1987), 3514.

[Cou88] J. Coutts, S. K. Peck, and J. Cooper, *Collisional-induced absorption in calcium rare-gas collisions*, J. Appl. Phys. **64** (1988), 977.

[Cra93] J. K. Crane, M. J. Shaw, and R. W. Presta, *Measurement of the cross sections for collisional broadening of the intercombination transition in calcium and strontium*, Phys. Rev. A **49** (1993), 1666.

[Czu89] E. Czuchaj, F. Rebentrost, H. Stoll, and H. Preuss, *Semi-local pseudopotential calculations for the potential energies of the* CaHe *and* CaHe *systems*, Chem. Phys. **138** (1989), 303.

[Czu91] E. Czuchaj, F. Rebentrost, H. Stoll, and H. Preuss, *Pseudopotential SCF/CI calculation for the potential energy curves of the* CaHe *pair*, Chem. Phys. Lett. **182** (1991), 191.

[Czu02] E. Czuchaj, private communication, 2002.

[Czu03] E. Czuchaj, M. Krosnicki, and H. Stoll, *Valence ab initio calculation of the potential energy curves for ca-rare gas van der waals molecules*, Chem. Phys. **292** (2003), 101–110.

[Dal99] F. Dalfovo, S. Giorgini, L. P. Pitaevskii, and S. Stringari, *Theory of Bose-Einstein condensation in trapped gases*, Rev. Mod. Phys. **71** (1999), 463.

[Dav95] K. B. Davis, M.-O. Mewes, M. R. Andrews, N. J. van Druten, D. S. Durfee, D. M. Kurn, and W. Ketterle, *Bose-Einstein condensation in a gas of sodium atoms*, Phys. Rev. Lett. **75** (1995), 3969.

[Den99] J. Denschlag, D. Cassettari, and J. Schmiedmayer, *Guiding Neutral Atoms with a Wire*, Phys. Rev. Lett. **82** (1999), 2014.

[Dev86] A. Devdariani and A. L. Zagrebin, *Spin-changing collisions in the* Ca$(4s5p\,^1P_1)$+He *system*, Chem. Phys. Lett. **131** (1986), 197.

[Dev97] A. Devdariani, E. Tchescnokov, E. I. Dashevskaya, and E. E. Nikitin, *Quasi-classical study of differential inelastic scattering of oriented* Ca$(4s5p,^1P_1)$ *atoms on* he, Phys. Rev. A **57** (1997), 4472.

[Dür82] R. Düren, E. Hasselbrink, and G. Moritz, *On the Interaction of Excited Alkali Atoms with Rare Gas Targets in Scattering Processes*, Z. Phys. A **301** (1982), 1.

[Ens96] J. R. Ensher, D. S. Jin, M. R. Matthews, C. E. Wieman, and E. A. Cornell, *Bose-Einstein Condensation in a Dilute Gas: Measurement of Energy and Ground-State Occupation*, Phys. Rev. Lett. **77** (1996), 4984.

[Est04] J. Esteve, C. Aussibal, T. Schumm, C. Figl, D. Mailly, I. Bouchoule, C. Westbrook, and A. Aspect *The role of wire imperfections in micro magnetic traps for atoms*, J. Phys. A, submitted (preprint: arXiv:physics/0403020) (2004).

[FAS] FAST ComTec GmbH, *MCD-2 Dual Input Multiscaler/Multichannel Analyzer, User Manual*.

[Fig02] C. Figl, A. Grimpe, R. Goldstein, J. Grosser, O. Hoffmann, and F. Rebentrost, *Direct Observation of Atom-Molecule Collisions by Optical Excitation*, Russ. J. Phys. Chem. **76 Suppl.1** (2002), S90.

[Fig03] C. Figl, J. Grosser, O. Hoffmann, and F. Rebentrost, *Differential scattering study of asymptotically forbidden optical transitions in* CaAr *collisions*, Chem. Phys. Lett. **380** (2003), 196.

[Fol00] R. Folman, P. Krüger, D. Casserati, B. Hessmo, T. Maier, and J. Schmiedmayer, *Controlling Cold Atoms using Nanofabricated Surfaces: Atom Chips*, Phys. Rev. Lett. **84** (2000), 4749.

[For98] J. Fortágh, A. Grossmann, and C. Zimmermann, *Miniaturized Wire Trap for Neutral Atoms*, Phys. Rev. Lett. **81** (1998), 5310.

[For02] J. Fortágh, H. Ott, S. Kraft, A. Günther, and C. Zimmermann, *Surface effects in magnetic microtraps*, Phys. Rev. A **66** (2002), 041604.

[Gol01] R. Goldstein, J. Grosser, O. Hoffmann, V. Schumann, and D. Wößner, *Electronic structure of the* NaN_2 *and* NaC_2H_2 *collision complexes: Experiment and theory*, J. Chem. Phys. **114** (2001), 2144.

[Gol04] R. Goldstein, *Untersuchung von Stoßprozessen mittels Laseranregung: Optische Stöße mit molekularen Targets und optische Stöße mit Femtosekundenlaserpulsen*, Ph.D. thesis, Universität Hannover, 2004.

[Gon94] M. A. Gondal, M. A. Khan, and M. H. Rais, *Laser-Enhanced Ionization Studies of the Blue Satellite Band in the* Ca-Ar *System Associated with the Electric-Quadrupole Transition* $4s^2\ ^1S_0 \rightarrow 4s3d^1D_2$ *of Calcium*, Il Nuovo Cimento **17 D** (1994), 9.

[Gro94] J. Grosser, D. Gundelfinger, A. Maetzing, and W. Behmenburg, *Laser-assisted collisions: investigation of the optical collision process* Na(3s)+Kr+$h\nu$ →Na(3p)+Kr *in a crossed beam experiment*, J. Phys. B **27** (1994), L367.

[Gro96] J. Grosser, D. Hohmeier, and S. Klose, *Differential cross sections for radiation assisted collisions between atoms* , J. Phys. B **29** (1996), 299.

[Gro97a] J. Grosser, O. Hoffmann, S. Klose, and F. Rebentrost, *Optical excitation of collision pairs in crossed beams: Determination of the* NaKr $B^2\Sigma$ *potential*, Europhys. Lett. **392** (1997), 147.

[Gro97b] J. Grosser, O. Hoffmann, C. Rakete, and F. Rebentrost, *Direct Observation of the Geometry of Atom-Atom and Atom-Molecule Collisions*, J. Phys. Chem. A **101** (1997), 7627.

[Gro99a] J. Grosser, O. Hoffmann, and F. Rebentrost, *Direct observation of collisions by laser excitation of the collision pair*, Comment. Mod. Phys. **1D** (1999), 117.

[Gro99b] J. Grosser, O. Hoffmann, and F. Schulze-Wischeler, *Direct observation of non-adiabatic transitions in* Na+*rare-gas differential optical collisions*, J. Chem. Phys. **111** (1999), 2853.

[Gro00] J. Grosser, O. Hoffmann, and F. Rebentrost, *Accurate probing of the repulsive* $X^2\Sigma$ *and* $B^2\Sigma$ *potentials of* NaNe *and* NaAr *by differential optical collision experiments*, J. Phys. B **33** (2000), L577.

[Gun93] D. A. Gundelfinger, Diplomarbeit, Universität Hannover, 1993.

[Gus01] T. L. Gustavson, A. P. Chikkatur, A. E. Leanhardt, A. Görlitz, S. Gupta, D. E. Pritchard, and W. Ketterle, *Transport of Bose-Einstein Condensates with Optical Tweezers*, Phys. Rev. Lett. **88** (2001), 020401.

[Hav86] M. D. Havey, F. T. Delahanty, L. L. Vahala, and G. E. Copeland, *Experimental fine-structure branching ratios for Na-rare-gas optical collisions*, Phys. Rev. A **34** (1986), 2758.

[Hän01] W. Hänsel, P. Hommelhoff, T. W. Hänsch, and J. Reichel, *Bose-Einstein condensation on a microelectronic chip*, nature **413** (2001), 498.

[Hed72] R. E. M. Hedges, D. L. Drummond, and A. Gallagher, *Extreme-Wing Line Broadening and* Cs-*Inert-Gas Potentials*, Phys. Rev. A **6** (1972), 1519.

[Hof95] O. Hoffmann, Diplomarbeit, Universität Hannover, 1995.

[Hof99] O. Hoffmann, *Direkte Beobachtung von atomaren und molekularen Stoßpaaren*, Ph.D. thesis, Universität Hannover, dissertation.de, 1999.

[Hoh95] D. Hohmeier, *Untersuchung der photoninduzierten Stoßanregung in gekreuzten Atomstrahlen mit differentiellem Nachweis*, Diplomarbeit, Universität Hannover, 1995.

[Jav86] J. Javanainen, *Oscillatory Exchange of Atoms between Traps Containing Bose Condensates*, Phys. Rev. Lett. **57** (1986), 3164.

[Jon03] M. P. A. Jones, C. J. Vale, D. Sahagun, B. V. Hall, C. C. Eberlein, B. E. Sauer, K. Furusawa, D. Richardson, and E. A. Hinds, *Cold atoms probe the magnetic field near a wire*, cond-mat / 0308434, 2003.

[Jos62] B. D. Josephson, *Possible new effects in superconductive tunneling*, Phys. Lett. **1** (1962), 251.

[Jun02] M. Jungen, private communication, 2002.

[Kau97a] J. G. Kaup and W. H. Breckenridge, *Spectroscopic characterization of the metastable* $(4p\pi^2\Pi_{0^-})$ *valence states and the* $5s^3\Sigma^+$ *Rydberg states of the* CaAr, CaKr *and* CaXe *van der Waals molecules*, J. Chem. Phys. **107** (1997), 5283.

[Kau97b] J. G. Kaup and W. H. Breckenridge, *Spectroscopic characterization of the singly excited* $CaAr(4d\pi^3\Pi_0)$, $CaAr(4d\delta^3\Delta_1)$ *states and the doubly excited* CaAr $(4p\pi 4p\pi^3\Sigma^-)$ *state*, J. Chem. Phys. **107** (1997), 5676.

[Ket92] W. Ketterle and D. E. Pritchard, *Trapping and Focusing Ground State Atoms with Static Fields*, Appl. Phys. B **54** (1992), 403.

[Ket96] W. Ketterle and N. J. van Druten, *Evaporative cooling of trapped atoms*, Adv. At. Mol. Opt. Phys. **37** (1996), 181.

[Ket99] W. Ketterle, S. S. Durfee, and D. M. Stamper-Kurn, *Making, probing and understanding Bose-Einstein condensates*, Proceedings of the International School of Physics "Enrico Fermi", Course CXL, Bose-Einstein Condensation in Atomic Gases (M. Inguscio, S. Stringari, and C. E. Wieman, eds.), Societa Italiana di Fisica, 1999.

[Key00] M. Key, I. G. Hughes, W. Rooijakkers, B. E. Sauer, E. A. Hinds, D. J. Richardson, and P. G. Kazansky, *Propagation of Cold Atoms along a Miniature Magnetic Guide*, Phys. Rev. Lett. **84** (2000), 1371.

[Kha96] M. A. Khan, R. A. Qureshi, and M. A. Gondal, **Ar**-*supported atomic population transfer from the* $3d4p\,^1D_2$ *to nearby states of* Ca, Chem. Phys. Lett. **264** (1996), 273.

[Kir00] K. N. Kirschner, *Theoretical Investigation of* Ca· RG, Ca^+· RG, *and* Ca^{2+}· RG *(*RG = Ar *and* Ne*) complexes*, J. Chem. Phys. **112** (2000), 10228.

[Kle86] P. Kleiber and K. Sando, *Laser-absorption profiles of the calcium – rare-gas* $(4s\,^1\Sigma^+ - 5s\,^1\Sigma^+)$ *molecular bands*, Phys. Rev. A **35** (1986), 3715.

[Kle88] P. Kleiber, A. Fletscher, and K. Sando, *Laser-absorption profiles of the magnesium-rare-gas (3s-4s) molecular bands*, Phys. Rev. A **37** (1988), 3584.

[Klo96] S. Klose, *Messung differentieller Wirkungsquerschnitte laserunterstützter Stoßprozesse*, Ph.D. thesis, Universität Hannover, 1996.

[Kra02] S. Kraft, A. Günther, H. Ott, D. Wharam, C. Zimmermann, and J. Fortágh, *Anomalous longitudinal magnetic field near the surface of copper conductors*, J. Phys. B **35** (2002), L469.

[Lam85] Lambda Physik, Göttingen, Germany, *Excimer laser emg 201 msc, instruction manual*, 1985.

[Lam87] Lambda Physik, Göttingen, Germany, *Dye Laser FL 3001/2, instruction manual*, 1987.

[Lea02] A. E. Leanhardt, A. P. Chikkatur, D. Kielpinski, Y. Shin, T. L. Gustavson, W. Ketterle, and D. E. Pritchard, *Propagation of Bose-Einstein Condensates in a Magnetic Waveguide*, Phys. Rev. Lett. **89** (2002), 040401.

[Lea03] A. E. Leanhardt, Y. Shin, A. P. Chikkatur, D. Kielpinski, W. Ketterle, and D. E. Pritchard, *Bose-Einstein Condensates near a Microfabricated Surface*, Phys. Rev. Lett. **90** (2003), 100404.

[Lee91] C. J. Lee, M. D. Havey, and R. P. Meyer, *Laser spectroscopy of molecular LiHe: The* $3d^2\Delta \leftarrow 2p^2\Pi$ *transition*, Phys. Rev. A **43** (1991), 77.

[Let88] P. D. Lett, R. N. Watts, C. I. Westbrook, and W. D. Phillips, *Observation of Atoms Laser Cooled below the Doppler Limit*, Phys. Rev. Lett. **61** (1988), 169.

[Leu97] A. W. K. Leung, J. G. Kaup, D. Bellert, J. G. McCaffrey, and W. H. Breckenridge, *Spectroscopic characterization of the weakly bound* $Ca(4s4d\sigma^3D_3)\cdot Ar[^3\Sigma^+]$ *state: Evidence for a substantial maximum in the potential curve at long range*, J. Chem. Phys. **111** (1999), 2484.

[Leu99] A. W. K. Leung, J. G. Kaup, D. Bellert, and J. G. McCaffrey, *Spectroscopic characterization of excited* $Ca(4s4d\delta^3D_J)$ RG $(^3\Delta_{1,2})$ *states (*RG = Ar, Kr, Xe*): No "heavy -atom" mixing of* $RG(nd\delta)$ *character into the wave functions*, J. Chem. Phys. **111** (1999), 981.

[Lin01] G. Lindenblatt, H. Wenz, and W. Behmenburg, *Study of excitation transfer* Li(3D → 3P) *occuring in optical collisions with rare gas atoms experimentally*, Euro. Phys. J. D **13** (2001), 329.

[LIN03] LINOS, Göttingen, Germany, *Catalog*, 2003.

[Lye02] J. E. Lye, C. S. Fletcher, U. Kallmann, H.-A. Bachor, and J. D. Close, *Images of evaporative cooling to Bose-Einstein condensation*, J. Opt. B **4** (2002), 57.

[Mae94] A. Maetzing, *Eine neue Methode zur Untersuchung von Stoßprozessen: Optische Stöße in gekreuzten Atomstrahlen*, Ph.D. thesis, Universität Hannover, 1994.

[Mas90] T. B. Massalski and H. Okamoto (eds.), *Binary Alloy Phase Diagrams*, 2nd ed., ASM International, 1990.

[Mat95] M. Mattiesen, *Entwicklung eines Detektors für Natrium-Atome in Rydbergzuständen*, Examensarbeit, Universität Hannover, 1995.

[Mei02] F. Meier and W. Zwerger, *Josephson tunneling between weakly interacting Bose-Einstein condensates*, Phys. Rev. A **64** (2002), 033610.

[Mes82] J. M. Mestdagh, J. Berlande, J. Cuvellier, P. de Pujo, and A. Binet, *Fine-structure transitions in* K(4P) *induced by rare gases and diatomic molecules*, J. Phys. B **15** (1982), 439.

[Mil88] D. R. Miller, Atomic and Molecular Beam Methods (G. Scoles, ed.), Oxford University Press, 1988.

[Nes63] A. N. Nesmeyanov, *Vapor pressure of the chemical elements*, Elsevier, 1963.

[Nik84] E. E. Nikitin and S. Ya. Umanskii, *Theory of Slow Atomic Collisions*, Springer, Berlin, 1984.

[Ott01] H. Ott, J. Fortágh, G. Schlotterbeck, A. Grossmann, and C. Zimmermann, *Bose-Einstein Condensation in a Surface Microtrap*, Phys. Rev. Lett. **87** (2001), 230401.

[Pas74] J. Pascale and J. Vandeplanque, *Excited molecular terms of the alkali-rare gas atom pairs*, J. Chem. Phys. **60** (1974), 2278.

[Pas84] J. Pascale, J.-M. Mestdagh, J. Cuvellier, and P. de Pujo, *Test of interatomic potentials and study of coupling mechanisms involved in fine-structure transitions for* K(4^2P)+Ar *collisions*, J. Phys. B **17** (1984), 2627.

[Pre86] W. H. Press, B. P. Flannery, S. A. Teukosky, and W. T. Vetterling, *Numerical recipes. The Art of Scientific Computing*, Cambridge University Press, 1986.

[Raa87] E. L. Raab, M. Prentiss, A. Cable, S. Chu, and D. E. Pritchard, *Trapping of Neutral Sodium Atoms with Radiation Pressure*, Phys. Rev. Lett. **59** (1987), 2631.

[Rad85] A. A. Radzig and B. M. Smirnov, *Reference Data on Atoms, Molecules, and Ions*, Springer-Verlag, Berlin, 1985.

[Reb98] F. Rebentrost, S. Klose, and J. Grosser, *Quantum and semiclassical dynamics of differential optical collisions*, Euro. Phys. J. D **1** (1998), 277.

[Reb03] F. Rebentrost, *private communication*, 2003.

[Rei99] J. Reichel, W. Hänsel, and T. W. Hänsch, *Atomic Micromanipulation with Magnetic Surface Traps*, Phys. Rev. Lett. **83** (1999), 3398.

[Rei01] J. Reichel, W. Hänsel, P. Hommelhoff, and T. W. Hänsch, *Applications of integrated magnetic microtraps*, Appl. Phys. B **72** (2001), 81.

[Sac97] C. A. Sackett, C. C. Bradley, and R. G. Hulet, *Optimization of evaporative cooling*, Phys. Rev. A **55** (1997), 3797.

[Sat95] Y. Sato, *Photoabsorption studies of Quasimolecules of alkaline-earth and related metal atoms*, AIP Conf. Proc. **328** (1995), 316.

[Say80] B. Sayer, M. Ferray, J. P. Visticot, and J. Lozingot *Experimental investigation of the* Cs($5D_{5/2,m=1/2}$ *)– rare-gas interaction: potential curves and oscillator strength of the dipole-induced transitions*, J. Phys. B **13** (1980), 177.

[Sch03] S. Schneider, A. Kasper, Ch. vom Hagen, M. Bartenstein, B. Engeser, T. Schumm, I. Bar-Joseph, R. Folman, L. Feenstra, and J. Schmiedmayer, *Bose-Einstein condensation in a simple microtrap*, Phys. Rev. A **67** (2003), 023612.

[Sch04] T. Schmidt, C. Figl, A. Grimpe, J. Grosser, O. Hoffmann, and F. Rebentrost, *Coherent control of atomic collisions using elliptic polarization*, Phys. Rev. Lett., 2004, accepted.

[Shi03] Y. Shin, M. Saba, A. Schirotzek, T. A. Pasquini, A. E. Leanhardt, D. E. Pritchard, and W. Ketterle, *Distillation of Bose-Einstein condensates in a double-well potential*, cond-mat / 0311514, 2003.

[Spi02] F. Spiegelman and L. Maron, *Two-electron pseudopotential investigation of the electronic structure of the* CaAr *molecule*, J. Chem. Phys. **117** (2002), 7534.

[Ued89] K. Ueda, T. Komatsu, and Y. Sato, *Observation of collision-induced-diploe absorption bands in strontium-rare-gas mixtures. 5s-4d bands*, J. Chem. Phys. **91** (1989), 4495.

[Vad01] C. Vadla, V. Horvatic, and K. Niemax, *Oscillator strength of the strongly "forbidden" Pb($6p^2\,{}^3P_0 \rightarrow 6p^2{}_j\,{}^3P_1$ transition at 1278.9nm* , Eur. Phys. D **14** (2001), 23.

[Var87] N. B. Vargaftik, *Handbook of physical properties of liquids and gases: pure substances and mixtures*, 2nd ed., Hemisphere, 1987.

[Vol96] U. Volz and H. Schmoranzer, *Precision Lifetime Measurements on Alkali Atoms and on Helium by Beam-Gas-Laser Spectroscopy*, Physica Scripta **T65** (1996), 48–56.

[Wan03] D.-W. Wang, M. D. Lukin, and E. Demler, *Disordered Bose-Einstein Condensates in Quasi One-Dimensional Magnetic Microtraps*, cond-mat / 0307402, 2003.

[Weh95] O. Wehrhahn, *Untersuchung optischer Stöße in gekreuzten Atomstrahlen*, Diplomarbeit, Universität Hannover, 1995.

[Zim99] D. Zimmermann, M. Braune, and D. Schwarzhans, *Recent Progress in the Determination of Interatomic Potentials of Alkali-Argon Systems*, AIP Conf. Proc. **10** (1999), 395.

Danke, thanks, merci

Thanks to Achim Grosser, who gave me the opportunity of working on the interesting subject of opticall collisions. He was always open for my questions, even finding time on Christmas day to discuss the latest result of the always-almost-at-end fitting procedure, and he was always in the mood to take us for a sailing trip. I also thank the other members of the Hannover group that were really great colleagues to work with: Ralf Goldstein, Olaf Hoffmann, and André Grimpe. I thank Elke Möbius and Hannes Goldstein, adopted members of the group, for being around. Peter Wilhelms always had a suitable motto to share with us. Thanks to Sabine Ruhmkorff for the administrative work. In the workshop, I would like to thank Manfred Marquard who spent endless time on making and repairing the calcium beam source, Helmut Glanz for help with electronics, Hartmut Lehmann, Philipp Schauzu, Stefan Bertram, Jochen Claus, and Jochen Paul for help with the computers. Thanks to Frank Rebentrost for a great collaboration and important help in various programming tasks. Thanks to Martin Jungen as well as Dieter Zimmermann for making their data available prior to publication.

From the Paris side, the first person to thank is Alain Aspect for giving me the opportunity to work in his group on BEC. I also thank Chris Westbrook who agreed to be my co-supervisor and supported me. Thanks to Denis Boiron for working on the cotutelle agreement. I am indebted to the members of my working group for many fruitful discussions and more: Jérôme Esteve, also of much help in translating the abstract to French, Christine Aussibal, Isabelle Bouchoule, and Thorsten Schumm. Thanks to all the other members-too many to name everyone. Thanks to José Carlos Gomez and Inês Vinga for a great time in Paris.

Thanks to Eberhardt Tiemann for organizing the Graduate College. Thanks to Olivier for the calcium data. Thanks to all the other members of the Graduate College for many interesting talks and great Celidh. Special thanks to Uta Weiland and Michaela Malec for the work and fun we shared. Thanks to Katrin Pfennig, Ute Reuter and Jocelyne Armand for great support with the burocratic stuff.

Melanie von Görtz and Fiona Meißner were the best flatmates. Thanks. Thanks to both my parents and my step parents, as well as my beloved grandmother who gave me every support they could. Thanks to my little brother and Anna for making me smile, although it will be some years still before they will be able to read these lines, and the crazy lovely people in Minden.

Thanks to Stefan for keeping up with me during the time of hard work. Thank you for unforgettable visits in Paris and your support.

Curriculum Vitae

University education:

Oct. 2000–May 2004	Ph.D. student at the University of Hannover and Université de Paris-Sud XI
Oct. 1994–Aug. 2000	Diploma studies in physics at the University of Hannover; degree: Physik Diplom

School education:

Aug. 1987–July 1994	Goetheschule Hannover; final examination: Abitur
Aug. 1991–Jan.1992	Brighton High School, Rochester, N.Y., USA

Research positions and scholarships:

Feb. 2002–May 2004	Scholarship from the European Graduate College *Interference and Quantum Applications*
Jan. 2001–Jan. 2002	Scientific assistant at the University of Hannover
Oct. 2000–Dec. 2000	Scholarship “GradFög” from the state of Lower Saxony

List of Publications

1. T. Schmidt, C. Figl, A. Grimpe, J. Grosser, O. Hoffmann, and F. Rebentrost, *Coherent control of atomic collisions using elliptic polarization*, Phys. Rev. Lett., **92** (2004), 033201.
2. C. Figl, J. Grosser, O. Hoffmann, F. Rebentrost, *Differential Optical Collisions in the KAr(4s-4p) system*, Khimizheskaya Fizika **23** (2004), 20-23.
3. C. Figl, R. Goldstein, J. Grosser, O. Hoffmann, F. Rebentrost, *Observation of elementary nonadiabatic processes in atom - atom and atom - molecule collisions*, Khimizheskaya Fizika **23** (2004), 24-28.
4. C. Figl, J. Grosser, O. Hoffmann, and F. Rebentrost, *Differential scattering study of asymptotically forbidden optical transitions in* CaAr *collisions*, Chem. Phys. Lett. **380** (2003), 196.
5. C. Figl, A. Grimpe, R. Goldstein, J. Grosser, O. Hoffmann, and F. Rebentrost, *Direct Observation of Atom-Molecule Collisions by Optical Excitation*, Russ. J. Phys. Chem. **76 Suppl.1** (2002), S90.
6. C. Figl, J. Grosser, O. Hoffmann, and F. Rebentrost, *Repulsive* KAr *potentials from differential optical collisions* J. Phys. B, accepted (2004).
7. J. Esteve, C. Aussibal, T. Schumm, C. Figl, D. Mailly, I. Bouchoule, C. Westbrook, and A. Aspect *The role of wire imperfections in micro magnetic traps for atoms*, J. Phys. A, submitted (preprint: arXiv:physics / 0403020) (2004).